KAUNAS UNIVERSITY OF TECHNOLOGY

DARIUS ŽIŽYS

INVESTIGATION AND OPTIMIZATION OF AUTONOMOUS ENERGY SOURCES OPERATING IN HIGHER TRANSVERSE VIBRATION MODES

Doctoral Thesis
Engineering Sciences, Mechanical Engineering (09T)

2018, Kaunas

This dissertation was prepared at Kaunas University of Technology, Faculty of Design and Mechanical Engineering, Department of Mechanical Engineering, during the period of 2013 – 2017.

Scientific Supervisor:

Prof. Dr. Rimvydas GAIDYS (Kaunas University of Technology, Technological Sciences, Mechanical Engineering, 09T).

Doctoral dissertation has been published in:
http://ktu.edu

Editor:

Jurgita Motiejūnienė

ISBN 978-609-02-1449-7

The bibliographic information about the publication is available in the National Bibliographic Data Bank (NBDB) of the Martynas Mažvydas National Library of Lithuania.

KAUNO TECHNOLOGIJOS UNIVERSITETAS

DARIUS ŽIŽYS

AUTONOMINIŲ ENERGIJOS ŠALTINIŲ, VEIKIANČIŲ AUKŠTESNIŲJŲ SKERSINIŲ VIRPESIŲ MODŲ REŽIMU, TYRIMAS IR OPTIMIZAVIMAS

Daktaro disertacija
Technologijos mokslai, mechanikos inžinerija (09T)

2018, Kaunas

Disertacija rengta 2013–2017 metais Kauno technologijos universiteto Mechanikos inžinerijos ir dizaino fakulteto Mechanikos inžinerijos katedroje.

Mokslinis vadovas:

Prof. Dr. Rimvydas GAIDYS (Kauno technologijos universitetas, technologijos mokslai, mechanikos inžinerija, 09T).

Interneto svetainės, kurioje skelbiama disertacija, adresas:
http://ktu.edu

Redagavo:

Jurgita Motiejūnienė

ISBN 978-609-02-1449-7

Leidinio bibliografinė informacija pateikiama Lietuvos nacionalinės Martyno Mažvydo bibliotekos Nacionalinės bibliografijos duomenų banke (NBDB)

SYMBOLS AND ABBREVIATIONS

AC – Alternating Current
AWCS – Autonomous Wireless Condition Sensor
COPS – Compliant Orthoplanar Springs
CPC – Coupled Piezoelectric Circuit
CNT-PDMS – Carbon Nano Tube Polydimethylsiloxane
DC – Direct Current
DFT – Discrete Fourier Transform
DOF – Degree of Freedom
EMF – Electromotive Force
FDM – Feasible Direction Method
FEA – Finite Element Analysis
FEM – Finite Element Model
FRF – Frequency Response Function
FPCB – Flexible Printed Circuit Board
GA – Genetic Algorithm
GRP – Gradient Projection Method
LFR – Low Frequency Resonator
MEMS – Microelectromechanical systems
MPG – Micro Power Generator
PET – Polyethylene Terephthalate
PVEH – Piezoelectric Vibration Energy Harvester
PVDF – Polyvinylidene Fluoride
PZT – Lead Zirconate Titanate
RMS – Root Mean Square
RF – Radio Frequency
SLP – Sequential Linear Programming
SUMT – Sequential Unconstrained Minimization Technique
WSN – Wireless Sensor Nodes

INTRODUCTION

Research Relevance, Aim and objectives

In recent decades' smart gadgets, various micro electro-mechanic devices and other MEMs have become popular. In everyday human life, this can be considered because of increasing need to miniaturize previously bulky systems such as sensor nodes, structure health, body health monitoring, microcontrollers, etc. The main drawback and limitation of such devices are reliable power supply, since, as the purpose of wireless sensor node dictates, it is often not possible or too expensive to use batteries as the man power source and the external power supply is not implementable due to the location of the sensor node. This engineering challenge can be tackled utilizing renewable energy sources such as mechanical energy, thermal gradients, solar or wind energy, radiation, etc. It was recognized by [117] that the power consumption goal for devices of size <1 cm3 is 100 μW, MEMS, wireless sensor nodes, micro-RF receivers and other similar devices all use power ranging from 10 nW to 1 mW, which is acknowledged as a realistic goal for modern energy harvesters. With advancing material science, we are now enabled to take advantage of energy conversion mechanisms that in the past was deemed as inefficient and not paying off, like photovoltaic, triboelectric, thermoelectric, piezoelectric etc. transducers. As some of these conversion mechanisms and devices using these mechanisms are efficient but need certain conditions like thermal gradients, direct sunlight or require substantial amount of volume like solar panels, water turbines, etc. Mechanical energy and vibrations are the most viable energy source for MEMS devices in terms of availability and ease of harvesting.

To harness useful mechanical energy from ambient vibrations, various transduction mechanisms are used: electrostatic, electromagnetic and piezoelectric, but each of these has its pros and cons, such as the size, efficiency dependency on ambient vibration frequencies, sophisticated devices. From the latter, the piezoelectric transducer is recognized as the most promising due to its simplicity and efficiency, but it requires the transducer to be working on frequencies matching its natural frequency, thus significantly limiting its applications. Piezoelectric transducers are also difficult to use for low frequency vibration energy harvesting since the size of the device is increased significantly to lower its natural frequency. To counter these issues and to increase the efficiency of these harvesters, a number of strategies have been developed.

In the literature review section of the thesis, the problematics and challenges of energy harvesting are analysed. Macro energy harvesting mechanisms such as solar or wind energy are only reviewed briefly to get a better overview of the situation in the market and to identify where the vibration energy harvesting stands. In the thesis, not only the possible applications, configurations and modelling were reviewed but also a great interest was shown for numerical investigation and experimental verification techniques of such devices. Different optimization techniques and possibilities of their use were also investigated. The main vibration energy to electricity conversion methods are covered shortly, summarizing their basic operation principles as well as advantages and disadvantages. Since piezoelectric energy

harvester relies solely on piezoelectric effect, this transduction mechanism was investigated in more detail as well as materials used and their characteristics. This work also involves frequency-up converting tandem where a low frequency resonator and a high frequency energy harvester are operating in tandem inducing high frequency vibrations in the energy harvester from the low frequency ambient vibration via impact coupling to produce high frequency power output at low frequency ambient vibrations. This work required substantial investigation of impact coupling modelling.

In the first section the literature review, different types of transduction mechanisms for ambient energy, such as solar, wind, thermal and other types are presented focusing on mechanical energy harvesting and piezoelectric transducers. Novelty and fields of applications of such devices are reviewed. It is recognized that wireless sensor nodes (WSN) might be the best application for such energy harvesters due to their small scale and comparatively small power output.

Aim of the work:

The aim of this research is to analyse and develop different piezoelectric vibration energy harvester power output maximization techniques taking advantage of higher vibration modes and ensuring it's operation at varying mechanical excitation conditions.

To achieve the aim of the work, several **objectives** have been formulated.

1. Develop a methodology for calculation of segmentation location of piezoelectric material layers to maximize the energy output from energy harvesters operating at higher transverse vibration modes and investigate distribution of energy in the active element.
2. Develop mathematical and numerical models for nonlinear dynamic contact of vibration energy harvester's piezoelectric elements and investigate the behaviour of developed models under vibro-impact conditions.
3. Create a coupled piezoelectric-circuit finite element model (CPC-FEM) for piezoelectric energy harvester enabling prediction of its power output at different dynamic conditions while operating at harmonic excitation conditions at non-impacting and vibro-impacting modes.
4. Determine mechanical and electrical parameters of the piezoelectric elements' nonlinear dynamic contact interaction applying investigated methods and analyse their impact on effectiveness of the harvester.
5. Develop mathematical and numerical models for optimization of the problem of piezoelectric vibration energy harvester maximizing harvested energy, perform the analysis of obtained results and experimentally verify results obtained from the created models.

Object of investigation

Nonlinear piezoelectric vibration energy harvester operating in dynamic/vibro-impact contact conditions at higher vibration modes. The problem of increasing efficiency of such a harvester is addressed.

Investigation methods

Investigation is preformed using advanced numerical and experimental methods and equipment which is also presented in the literature review. The models of piezoelectric vibration energy harvesters are created using FE method. The models were used for the development of methodology necessary for determining the best segmentation point of piezoelectric elements on piezoelectric vibration energy harvester operating in higher transverse vibration modes, investigation of nonlinear dynamic contact interaction of piezoelectric elements, and shape optimization of the piezoelectric energy harvester. In order to process the numerical and experimental results, the methods of numerical differentiation, integration and Discrete Fourier Analysis were used. The COMSOL Multiphysics software was used to perform the calculations of the FE models, and the MATLAB software was adopted for mathematical calculations.

Several experiments were performed to verify the modelling results.

- The results obtained from theoretical investigation and FE modelling of the methodology developed for determining the best segmentation point of piezoelectric elements on the piezoelectric vibration energy harvester operating in higher transverse vibration modes were performed. The results of modal analysis were verified using the PRISM holography system measuring the vibration amplitudes in y direction and verifying natural frequencies. Experiments were performed to verify the open-circuit voltage output of the active element of a constant cross-section and the optimally-shaped active element obtained from FE model transient analysis. The experimental setup consists of a piezoelectric vibration energy harvester and two systems connected to it, the excitation system and the data acquisition system. The function generator AGILENT 33220A is used to control the harmonic excitation signal transmitted to the electromagnetic shaker. The single-axis miniature piezoelectric charge-mode accelerometer METRA KS-93 was attached at the bottom of the electromagnetic shaker for acceleration measurements. The experiments were performed in the Institute of Mechatronics, KTU (Kaunas). The substrate layer was fabricated from structural steel by using water jet cutting. The piezoelectric material specimens were manufactured using a picosecond laser PL10100 (Ekspla). The laser plates were guided using galvanometric scanners (ScanLab). The piezoelectric material used was PVDF, namely DT1-028K by Measurement Specialties Inc., Hampton. The laser cutting experiments were done in the Centre of Physical Science and Technology (Vilnius).
- The results obtained from model investigation of nonlinear dynamic contact of vibration energy harvester's piezoelectric elements under vibro-impact conditions were verified experimentally in the Institute of Mechatronics, KTU (Kaunas). The first experiment was done wit hthe aim to compare the dynamic response of PVEH under contact excitation under open circuit conditions. Voltage-time dependence was obtained experimentally, and despite the transient process, its duration between impacts and overall

behaviour shows good agreement with the theoretical model. The second experiment was performed in order to compare modelling and experimentally obtained peaks of harvested power as a function of load resistance under highly nonlinear vibro-shock inputs to the transducer. The modelling results show good agreement with experimental the results. The displacements were measured using a Doppler Vibrometer (OFV-512 differential laser interferometer, Polytec, Waldbronn, Germany) with a Polytec OFV-5000 controller (Polytec, Waldbronn, Germany) connected to it. The electromagnetic shaker signal was controlled by a 33220A function generator (Keysight, Santa Clara, USA), and the VPA2100MN voltage amplifier (HQ Power, Gavere, Belgium) was used to amplify the signal. A single axis accelerometer was attached to the acrylic glass support mounted on top of the shaker to measure the excitation amplitude (single axis accelerometer KS-93). The readings were taken by a 3425 USB oscilloscope.

Defended statements

The following scientific novelties are presented in the thesis:

1. Developed and realized methodology to calculate the most effective segmentation line of piezoelectric material layers for piezoelectric vibration energy harvesters operating in higher transverse vibration modes.
2. Developed mathematical and numerical model of vibration energy harvester element nonlinear vibro-impacting contact. Harvesters, consisting of Low Frequency Resonator (LFR) and Piezoelectric Vibration Energy Harvester (PVEH) tandem dynamic characteristics have been investigated.

Statement of novelty

1. A novel calculation methodology was proposed and implemented for the identification of optimal segmentation location (coincides with normal strain node) of piezoelectric elements for devices operating in the second or higher transverse vibration modes. Up to 7% increase in generated open circuit voltage was achieved.
2. Optimal geometric and electrical parameters of frequency-up converting piezoelectric vibration energy harvester operating under highly nonlinear dynamic contact vibro-impact excitation were identified, increasing harvesters generated power output up to 150%. It was found that the highest power output is achieved if the dynamic contact location coincides with the transverse displacement nodal point of harvester operating in the second transverse vibration mode shape.
3. Applying mathematical optimization method, the implemented methodology of piezoelectric vibration energy harvester geometrical shape optimization, which enabled an increase of its efficiency by 16%.

Practical use

During the work, specific finite element models and calculation methodologies were created that can be used for very relevant and advanced investigation of vibro-impact contact process dynamic in piezoelectric vibration energy harvesters and determining harvester's optimal parameters, which enables cost reduction of experimental and theoretical investigations. These models can also be applied for mechanical interaction synthesis of energy harvesters utilizing different transduction mechanisms.

List of Publications

"ISIS Web of Science" publication with citation index

1. D. Žižys, R. Gaidys, V. Ostaševičius, R. Daukševičius, V. Daniulaitis. Segmentation of Vibro-Shock Cantilever-Type Pjezoelectric Energy Harvester Operating in Higher Transverse Vibration Modes // Sensors 2016, 16 (1), 11; doi:10.3390/s16010011
2. D. Žižys, R. Gaidys, V. Ostaševičius, B. Narijauskaitė. Vibro-Shock Dynamics Analysis of a Tandem Low Frequency Resonator-High Frequency Piezoelectric Energy Harvester // Sensors 2017, 17 (5), 970; doi:10.3390/s17050970

International conferences

1. D. Žižys, R. Gaidys, V. Ostaševičius. *International conference "Mechanika 2014"*. Optimal Shape Piezoelectric Energy Harvester Design.
2. D. Žižys, R. Gaidys, V. Ostaševičius. *International conference "Mechanika 2016"*. Electric Power Output Maximization for Piezoelectric Energy Harvester by Optimizing Resistive Load.
3. D. Žižys, R. Gaidys, V. Ostaševičius. *Respublikinis XXIV Lietuvos skaičiuojamosios mechanikos asociacijos seminaras*. Gembinio energijos generatoriaus formos optimizavimo uždavinio matematinis modelis.
4. D. Žižys, R. Gaidys, V. Ostaševičius, B. Narijauskaitė. *International conference "Mechanika 2017"*. Maximization of energy harvesting from vibrations.
5. D. Žižys, R. Gaidys, V. Ostaševičius. *"Mechanika 2016": Proceedings of the 21st international scientific conference*. Effect of piezoelectric layer segmentation methods on bimorph cantilever energy output, 2016. p. 314–316.

1. LITERATURE REVIEW.

In the literature review section, the literature used for the thesis is reviewed starting from different sources of renewable energy and their applicability for MEMS devices. Mechanical and especially vibration energy was recognized as the most promising source for powering up such devices, thus in the next section different transduction mechanisms of vibration energy harvesting were investigated, including electromagnetic, electrostatic and piezoelectric ones.

Among them, piezoelectric energy harvesting devices have received more attention due to their self-contained power without requiring external voltage source, highest energy density and good dynamic responses. The research also emphasized nonlinear energy harvesters and their figures of merit. Frequency up conversion and impact induced vibrations were of most interest since those were recognized as some of the most promising techniques to increase energy output for piezoelectric vibration energy harvesters.

In general, the aim of this section is to briefly introduce the reader to the history of energy harvesting and present benefits and limitations of the piezoelectric transduction mechanism.

1.1. Types of energy sources and their implementation for mechanical energy harvesting.

In the past century, most of energy produced in the world was supplied by wood. Later, wood was replaced by coal, natural gas and petroleum. Now, the largest share of U.S. primary energy production is taken by petroleum which accounts for 36%, while renewable energy accounts only for 13% of total primary energy production [1]. Currently, the use of renewable energy both electricity generation and heat production have sky rocketed. In the EU, it is 16% with the goal for 2020 as high as 20% as identified by Zadeh (2011) [2]. If do not we consider the total energy generated but only electricity generated from renewable sources, the figures are different. In 2016 in the EU, 28% of electricity was generated from renewable energy sources where in 2004 this number was 14%, thus in just 10 years the renewable energy production has doubled. The growth achieved almost solely by the expanse of thee solar and wind energy sector.

Solar power is probably the most abundant macro energy source. It is widely used for heating the water and houses and for the generation of electricity. Where the use of sun energy is limited or inaccessible (e.g., polar regions during winter seasons, cloudy days or nights, etc.), different energy sources are used geothermal energy being one of them. Iceland country report (2017) [3] states that Iceland will increase its electricity generation from geothermal energy by 12% from 2016 to 2020, and geothermal utilization is expected to rise by 70% from 2016 to 2050. Already in 2016, most of Iceland’s energy was carbon free and generated from local renewable energy sources. It needs to be emphasized that the renewable energy sources available for energy generation are usually very much dependent on geographical location, for example the energy of the ocean's tides is only feasible where the tides are strong and high, and the wind energy can only be used in locations with high average winds and

so on. These and many more limitations of renewable and green energy sources have been their biggest disadvantage for a long time. There is also a lack of technologies in order to store the energy generated by renewable energy sources while the fossil fuel can be easily transported and used where it is needed.

The logic changes when downgrading from macro to micro energy sources to use with portable electronics or stationary micro devices like wireless sensor nodes. With consumer electronic devices like mobile phones getting ever hungrier for power the energy, certain saving techniques must be developed. It is stated by Donovan (2016) [4] that low power has been the most important electronic design criterion for at least the last twenty years, and thanks to Moore's Law and a lot of smart engineers, semiconductor power levels have dropped dramatically, often consuming milliwatts in run mode and nanowatts in standby mode.

As a result of dramatic decrease in consumption of power and development of ultra-low power devices like antennas, sensors and controllers, wireless sensor networks became feasible in reality with most of previous drawbacks eliminated. One of the most important drawbacks remaining is power supply. With decreased power consumption, the batteries now need replacements much more rarely, but they still do. This is undesired for devices which are used in difficult to access or inaccessible areas. As a remedy for this problem, a tandem of a battery and an energy harvester can be used significantly increasing the duration between battery replacements, or in the perfect case eliminating the need to replace the battery at all. The renewable energy sources to be used with such devices may be thermal energy, solar energy, radiation and mechanical energy. It is stated by Donovan (2016) [4] that there are several energy harvesting technologies in common use with some innovative techniques just over the horizon. The most common energy sources are light, heat, vibration and RF (see Table 1.1 from [4]), but one or more of them may be more than adequate to power low-power devices in an environment.

Table 1.1 Power available from energy harvesting sources by Donovan (2016) [4]

Source	Source power	Harvested power
	Light	
Indoor	0,1 mW/cm^2	10 μW/cm^2
Outdoor	100 mW/cm^2	10 mW/ cm^2
	Vibration/motion	
Human	0,5m at 1 Hz 1 m/s^2 at 50 Hz	4 μW/cm^2
Machine	1m at 5 Hz 10 m/s^2 at 1 kHz	100 μW/cm^2
	Thermal	
Human	20 mW/cm^2	30 μW/cm^2
Machine	100 mW/cm^2	1-10 mW/cm^2
	RF	
GSM BSS	0.3 μW/cm^2	0.1 μW/cm^2

Table 1.1 indicated that vibration and motion energy might not be the most promising energy source in terms of the amount of energy density, but it is the simplest to implement. Vibration energy harvesting can be implemented in different ways, but

overall, they are usually spring-mass systems exploiting resonance phenomena. The three main transduction mechanisms used for vibration energy harvesting are:

- piezoelectric
- electromagnetic
- electrostatic

All the devices presented in the literature review are summarized in tables classified by transduction type, and conclusions are drawn for suitability of the various techniques. Figure 1.1 by Beepy (2012) [5] illustrates the distribution of utilization of different vibration frequencies and accelerations by different kinds of vibrational energy harvesters. Ostasevicius (2017) [6] have outlined numerous applications for micro energy harvesters for vibration energy harvesting in biomechanical microsystems. Some form of transduction mechanism is obviously required to convert the kinetic energy into electrical energy. This mechanism has to be incorporated into the mechanical system that has been designed to maximize the energy coupled from the application environmental to the transducer.

The transducer can generate electricity from the mechanical strain or the relative displacement present within the system, depending upon the type of the transducer. The use of active materials such as piezoelectrics is an obvious example that enables the strain to be directly converted into electrical energy. Electromagnetic and electrostatic transduction exploits the relative velocity or displacement that occurs within a generator. Each transduction mechanism has different characteristics such as damping effects, ease of use, scalability and effectiveness.

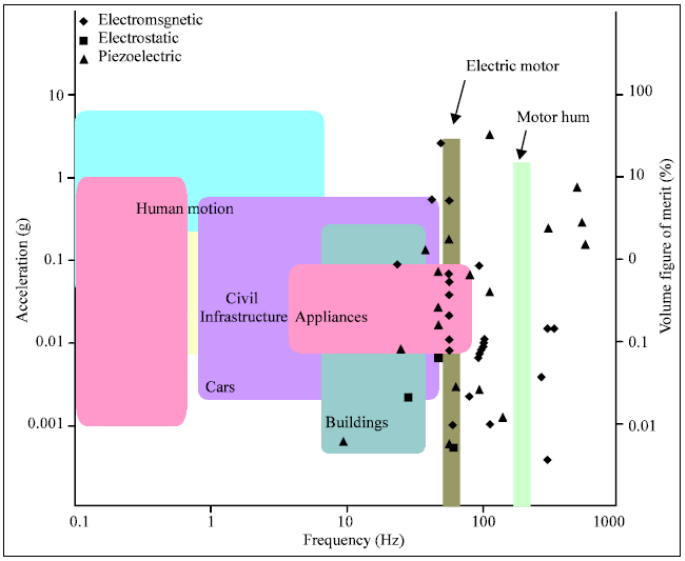

Figure 1.1. Distribution of utilization of different vibration frequencies and accelerations by different kinds of vibrational energy harvesters [5]

The suitability of each mechanism for any application depends largely on the practical constraints applied. Assuming no size constraints, electromagnetic harvesting will be most efficient because the coil can be large, with a high number of

turns and low coil resistance (larger diameter wire) providing very high potential coupling factors. The efficiency of piezoelectric generators is fundamentally limited by the piezoelectric properties of the material. The efficiency of electrostatic generators is reduced by technical challenges relating to charging the electrodes, the separation distances and the amplitudes of displacement as described by Beepy (2012) [5].

1.2. Electrostatic transduction mechanism.

Electrostatic generators consist of a variable capacitors whose two plates are electrically isolated from each other by air, vacuum or an insulator. In the simplest case, external mechanical vibrations cause the gap between the plates to vary, and hence the capacitance changes. To extract energy, the plates must be charged, and the mechanical vibrations work against the electrostatic forces present in the device as described by Beepy (2012) [5].

Electrostatic generators can be either voltage- or charge-constrained. Voltage constrained devices have a constant voltage applied to the plates; therefore, the charge stored on the plates varies with changing capacitance. This typically involves an operating cycle that starts with the capacitance being at a maximum value (i.e., the plates being at their closest). At this stage, the capacitor is charged up to a specified voltage from a reservoir while the capacitance remains constant as described by Knight (2008) [7]. The voltage is held constant while the plates move apart until the capacitance is minimized (C_{min}). The excess charge flows back to the reservoir as the plates move apart and the net energy gained is given by and as described by Beepy (2012) [5].

Charge-constrained devices use a constant charge on the capacitive plates; therefore, the voltage will vary with changing capacitance. The plates are initially charged when the variable capacitance is at a maximum (plates closest together). As the capacitor plates separate, the capacitance decreases until C_{min} is reached, and, since the amount of charge is fixed, the voltage across the plates increases. The initial charging can originate from a reservoir controlled by the system electronics and the initial charge is returned to the reservoir at the end of the cycle. Alternatively, a fixed charge can be obtained using electret materials, such as Teflon or Parylene. In either case, the mechanical work against the electrostatic forces is converted into electrical energy. In either case, V_{max} must be carefully chosen to be compatible with the associated electronics and its associated fabrication technology. These two approaches have different strengths and weaknesses. The constant voltage approach produces greater energy levels but requires the electronics to provide a charging voltage of a different value to that used by the system electronics, which are powered from the reservoir. This requires a dual voltage system, but, since the precharging voltage level affects the damping in the generator, it is possible to use this approach to adjust its dynamics to suit different excitation characteristics. The charge constrained case produces less power but is simpler to precharge the plates to a voltage less than V_{max}.

A third hybrid approach suggests to operate the generator in the charge-constrained mode but place a fixed capacitance in parallel as stated by Knight (2008)

[7]. In this case, the energy from the charge-constrained system can approach that of the voltage constrained system because the parallel capacitance can be very large. The drawback of this approach is that more initial charge is required before the conversion process can begin; hence there are potentially more losses. Electrostatic generators can be broadly classified into three types shown in Figure 1.2: in-plane overlap varying, in-plane gap closing out-of-plane gap varying and voltage constrained as described by Zhu (2011) and Despesse (2005) [8, 9]. The relationship between the electrostatic force variation and the inertial mass displacement (x) for the three configurations is shown in Table 1.2 [5].

Table 1.2. Electrostatic force variation for the three configurations

Structure	Charge constrained	Voltage constrained
Out-of-plane gap varying	F_e constant	$F_e \sim 1/x$
In-plane overlap varying	$F_e \sim 1/x^2$	F_e constant
In-plane gap varying	$F_e \sim x$	$F_e \sim 1/x^2$

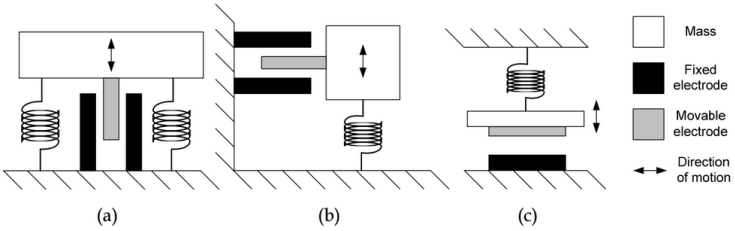

Figure 1.2. Types of electrostatic generators. a) In plane, overlap varying, charge constrained, b) In plane, gap varying (plan view), c) Out of plane, gap varying, voltage constrained, [8]

In the case of an electromagnetic generator, Beepy (2012) [5] stated that the damping coefficient arises from electromagnetic transduction. Some formulas are available for approximate evaluation of electromagnetic damping a more precise value for the electromagnetic damping can be determined by techniques such as finite element analysis (FEA). Electrostatic transduction is characterized by a constant force damping effect, denoted as coulomb damping, and a simple model is shown in Figure 1.3.

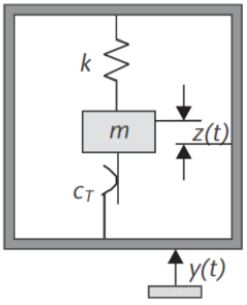

Figure 1.3. Model of an electrostatic resonant generator [5]

In [10] Wang et al. (2014) described an electrostatic energy harvester consisting of a four-wafers – glass base wafer, spacer, device wafer and top cap wafer. The 1 cm^3 volume device can operate in as low as 0.014 m/s^{-2} acceleration producing an output power of 1.2 μW. The second prototype was constructed taking advantage more advanced MEMS fabrication processes and described by Crovetto (2013) [11]. The experiments were done by exciting the device with vibrations from two perpendicular directions at harvester's resonance frequency. The power of 32.5 nW was achieved with an external electrical load of 17 MΩ with acceleration amplitude of 0.3 m/s^{-2} at a frequency of 179.5 Hz.

Zhang et al. (2016) [12] described an electrostatic energy harvester consisting of two cantilevers with their own proof masses suspended on top of each other. This results not in one, but in two resonant frequencies as the cantilevers where resonant frequencies of the cantilevers were 37 and 45 Hz. Moreover, the cantilevers were placed in respect to each other so that if one of the cantilevers is excited by its resonant frequency, it hits the other cantilever due to increased vibration amplitudes. Under vibration amplitude of 9.3 m/s^{-2} 6.2-9.8 μW, the power output was achieved in the frequency range of 36.3-48.3 Hz.

Suzuki et al. (2010) [13] have proposed an electrostatic vibration energy harvester with a passive, gap spacing, control method. The gap distance control in this case is used to avoid sticking the whole structure while in in-plane. Triboelectric properties of the material are used to create a repulsive electrostatic force between the different structures. In the generator application harvester with such structure separation demonstrated power output of 1 μW at acceleration of 2 g at 63 Hz excitation frequency. The drawback of such approach is the need to pre-charge the electrodes, which complicates the harvester design and requires an external power source.

The two main types of electrostatic transducers were described in this section – constant voltage and constant charge electrostatic transducers. Both methods have their pros and cons as in both cases the work is done against the electrostatic forces and it is converted into electrical energy. Constant voltage devices generate larger power output, but it requires quite sophisticated electronics to charge the plates to the required voltage, and the voltage required rarely coincides with the power supply voltage used by the controller. Furthermore, while the plate charging voltage affects the damping of the transducer, it allows to effectively regulate the transducers dynamic properties so that it meets the parameters of mechanical excitation. Constant charge devices generate lower power output, but the plates are charged much more easily. There also exist a third type of electrostatic transducers as a hybrid between the two latter types described in [7-9], but this type is less popular due to quite high charge levels required for charging the plates, which as the result increases the electrical loses of such devices quite significantly.

1.3. Electromagnetic transduction mechanism.

To date, most types of rotating generators have been based upon electromagnetic transduction techniques and used in numerous applications from bicycle dynamos to large-scale power generation. Kinetic energy harvesting can exploit rotary generators,

such as those found in the Seiko kinetic watches [5] or linear transducers that are used to harvest power from vibrations. Well-designed generators, which are not constrained in size, can be extremely efficient at converting kinetic energy into electrical energy.

Electromagnetic transduction mechanism produces comparatively high current but this is in trade off to voltage produced. Overall, this transduction mechanism has very few drawbacks as it does not require an external voltage source for electrodes and it does not have mechanical constraints. On the other hand, it scales-down poorly reducing its efficiency at micro-scale [8].

A comparison of different electromagnetic circuits and their relative merits were discussed by Suhaimi (2014) [14] and Warneke (2001) [15]. Yang et al. (2010) [16] have demonstrated an electromagnetic device consisting of a free-standing magnet that is suspended in a cavity formed from circuit board layers glued together and embedded with multi-layer copper coils. Two different designs were tested – without air holes and with air holes. Experimental results revealed that the device with no air holes produced lower voltage, but showed wider bandwidth and higher central frequency. This is explained by sever damping. The device with air holes demonstrated 9 mV voltage output and 40 Hz bandwidth (from 40 to 80 Hz) at 1,9 g acceleration, and the device produced 0.4 μW power output with an added 50 Ω electrical load.

Sardini et al. (2011) [17] have proposed a novel electromagnetic transducer. This device is dedicated for energy harvesting from low frequency vibrations (below 100 Hz). The problem of lowering the resonant frequency of the structure was tackled by using polymeric materials as resonators. The authors also offered a new magnet configuration that ensured an increase of spatial variation of magnetic flux. The device creates a relative movement between permanent magnets and planar inductors as described in [17]. Experimental investigation of linear device produced 290 μW at 100 Hz frequency, which results in approximately 0.5% effectiveness. The device with polymeric resonators demonstrated 153 μW at 40 Hz resonant frequency, which results in 3.3% efficiency. Using polymeric resonators, the resonant frequency of the device was reduced from 100 to 40 Hz and the energy harvesting efficiency increased from 0.5% to 3.3%. Sardini et al. (2011) [17] note that the submitted values are peak values instead of RMS.

Mahmoudi (2014) [18] presented a hybrid – a piezoelectric-electromagnetic energy harvester. The device consists of two PZT/Steel/PZT cantilevers joined in the middle by a permanent magnet, two coils are placed on top and on the bottom of the structure in parallel to magnet traveling path. In this case the cantilevers are used both for energy generation and guiding of the permanent magnet. As described by [18], "the principal benefits of this design are important reduction of the damping to enhance the harvested power and the exploitation of the active element nonlinear vibrations to significantly enlarge the harvester bandwidth". The primary resonant frequency of the hybrid was found to be 93 Hz. It is also noted that the elastic part (PZT cantilevers) contribution is negligible inside its linear dynamic range, thus the device must operate at high displacement amplitudes (Duffing amplitude) to take advantage of PZT layers. Duffing amplitude is well described by Juliliard (2008) [19]

and Kacem (2010) [20]. It was found that at 93 Hz excitation frequency, the piezoelectric transducer contributed up to 61% of total power output of the device while electromagnetic transduction accounted for the remaining 39%. The electromagnetic transducer results were compared to electromagnetic transducers using pure levitation. It was shown that the approach by Mahmoudi (2014) [18] produced 60% higher power density (932 $\mu W \cdot cm^{-3} \cdot g^{-2}$) and 29% increase in frequency bandwidth (153–198 Hz). This approach is particularly interesting since using two transduction mechanisms enabled the authors to eliminate some of the electromagnetic transducer drawbacks if operated single-handedly such as levitating magnet friction to the walls of the tube. Abed et al. (2016) [21] adopted this traditional approach to purely electromagnetic transduction mechanism and implemented a device consisting of multiple magnets creating a multi-degree of freedom (MDOF) vibration energy harvester. Two different cases were investigated – a device with two and three moving magnets. In the case of two moving magnets, the device operated at 5.1 Hz to 12 Hz bandwidth and normalized power of 10.4 $mWcm^{-3}g^{-2}$. The three-magnet device demonstrated 4.6 Hz to 14.5 Hz bandwidth and power output of 20.2 $mWcm^{-3}g^{-2}$.

Another approach – using external magnets and applying an axial load to a cantilever generator – was reported by Zhu et al. (2008) [22]. The tuning configuration is shown in Figure 1.4.

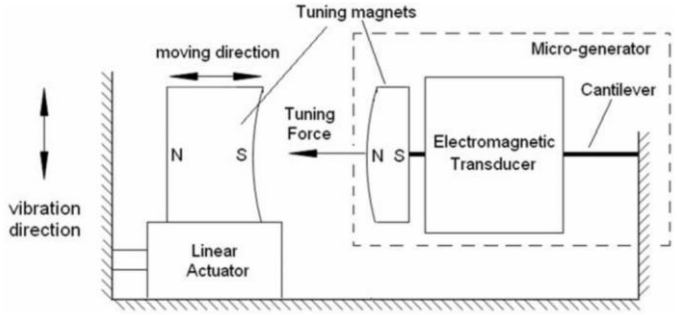

Figure 1.4. Schematic diagram of the tuning mechanism [22]

The axial force is applied by two magnets, one located on the end of the cantilever and one aligned next to it. The tuning magnets can be arranged to provide either a compressive force (magnets repelling) or a tensile force (magnets attracting). The force is altered by varying the distance between the two tuning magnets using a linear actuator. The tuning range of the microgenerator was 67.6– 98 Hz by changing the distance between two tuning magnets from 5 to 1.2 mm. More importantly, when used in the tensile mode, damping levels were unaffected. The University of Southampton has also developed electromagnetic generators based upon a cantilever spring arrangement. The earliest device comprised a pair of NdFeB magnets on a C-shaped core at the free end of the cantilever beam located either side of a coil wound from enamelled copper wire as described by El-Hami (2001) [23]. This early device produced >1 mW from a volume of 240 mm^3 at a vibration frequency of 320 Hz.

This generator was subsequently improved by adding a second pair of rare earth magnets forming the magnetic circuit by Glynne-Jones (2004) [25]. The improved flux linkage produced, for the same input vibration, more than twice the output voltage, and hence more than four times the instantaneous power. A smaller-scale version of this generator was developed during an EU-funded Framework 6 project VIBES by Beepy (2007) [24], and a cutaway of the optimized device is shown in Figure 1.5.

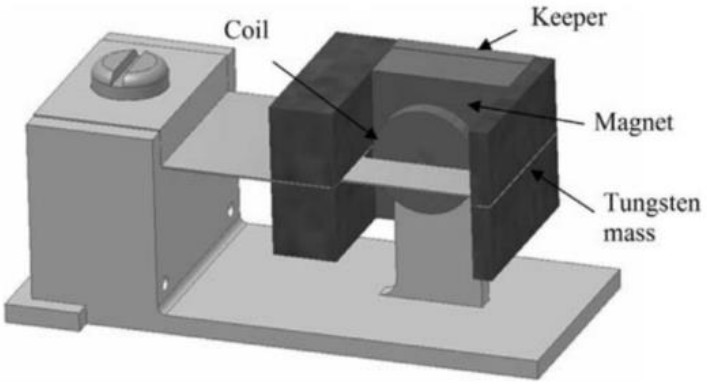

Figure 1.5. Cutaway (two magnets and keeper removed) of the mini size generator design [24]

This device is probably the smallest version of the device that can be practically assembled using conventional fabrication techniques (i.e., non-MEMS) and achieve a total packaged device volume of 850 mm^3 as described by Beepy (2007) [24]. The final version of this device uses a 50 μm thick beryllium copper beam and a coil with 2,800 turns wound from a 12 μm diameter wire with a coil resistance of 2,323Ω. The generator was designed to enable a manual frequency adjustment by altering the cantilever beam length. The power output into a 15-kΩresistive load was 50 μW at 1.1 V from 0.6 m/s^{-2} vibrations at 50 Hz. This device was demonstrated powering an autonomous wireless condition monitoring sensor system (ACMS). The generator was coupled to a voltage step-up circuit, the output of which was used to charge a 0.047 F capacitor. A low-power microcontroller was used to monitor the capacitor voltage and turn on the sensor system when sufficient energy has been stored.

A low-frequency inertial linear electromagnetic generator designed for human motion has been described by von Buren et al. (2007) [26]. The design consists of a tubular translator which moves vertically within a series of stator coils. The translator is made up of a number of cylindrical magnets separated by spacers, the dimensions of which were optimized using finite element analysis. The optimum resonant frequency of the generator varies from 5 Hz to 10 Hz depending upon the location and the wearer. The prototype has a total device volume of 30.4 cm^3 and produced an average power output of 35 μW when located just below a subject's knee. The final type of the human-powered energy-harvesting approach covered here is the energy-harvesting backpack. This approach exploits the relative motion and forces between the wearer and the backpack with the inertial mass being provided by whatever is

being carried. This is a logical opportunity for energy harvesting since the mass is already present, provided the energy can be extracted without significant extra effort from the wearer. Two versions have been realized. The first version, developed by Rome et al. (2005) [27], comprises a backpack with the load supported on a separate frame using a linear bearing and a set of springs. The load is free to move vertically relative to the frame, and a rotary electric generator with a rack and a pinion was used to generate electrical energy. This backpack generated a maximum power of approximately 7.37 W but at a cost of 19.1 W metabolic power, resulting in increased fatigue for the user. The second approach uses piezoelectric straps made from PDVF to extract the energy [28]. Simulations predicted that the straps could generate 45.6 mW of power while carrying a 45 kg load at a walking speed of 2–3 mph.

To conclude, the electromagnetic transducers demonstrate quite high levels of generated current, but in expense of generated voltage. Such a device does not require an external source of power to operate, but the amount of generated energy is directly proportional to the size of the transducer, mainly because a magnet is required. Zhu (2011) [8] have proved that the effectiveness of electromagnetic transducer decrease dramatically when going from macro to micro scale. Finally, due to the need of permanent magnets, electromagnetic transducers cannot be easily integrated into MEMS devices.

1.4. Piezoelectric transduction mechanism.

As described in [29], when a poled piezoelectric ceramic is mechanically strained, it becomes electrically polarized, producing an electric charge on the surface of the material. This is one of the two fundamental properties of piezoelectric material – the direct piezoelectric effect. The second one is referred to as the reverse piezoelectric effect and is exactly the opposite of the direct piezoelectric effect. As the piezoelectric material is deformed, charges are generated. These charges can be collected and transferred using electrodes attached on the surface of the piezoelectric material normal to deformation vector. As described in [29], the constitutive equations attributed to the piezoelectric property are based on the assumption that the total strain in the transducer is the sum of mechanical strain induced by the mechanical stress and the controllable actuation strain caused by the applied electric voltage. For reference, 3 axis system is used for the piezoelectric materials. It is illustrated in Figure1.6.

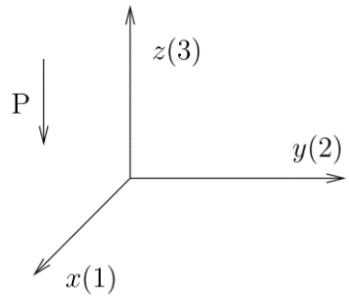

#	Axis
1	x
2	y
3	z
4	Shear around x
5	Shear around y
6	Shear around z

Figure 1.6. Axis nomenclature [29]

Piezoelectric materials have been used for many years to convert mechanical energy into electrical energy. Piezoelectrics contain dipoles, which cause the material to become electrically polarized when subjected to mechanical force. The degree of polarization is proportional to the applied strain. Conversely, an applied electric field causes the dipoles to rotate, which results in the material deforming. The piezoelectric effect is found in single crystal materials (e.g., quartz), ceramics (known as piezoceramics) (e.g., lead zirconate titanate (PZT)), thin-film materials (e.g., sputtered zinc oxide), screen printable thick films based upon piezoceramic powders and polymer materials such as polyvinylidene fluoride (PVDF) as described by Beepy (2000) [30]. Such materials have anisotropic piezoelectric behaviour. This means that the properties of the material differ depending upon the direction of the strain and the orientation of the polarization (and therefore, the position of the electrodes). For example, the 3 directions refers to piezoelectric materials that have been polarized along their thickness (i.e., having electrodes on the top and bottom surfaces). If a mechanical strain is applied in the same direction, the constants are denoted with the subscript 33 (e.g., d_{33}). If the strain is applied perpendicular to the direction of polarization (e.g., the 1 direction), the constants are denoted with the subscript 31 (e.g., d_{31}). These are illustrated in Figure 1.7 from [8], but for a more complete description, a reference is made to the IEEE standards (1987) [31].

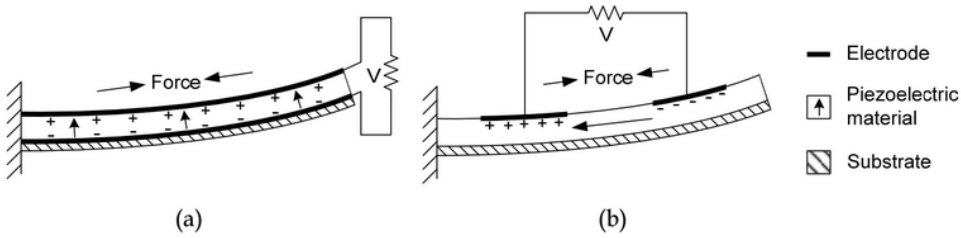

Figure 1.7. Two types of piezoelectric energy harvesters (a) d_{31} mode and (b) d_{33} mode [8]

Transducers utilizing the piezoelectric effect were extensively studied by different authors. Beepy (2006) [32] have presented an extensive comparative study of piezoelectric transducers with electromagnetic and electrostatic devices. Sirohi (2000) [33] has extensively studied the behaviour of piezoelectric elements in sensor modes. Sodano and Inman (2004) [34] have focused on developing a model to predict the amount of power capable of being generated through the vibration of a cantilever beam with attached piezoelectric elements. This work was one of the first attempts to create a reliable model to be applied with different boundary conditions and layouts of piezoelectric patches [34]. Electromechanical modelling of cantilevered energy harvesters is extensively studied by Erturk (2009) [35].

Mello (2014) [36] have focused on optimization techniques for piezoelectric transducers. Topology optimization method was adopted to maximize the harvesters output voltage with the requirement of quasi-static operation. Nakasone (2010) [37] have used the topology optimization method to maximize the electromechanical

coupling factor for the harvester operating at higher vibration modes. Optimal polling directions were found to avoid cancelation of charge to higher vibration mode shape but did not solve the problem of finding the normal strain nodal point to maximize the power output from harvesters operating in higher mode shapes. Ashraf (2013) [38] presented a bounded nonlinear vibration energy harvester fit to operate in a wide range of low frequency vibrations utilizing mechanical stoppers. The wideband range was achieved by the frequency-up conversion method as the harvester beam contacting the mechanical stopper seismic mass movement within the elastic limits of the spring was confined. Experimentally proven modelling results show that a device can efficiently operate in a range from 10 to 18 Hz with 65.74 μW cm3 power density at 10 Hz and 341.68 μW cm^3 at 18 Hz. The drawback of narrow bandwidth has also been addressed by Li (2010) [39] who have introduced an energy harvester with an L-shaped proof mass.

The narrow bandwidth problem can be also tackled by developing multimodal devices which could resonate not at one but at multiple frequencies, thus increasing the operational frequency range of such a device. One example of such a device is a multi-modal energy harvester offered by El-Hebeary (2013) [40]. The device is a "delta" or "V" shaped plate with multiple magnets fixed to it. The device was shown to have three prevailing frequencies – 7.9, 12.3 and 18.7 Hz with peak power densities of 2 mW/cm^3 at 7,9 Hz, 1,45 mW/cm^3 at 12,3 Hz and 0,4 mW cm^3 at 18,7 Hz. For a V-shaped plate and two magnets, the prevailing frequencies were 8,1 Hz and 12,5 Hz with peak power densities of 2 mW/cm^3 at low end of bandwidth and 1,4 mW/cm^3 at high end. Bai et al. (2014) [41] have developed a multi-modal energy harvester using a different approach, i.e., a spiral-shaped cantilever with tip mass in the form of magnets coupling with a magnetoelectric transducer. The achieved bandwidth was from 15 Hz to 70 Hz with 5 concentrated frequency peaks.

Vibration energy harvesting can also be divided into three different fields:

- Impact or shock energy harvesting when the energy is gathered from "pulses" of energy which are high in amplitude and acceleration. They last very shortly and are quite random in nature. Such impact energy can be harvested by resonant or non-resonant systems.
- Harmonic vibrations. Such vibrations have a constant amplitude and frequency. Thus, devices with a very narrow band of resonant frequency may be used. Non-resonant devices are not efficient in such applications. Such vibrations are very rear in nature and can only be found in human made sources (motors, engines, mechanisms).
- Random or ambient vibrations. This vibration source has very random amplitudes and frequencies. In such cases, devices with wide resonant frequency band or tunable devices may only be used.

Electro-mechanical energy conversion mechanism is described by Erturk (2009) [42] and illustrated in Figure1.8. This conversion mechanism is controlled by constitutive laws described by Sirohi (2000) [33] and fundamental relations of mechanics of materials described by Rezaeisaray (2015) [43]. A charge is the integral of the normal component of electric displacement over the electrode area, and the electric displacement field generated in the piezoelectric layer during vibration is a

function of the strain distribution over transducer length as described by Bucciarelli (2009) [44]. A charge cancelation is possible if the piezoelectric material is bonded on a transducer surface that is undergoing deformations of higher vibration modes as discussed by Erturk (2008) [45]. In higher vibration modes, a certain strain node exists where the deformation field changes the sign. This strain node can be find from modal analysis of the cantilever. Erturk (2009) [42] have conducted a detailed research on how to avoid the problem of charge cancelation and find the strain nodes as well as segmentation techniques, but in this case modal analysis results were used for investigation of the mode shapes for displacement and normal strain. In addition to the conventional vibration energy harvesting from harmonic vibrations in resonant or off-resonant mode, there was a series of harvesters dedicated to impact energy harvesting as described by Kang (2008) and Cady (1946) [46, 47] which is a type of a non-linear generator. The aspects of modelling contact dynamics were thoroughly investigated by Djuguma (2009) [48].

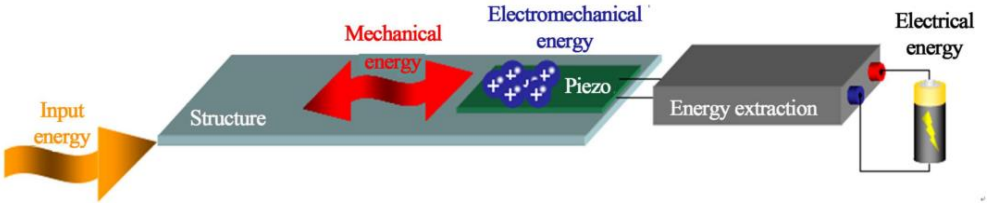

Figure 1.8. Schematic representation of electromechanical energy conversion in energy harvester [42]

Figure 1.9 shows the concept of artificial hair cell proposed by Hana (2012) [49]. The hair structure is mounted on a flexible printed circuit board (FPCB). The piezo resistive sensing element made of the CNT-PDMS composite is embedded in the bottom region of the hair structure because the maximum stress and, consequently, the maximum strain is applied on the region where the structure is bent by an external force. The horizontal and vertical cross sections of the sensing element are depicted in Figure 1.9(b) and 13(c), respectively. The sensing element is composed of three piezo resistive sensing resistors (R1, R2 and R3) and one common resistor (R0) as shown in the equivalent electrical mode in Figure 1.9(d).

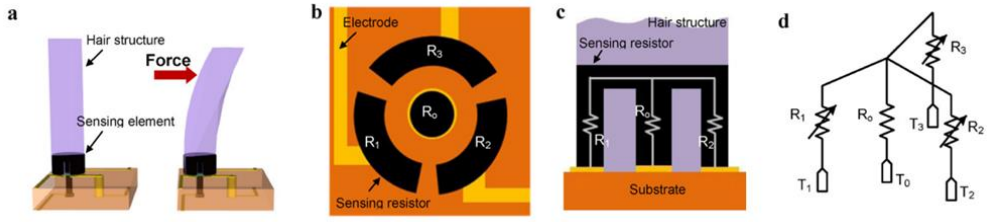

Figure 1.9. (a) Schematic view of proposed hair sensor device. (b) Horizontal and (c) vertical cross section of sensing element. (d) Equivalent electrical model of sensing element [49]

The common resistor is located at the bottom centre of the cylindrical hair surrounded by three sensing resistors as shown in cross sectional views. The bottom sides of the four resistors sitting on top of metal electrodes become measurement terminals that allow measurement of the resistance of individual sensing resistors. The other sides of the resistors are connected to each other at a single node inside of the hair structure. The three sensing resistors, R1, R2 and R3 have the same initial resistance. When a force is applied on the hair, the bending of the hair will deform the sensing resistors resulting in the strain-induced resistance changes. In contrast, the common resistor is located at the centre of circular hair structure. When the hair is forced to the right direction in Figure 1.9(c), the left part of the common resistor is in tension and the right part is in compression with the neutral surface of zero stress in the middle of cylindrical structure for homogeneous material.

Zhu (2010) [50] developed a novel miniature wind generator for wireless sensing applications. The device consisted of a wing exposed in an airflow with a magnet attached on top of it and a bluff body. As the wing is exposed to the airflow, it bends backwards, and as the bending amplitude reaches the bluff body, the pressure created by the airflow is relieved and the wing bends backwards. As the frequency of this oscillation reaches the natural frequency of the structure, the device operates in a resonance mode. Although the dimensions of the device were of centimetre scale (120 x 80 x 65mm), the produced power was just 470 μW at 2,5 ms^{-1} wind speeds, and with 5 ms^{-1} wind speed, the power output achieved was 1.6 mW, which is more than enough for sensing application and wireless transmission of the recorded data. The device is shown in Figure 1.10.

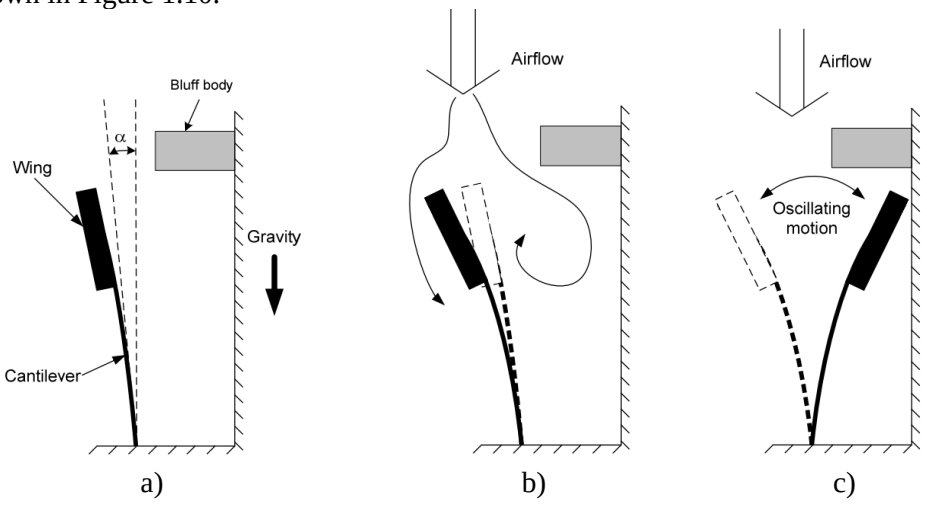

Figure 1.10. Principle of the energy harvester from [50] a) No airflow, initial bending due to gravity, b) Cantilever bent due to air flowing, c) Cantilever sprung back

To conclude, the piezoelectric transduction mechanism is the most promising one due to its simplicity and quite high efficiency (5-20 %). Since the efficiency is highest when the transducer, i.e., the cantilever type piezoelectric energy harvester, operates in resonance mode, it is necessary that the fundamental frequency of the transducer would match the ambient frequency. This is one of the main drawbacks

that has to be overcome since the frequency of ambient vibrations is rarely stable. It is also quite difficult to decrease the fundamental frequency of the cantilevered energy harvester to the desired frequency, which also results in decreased efficiency. Different tuning and optimization techniques shall be reviewed to overcome these drawbacks.

1.5. Mechanical Tuning.

It is a common concept that micro-scale devices will harvest less energy than larger-scale systems. Furthermore, the efficiency of the transduction process is affected by issues with scaling. Finally, as generators are made smaller, the resonant frequency of the system tends to increase. It is, therefore, challenging to realize a MEMS generator, which is tuned for applications on machinery at around 100 Hz. Frequency tuning can be classified as either continuous or intermittent [5]. Continuous tuning includes any approach that is applied constantly to the generator. Intermittent tuning refers to the tuning methods that can be periodically activated to adjust the generator frequency and, when the desired value is reached, the tuning mechanism is turned off. Intermittent tuning consumes less energy than continuous tuning and is, therefore, the preferred option. Roundy (2002) [51] stated that it is impossible to gain a net increase in power generated using continuous frequency tuning mechanisms since the energy needed to run them will exceed an increase in power output generated by them. This, however, has been shown not to be the case by Zhu (2010) [52]. Therefore, both approaches are valid. The suitability of different tuning approaches depends upon the nature of the application. Different approaches can be analysed by considering:

- The energy consumed by the tuning mechanism (should be minimized and must not exceed the energy produced by the generator);
- The range of frequencies achieved;
- The degree of frequency resolution;
- Its effect on damping levels over the entire operational frequency range (ideally no effect).

Tuning can be achieved by mechanical techniques, which change the mechanical properties of the structure in some manner, or by electrical tuning that exploits the influence of the electrical output load. Some mechanical approaches to frequency tuning will be considered next.

Most vibration energy-harvesting devices are based on a cantilever spring structure, which can be used to highlight the possibilities for mechanical tuning. The principles described are generally applicable to all types of mechanical resonator structures. Mechanical tuning can be achieved by:

- Altering the dimensions of the beam;
- Moving the centre of gravity of the proof mass;
- Varying the spring stiffness;
- Straining the structure.

The mechanical approach can include changing the dimensions of the system, moving the centre of gravity of the proof mass, varying the spring stiffness and straining the structure to impact its performance. The length of the cantilever can be

altered, for example, by altering the clamp position, and thus changing the distance from the fixed end l to the free end, as a result mass m is also changing and as well the resonant frequency f_r. In [52], it is shown how the ratio between the original length and the altered cantilever length impacts the resonant frequency. The length of the cantilever is directly responsible for the change in cantilevers resonant frequency, i.e., the shorter the cantilever, the higher the resonant frequency, and the longer the cantilever, the higher the resonant frequency as described by Zhu (2010) [52].

Similarly, the centre of gravity of the added proof mass can be used for tuning the resonant frequency of the device. The detailed mathematical explanation of this method can be found in [53]. An example of such method could be Wu et al. (2008) [53] who have reported a piezoelectric energy harvester that consisted of a rectangular cantilever with a proof mass (10 x 12 x 38 mm) on the free end of the beam with a movable 30mm long M6 screw. The team could tune the resonant frequency of the device from 180 Hz to 130 Hz by moving the screw from one end to another as shown in Figure 1.11 As expected, the output voltage dropped when resonant frequency increased. This method is recognized for good tuning resolution but requires sophisticated mechanisms for real time tuning.

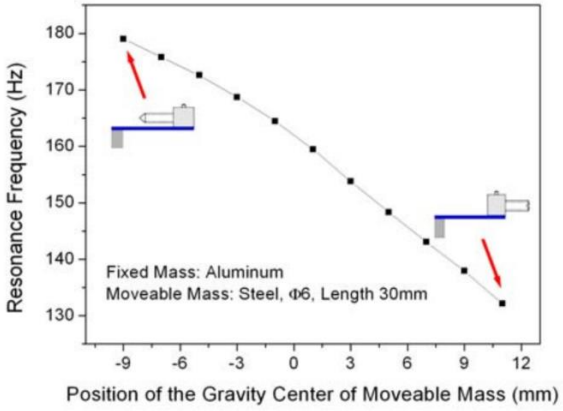

Figure 1.11. Experimental result of frequency adjustment [53]

Another approach is to vary the spring stiffness by placing an adjustable spring (k_a) in parallel with the mechanical spring (k_m). It can be outlined that this method always requires additional components other than cantilever and proof mass to operate, and they usually require quite high voltages to operate meaning the power output is reduced by power consumed for operation of the tuner.

One of the best examples of increasing energy collection time by increasing the bandwidth of the harvester is the work of Bendame et al. (2015) [54] as shown in Figure 1.12. The authors have developed a device based on piecewise-linear oscillators. The device has a stopper to tune the stiffness ratio of the oscillator and the velocity of the moving object at the point of impact with the stopper. The authors tried to reach the best effective mass m and stiffness k ration as well as decrease the damping ratio. The authors developed a procedure to optimize the wideband MPG's and found out that the optimization requires two additional steps to traditional

technique of minimizing mechanical energy losses through damping. Dominant factors determining the performance of MPG's were stiffness ration ρ^2 and the velocity of the structure at the point of impact. Both factors are controlled by changing the position of the stopper, the height or the distance from the fixing point of the cantilever. In conclusion, although the design of the wideband MPGs is more challenging than that of regular MPGs, they offer significant performance improvements justifying the added design costs. Specifically, wideband MPGs can be 'tailored' to better fit the environmental vibrations, thereby maximizing the harvested energy.

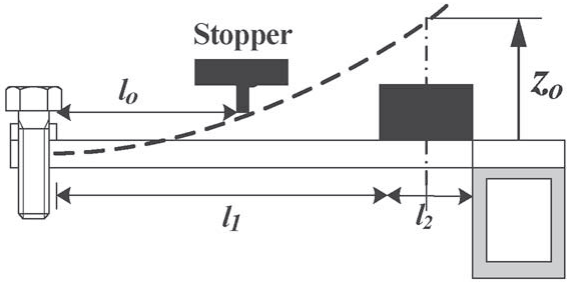

Figure 1.12. Schematic representation of wideband MPG by Bendame et al. (2015) [54]

The other approach is by Khym et al. (2004) [55]. The authors presented impact-based frequency up converted wide band piezoelectric harvester's system at which two high frequency operating beams are struck at the same moment by a low frequency driving beam with a tip mass. In such a way, a big mass low frequency beam transfers its kinetic energy to high frequency low mass cantilevers exciting them in their resonant frequencies. The change of the driving beams' stiffness during the contact allows the device to broaden its bandwidth by ~170% and additional gain of energy by 61 % in vicinity (from 7 to 10.5 Hz). The efficiency of power transfer is increased to approximately 85%. Each generator beam produces 377 μW peak power at 14.5 Hz under 0.6 g acceleration with the corresponding power density of 58.8 $\mu W/cm^{-3}$ as described by Khym et al. [55].

The other method for tuning the resonant frequency is variable spring stiffness. It is commonly used because it can be achieved through various methods: electrostatic, piezoelectric, magnetic or thermal mechanisms. Most of variable spring stiffness devices are continuously operated. Many examples of electrostatic tuning have been demonstrated in tunable micromechanical resonators and have not necessarily been applied to vibration energy generators as described by Adams (19995) and Charnegie (2007) [56, 57]. Electrostatic generators can be tuned by adjusting the voltage on the plates, as discussed earlier. The presence of the inertial mass in an energy harvester reduces the tuning effectiveness and increases the power required for tuning. Piezoelectric tuning has been demonstrated by using two piezoelectric elements on the energy harvester spring element. One of these elements

is used to harvest the energy, while, as described by Roundy (2004), the other element has a tuning bias applied to it. Thermal techniques utilise the variation in Young's modulus of the spring material with the temperature or the thermal expansion of the material. This approach, however, requires relatively high powers and is thus avoided in practical energy harvesting applications.

Magnetics have been used to alter the spring stiffness by applying external forces to the device. For example, the resonant frequency of a cantilever structure can be tuned by applying an axial load. The resonant frequency of a uniform cantilever with an associated buckling force, F_b, operating in the fundamental flexural mode with an axial load, F (positive for a tensile load and negative in the compressive case), is given by Blevins (2001) [59].

From the last section, there are ways to increase the efficiency of piezoelectric transducers using the mechanical methods. These can be passive or active, but usually these include some drawbacks like the need for an external power supply and active control, increased device volume, etc. Nevertheless, in most cases the mechanical methods grant significant increase in generated energy.

1.6. Electrical tuning.

Electrical tuning is achieved by changing the value of electrical load and electrical damping that is directly related. It is difficult or impossible to achieve electrical tuning on electrostatic or electromagnetic transducers. Thus, only piezoelectric transducers are reported to be electrically tuned. The electrical tuning of piezoelectric transducer is achieved by changing the capacitance parameter. As reported by Beepy (2012) [5], basic bimorph piezoelectric cantilever generator can be represented with an equivalent circuit, as shown in Figure 1.13.

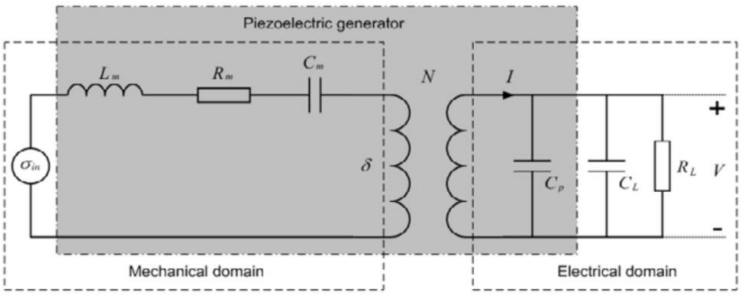

Figure 1.13. Equivalent circuit of the piezoelectric generator with capacitive and resistive loads, where L_m, R_m, and C_m represent the mass, damping, and spring in the mechanical part, respectively, and C_p is the capacitance of the piezoelectric layer. C_L and R_L are the capacitive and resistive load, respectively, and V is the voltage across the resistive load [5]

The transformer relates the mechanical domain to the electrical domain according to the model of the piezoelectric effect. For a piezoelectric bimorph, which operates in the 31 modes, ε is the dielectric constant of the piezoelectric material and E is the Young's modulus of the piezoelectric material. Figure 1.14 compares the resonant frequencies and power output of electrically tunable piezoelectric generators

of different piezoelectric materials with varying load capacitances. Piezoelectric materials with a higher Young's modulus, strain coefficient and lower permittivity provide a greater tuning range. Figure 1.14 shows that PZT-5A is the best of the four piezoelectric materials [52].

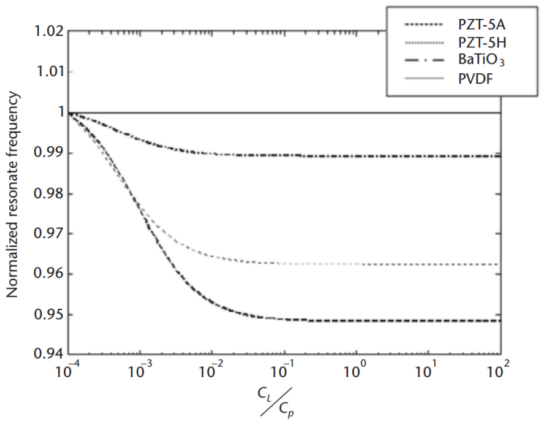

Figure 1.14. Change in the resonant frequency of a piezoelectric generator with different piezoelectric materials [52]

Electrical tuning was demonstrated by Wu et al. (2006) [60] with a piezoelectric bimorph cantilever. One piezoelectric layer was used for frequency tuning, while the other layer was used for energy harvesting. Varying the load capacitance achieves a frequency variation of 3 Hz varying from 91.5 Hz to 94.5 Hz. A similar approach was demonstrated by Charnegie (2007) [57], and again one piezoelectric layer was used for energy harvesting, while the other is used for frequency tuning, as shown in Figure 1.15.

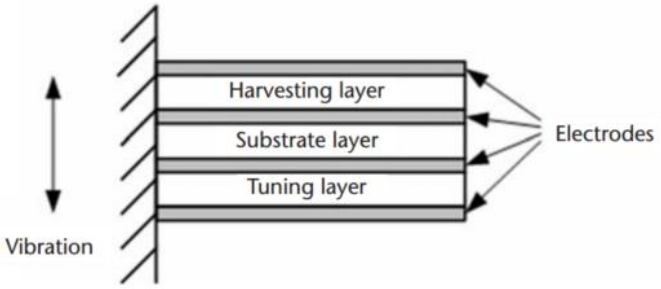

Figure 1.15. Piezoelectric bimorph used for electrical frequency tuning [60]

Test results show that the resonant frequency can be tuned by 4 Hz with an untuned frequency of 350 Hz by adjusting the load capacitance from 0 to 10 mF if only one layer is used for frequency tuning. In this case, the output power remains constant, irrespective of the load conditions. If both layers are used for frequency tuning, then the same range of load capacitance was found to achieve a tuning range of 6.5 Hz. In this case, however, the output power decreased with increasing load capacitance. Electrostatic tuning has been demonstrated in a MEMS resonator by

Adams (1995) [56]. The resonator is not designed for energy harvesting but demonstrates the feasibility of electrostatic tuning with a resonant frequency of 25 kHz and a tuning range from 7.7% to 146%. It uses the single comb structure shown in Figure 1.15 and a tuning voltage ranging from 0 V to 50 V. This is an example of continuous tuning and compatible with energy harvesters employing comb drive structures. It should be noted, however, that the greater the mass of the resonator as would typically be the case in an energy harvester, the less the frequency range can be adjusted.

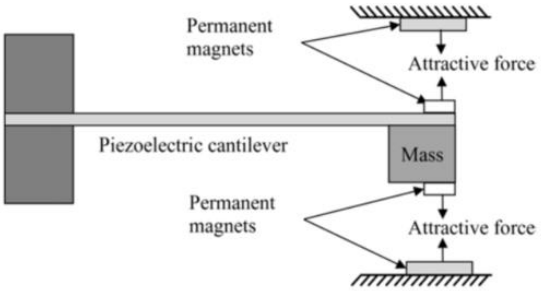

Figure 1.16. Schematic of the tunable piezoelectric generator [61]

The use of external forces, applied by external magnets, was demonstrated by Challa (2008) [61] who reported an intermittently tuned piezoelectric microgenerator. The device has an untuned frequency of 26 Hz and a frequency range of 22–32 Hz. The tuning was realized by applying an attractive magnetic force perpendicular to the cantilever generator, as shown in Figure 1.16. The magnitude of the force can be altered by varying the distance between the two sets of tuning magnets, but it should be noted that the tuning mechanism had the unwanted side effect of also varying the parasitic damping over the frequency range.

1.7. Strategies to broaden bandwidth.

Traditional piezoelectric transducers employ the first mode shape for energy harvesting. The frequency of the first mode shape is the lowest, but the vibration amplitude is the highest and the frequency band comparatively narrow [8, 9]. High vibration amplitudes are a drawback due to increased loads on brittle piezoelectric ceramics and bigger volume of the device. Narrow bandwidth limits the possibilities of use for such device since the ambient vibrations have very wide and varying frequency spectra. Different techniques have been used by authors to widen the frequency band-width of the piezoelectric energy harvester, some of which are reviewed in the following chapter. A graphical summary of techniques for broadband increase are shown in Figure 1.17.

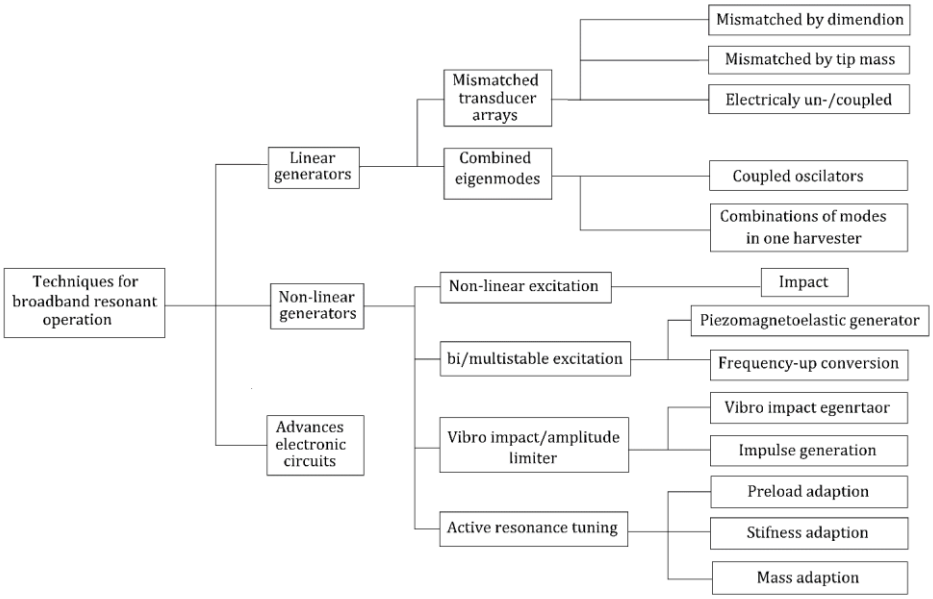

Figure 1.17. Overview on commonly used broadband techniques for vibration energy harvesting

One of the methods for increasing the bandwidth is to use a mechanical stopper to limit the amplitude of the generator as described by Abed et al. (2016) [62]. The generator strikes the end stop, and this is found to increase the bandwidth of the device as the frequency slowly increases. It does not appear to work when the frequency is reduced.

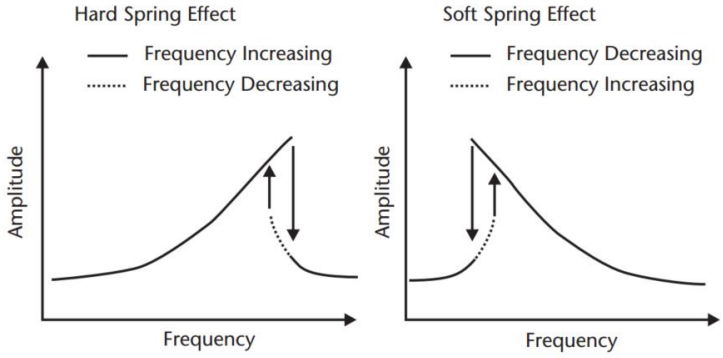

Figure 1.18. Hard and soft spring effects [5]

Nonlinear generators utilise the spring stiffening or spring softening effect, whereby the resonant frequency varies as a function of amplitude (see Figure 1.18). The spring stiffening (or hard spring) effect means that the resonant frequency increases with amplitude. Such nonlinear devices have a larger bandwidth over which power can be harvested due to the shift in the resonance frequency. As with the

mechanical stopper approach, a generator demonstrating a hard spring nonlinearity will only increase its bandwidth as the frequency increases and will have no effect for decreasing frequencies (vice versa for the soft spring effect).

Bistable structures (known as the snap-through mechanisms) can also be used for vibration energy-harvesting applications. Such structures effectively snap backwards and forwards between two stable positions at any frequency, provided that the acceleration stimulus is of a sufficient magnitude. The stored elastic energy has the effect of increasing the velocity of the structure for a given input excitation, and analysis reveals that the amount of power harvested by a nonlinear device is $4/\pi$ greater than that of the tuned linear device operated out of resonance. Bistable transducers have been investigated employing buckled spring-mass architecture to increase the bandwidth of the harvester as described by Bucciarelli (2009) [44]. Suhaimi (2014) [14] described a mechanism consisting of combined nonlinear hardening and softening mechanism which was aimed at widening the bandwidth as well as amplifying the low human motion frequency. This was achieved by adopting a translation to rotation motion converter. Nonlinearity was achieved by using mechanical and magnetic springs. Low frequency human motion was targeted in this research. Sardini (2011) [17] has described a method to increase the bandwidth of electromagnetic device by placing magnets on top of polymeric cantilever beam increasing the spatial variation of magnetic flux and changing the damping parameter. The harvester consisted of a conventional cantilever positioned on a flexible body beam. It was able to harvest energy from the first three vibration modes of the device with a large frequency spacing between the first mode (at 8.7 Hz) and the second mode (at 55.8 Hz). Mahmoudi (2014) [18] presented a hybrid piezoelectric/electromagnetic transducer bandwidth which was increased by exploiting nonlinear vibrations. The bandwidth of 153 Hz to 198 Hz was achieved. The L-shaped beam-mass structure investigated by Mahmoudi (2014) [18] could achieve harvesting energy from the first two vibration modes with $\omega_2 \approx 2\omega_1$, while the third and the higher modes are far removed from the first two modes. Kacem (2010) [20] and Abed (2016) [21, 62] proposed multi DOF devices or investigated bistability or multistability [20] but designing a multi-degree of freedom vibrating structure in MEMS is more challenging due to the microfabrication limitations.

Yang et al. (2015) [63] investigated an electromagnetic harvester based on a suspended beam with three permanent magnets (see Figure 1.26). The proposed design can harvest energy under three environment vibration frequencies of 369 Hz, 938 Hz and 1184 Hz, respectively. Suzuki et al. (2010) [13] exploited an asymmetric gammadion spring as the vibration resonator to achieve multiple frequency energy harvesting corresponding to the resonant frequencies of 110 Hz, 165 Hz and 243 Hz, respectively. Since the frequencies of typical ambient vibrations are lower than 100 Hz, it is more meaningful to achieve multiple modes in this low frequency region. A V-shaped energy harvester with multiple magnets was presented by El-Hebeary (2013) [40] who analysed the geometries of the V-shaped plate and the locations of the magnets in order to control the resonant frequencies and their spacing. This harvester can obtain three natural frequencies in the range from 8 Hz to 19 Hz but needs multiple energy conversion structures (multiple sets of magnets and coils).

A schematic diagram of the proposed multimodal vibration energy harvester by Bai (2014) [64] is shown in Figure 1.19. It consists of a spiral shaped cantilever beam, four permanent magnets, a ME transducer and a height adjustable holder. The spiral cantilever with the same width and thickness acts as the resonator of the harvester; and four permanent magnets are arranged and positioned at the innermost layer of the spiral beam acting as the proof mass. The ME transducer fixed on the holder is fabricated by one piezoelectric layer bonded between two magnetostrictive layers. Both the spiral beam and the holder are fixed on the housing of the harvester, and the energy conversion is achieved based on the relative movement of the magnets and the ME transducer.

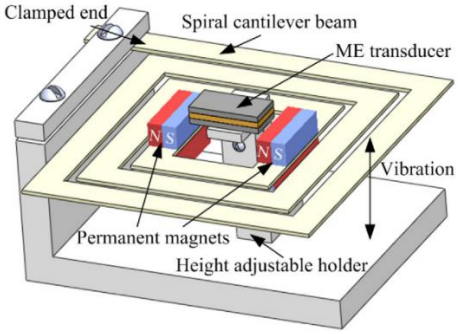

Figure 1.19. Schematic diagram of non-linear vibration energy harvester from [63]

Impact induced vibrations are another method for bandwidth increasing. During an impact, not only the first natural vibration mode but also higher natural modes are excited. So after the impact, the cantilever shape may be represented as a superposition of the first and higher natural modes. The frequency of the body impacting to the actual harvester is only important for higher energy density, but the harvester will always vibrate in its natural frequency. This phenomenon enables frequency-up converting devices. High frequency harvesters can be used for energy harvesting from low frequency vibrations. Therefore, higher modes of the harvester can be excited due to random varying frequency or impulse-type excitations generated by ambient vibration sources. Dauksevicius (2013) [65] presented a frequency up converting harvester consisting of a high frequency energy harvester and a low frequency resonator. The low frequency resonator was vibrating under low frequency harmonic base excitation of 18.8 Hz and under the maximum vibration amplitude impacting a high frequency harvester forcing it into resonant vibrations of 374 Hz. 4 Hz bandwidth of LFR was achieved at 0.5g acceleration. Frequency-up converting device capable of harvesting low frequency wide band vibrations and utilizing mechanical stops was developed by Ashraf (2013) [66]. The device was proven to operate in frequency band from 10 Hz to 18 Hz.

Abed (2016) [62] has designed a system of magnetically coupled cantilevers. The device demonstrated a significant 130% increase in bandwidth. Frequency-up converters can be design with a magnetic or mechanical coupling. The most significant drawback is that the devices that are the ferromagnetic elements further

increase the volume of the device, thus decreasing the output energy density. Yang et al. (2011) [67] proposed a frequency-up converting harvester in which the frequency-up conversion phenomenon is achieved by magnetic repulsion forces. As the main advantage of a magnetically coupled device is the non-contact coupling, this theoretically could prolong the lifetime of the device. One more example of a magnetically coupled device is provided by Najafi (2008) [68]. It is an electromagnetic energy harvester which consists of cantilevers with magnets and coils on top of the resonating cantilevers. The device was proven to generate up to 170 nW of power in ambient vibration range of 10 Hz to 100 Hz.

The biggest drawback of low frequency harvesters is the vigorous vibration amplitude. This drawback was tackled by Li (2015) [69] who investigated the feasibility of using a rectangular piezoelectric bistable laminate vibrating in its second resonant mode. The second mode was chosen to avoid extremely large vibration amplitudes of a low frequency device. By adding a proof mass, the second natural frequency was lowered from 99 Hz to 65 Hz; and a bandwidth of 11 Hz was achieved. As described by Abed (2016) [62], the size of a low frequency harvester is the main reason behind low density of energy generated by it, since low resonant frequency is not achievable without relatively big proof mass added. Li (2016) [70] described a bi-resonant structure consisting of two piezoelectric cantilever harvesters with natural frequencies of 15 Hz and 22 Hz. As one of the harvesters entered a resonance mode, a dynamic contact was achieved between the two harvesters further increasing the power output. Bandwidth of 14 Hz was achieved at 1g acceleration. Li (2016) [71] continued the research of bi-resonant devices and designed a harvester tandem. With the centre frequency of the device being at 20 Hz, the bandwidth of 25 Hz was achieved. The frequency bandwidth of 12 Hz was achieved (from 10 Hz to 22 Hz). Sharvari (2015) [63] have proposed a nonlinear PVEH using a compliant orthoplanar spring (COPS) as shown in Figure 1.20. With the addition of lightweight masses at different locations, closed multiple nonlinear hardening resonances are obtained during the forward as well as the reverse sweep further extending the nonlinear PVEH bandwidth.

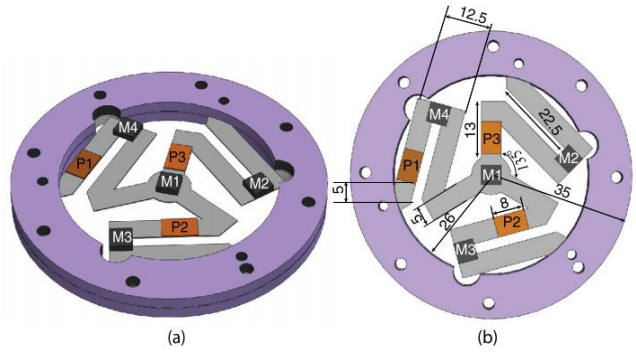

Figure 1.20. Schematic of the COPS-PVEH (all dimensions are in mm) [63]

In Figure 1.20, the P1, P2 and P3 are the locations at which the piezoelectric material segments were attached to measure the voltage outputs, while M1-4 denotes

locations at which four different masses were attached. The author noted that by adding the masses M1-4 the different modes were brought closer together; and the open circuit voltage output from piezoelectric segments P1-3 was increased. But this was done with a trade-off of the mass and volume of the device.

The Finite Element Modelling and structural optimization were developed in parallel with each other and are closely related. With recent breakthrough in FEM, structural optimization did not fall behind either. As described by Park (2007) [72], the linear static FEM problem is primarily solved in structural optimization; and structural optimization is classified according to the characteristics of the design variables and shown in 1.3 table. Due to complexity of the problems, the investigators are yet focusing on linear static problems. This leads to the need to reduce the complexity of the solved problems in case a dynamic problem is solved. This may sometimes lead to oversimplification of the problem, and thus to wrong results.

Table 1.3. Classification of structural optimization [72]

Structural optimization	Design variable
Size optimization	Design variables are thickness or section properties. The domain for FEM is fixed during optimization.
Shape optimization	Design variables are the shapes of structures. The domain for FEM is changed during optimization.
Configuration optimization	The transformation matrices of FEM are functions of design variables. Sometimes it is considered as shape optimization
Topology optimization	Design variables are the elastic modulus of the elements for FEM. The problem can be viewed as a material distribution problem.

In the investigation of the different strategies to broaden the bandwidth, a conclusion can be drawn that multi-DOF and frequency-up converting devices with impact coupling are among the most promising. The Frequency-up converting devices with magnetic coupling can be excluded to the sheer size of such devices, and the magnetic coupling is only achieved with magnets which increase the volume of the device significantly. Mathematical optimization is also among the most promising approaches.

1.8. Numerical models and methods of their analysis.

There are many different methods for analytical modelling of piezoelectric elements. In the next section, some models shall be reviewed briefly with their theoretical derivations and some examples from the literature reviewed.

The simplest model of a piezoelectric transducer for the thickness mode vibration is described by Fujiwara (192) [74], and can be directly obtained from the description of phenomena observed by Erhart (2016) [75]. Both authors discovered the difference of potential is proportional to the strain of a piezoelectric crystal.

The above-mentioned model requires the conversion of the mechanical part of the system into electric circuit using electro-mechanical analogies. It allows the whole electro-mechanical system to be analyzed using circuit theory-based methods.

Some of the simplest equivalent circuit models for a piezoelectrical harvester operating close to or at the resonant frequency is the model proposed by Van Dyke and described by Sherrit (1997) [76]. The simple Van Dyke model is frequently adopted for simulations of electromechanical resonance, for example, by Sedra (2003) [77]. The Van Dyke model is a capacitor connected in parallel to resistive, capacitive and damping elements, which in their turn, are connected in series. The components here represent the mass, mechanical damping and elastic compliance, in other words the electrical components mimic the most important mechanical properties. The capacitor represents here the electrostatic capacitance of two parallel plates of piezoceramics [78]. Even though the Van Dyke model is simple, it has its limitations, namely modelling materials with high losses as described by Sherrit (1997) [76] are highly inaccurate and unreliable. This drawback was tackled in a new model, the main difference between the previously described Van Dyke model and Sherrit model is that Sherrit (1997) [76] employs complex numbers instead of real numbers. This allows modelling of piezoelectrical materials with losses. Guan (2004) [79] noted that when a piezoelectric material is fixed on a mechanical structure (i.e., the cantilever), its boundary conditions are changed. As a result, the Van Dyke or Sherrit models are no longer accurate. Having this assumption in mind, Guan (2004) [79] developed a model for loaded piezoelectric ceramics with multiple resonant frequencies. An additional capacitor and a resistor branch are added if compared to the Van Dyke model.

For the loaded piezoelectric ceramics conditions, the Van dyke model was extended as described by Kim (2008) [80]. Multiple branches of RLC components were added to include the mechanical resonance modes in the extended Van Dyke model. In the extended Guan (2004) [79] model, each series RLC branch stands for mechanical resonance mode. The drawback of the Guam model is that it is difficult to determine RLC components values for resonance frequencies that are close or overlapping with each other as described in [79]. Kim (2008) [80] proposed a systematic procedure to model a piezoelectric ceramic (Easy Model), equivalent circuit model that can represent the electrical behaviours of unloaded and loaded piezoelectric ceramics. The main advantage of modelling the piezoelectrical transducer as a purely mechanical system is that the model can be developed without knowing the exact parameters of the materials. Only the measured impedance of the piezoelectrical material is needed. The model is also highly accurate as up to 99% average accuracy is reported for piezoelectric materials that are not mounted on a structure. For mounted piezoelectrical materials, the accuracy drops to 93% but that is still an impressive result.

The diagram of this model is shown in Figure 1.21 where x_1 and x_2 are the displacements of lumped masses m_1 and m_2, respectively k is the spring, F is the force exciting the mechanical part of the system, R is resistance and L is the induction of electrical circuit, and between mass m_1 and m_2 there is a piezoelectric transducer. The state space equations are useful for the simulations and development of control system. Erturk (2008) [81] have implemented single-degree-of-freedom modelling for of the harvester beam as it allows simple expressions for the electrical outputs. The well-known SDOF relation is employed for mathematical modelling. The authors

have shown a comparison between the Euler-Bernoulli and SDOF model predictions for harmonic excitation as well as corrections of the SDOF model for transverse vibrations. Proper corrections were also introduced for corrections factor in the electromechanically coupled SDOF equations.

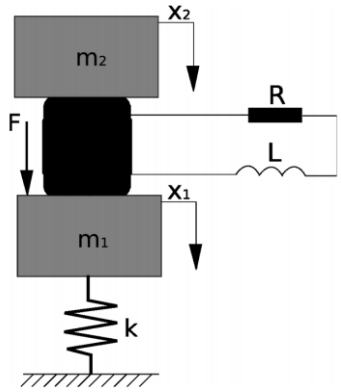

Figure 1.21. Two-degree of freedom mechanical system with piezoelectric element [5]

Erturk (2009) [82] have investigated the cantilevered piezoelectric energy harvesters. The L-shaped beam-mass structure was developed as a new piezoelectric energy harvester configuration. A linear distributed parameter model for predicting the electromechanically coupled voltage response and displacement response of the harvester structure was developed and investigated. The computational scheme of the proposed harvester is shown in Figure 1.22 where the m_{1-3} represents the masses of different beam segments, while L_{1-3} stands for the lengths. YI_{1-3} represents the Young's modulus and the moment of inertia for each beam. W_{1-3} indicates the displacement variables of the system, and x_{1-3} is the reference frames. The electromechanically coupled modelling approach is based on the experimentally validated coupled distributed parameter model proposed by Erturk (2008) and (2009) [83], [84].

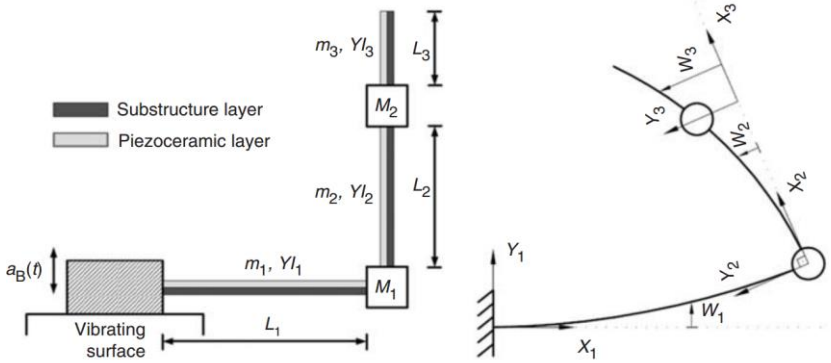

Figure 1.22. (a) Schematic of the L-shaped piezoelectric energy harvester, (b) the reference frames and the displacement variables [82]

Erturk (2014) [85] presented analytical electroelastic modelling of piezoceramic patch-based energy harvesters structurally integrated on thin plates. Analytical, distributed parameters and electrostatic model based on Kirchhoff's plate theory for energy harvesting from thin plates can be used for prediction of energy output of such device, predicting its dynamic parameters, etc. A similar electrostatic beam model was devised by Erturk and Inman (2009) [86]. Closed-form steady state solutions for electrical and structural responses were obtained for harmonic force excitation. Multi-mode and single-mode analytical frequency response functions (FRFs) between voltage output-to-force input and displacement-to force input were derived and generalized for different boundary conditions of thin plates as described in [86].

Closed-form steady-state solutions for the electrical output and structural response were derived for harmonic force inputs. There exists many different approaches for solving the numerical models but the favourite is the Finite Element Method (FEM). The description of the Finite Element matrix formulation can be found in [87]. Establishing nodal solution variables and element shape functions over an element domain, which approximate the solution, leads to finite element discretization. These models are usually implemented in commercially available software tools. Erturk (2009) [88] has developed a finite element model for piezoelectric energy harvester plates. An electromechanically coupled finite element (FE) plate model was presented for predicting the electrical power output of piezoelectric energy harvester plates. The presence of conductive electrodes were taken into account in the FE model. The derivation given in this paper was for both a unimorph and bimorph piezoelectric energy harvester configurations.

A rectangular finite element with three mechanical degrees of freedom per node (namely, the displacements u, v and w in x, y and z directions; θ represents the electromechanical coupling for the given direction) shown in Figure 1.23 is used to model the substructure and the piezoceramic layers as described by Erturk (2009) [88]. If we assume that the surfaces normal to bending direction are ideally covered with a perfectly conductive electrode, we can conclude that 1 DOF (namely, the voltage across these electrodes) is more than enough for modelling the electrical response. The rectangular element shown in Figure 1.23 has a total of 13 DOF.

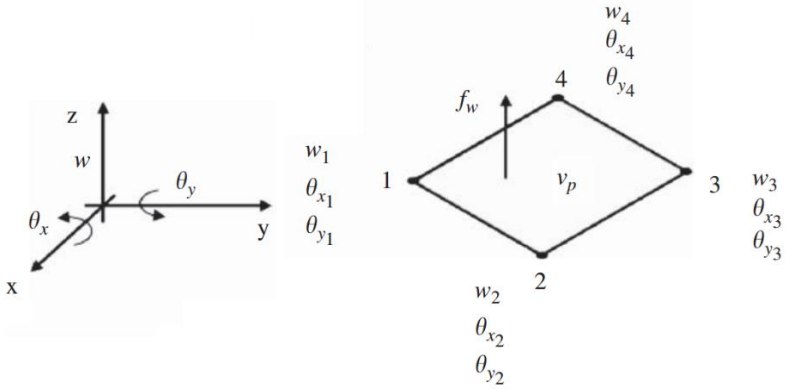

Figure 1.23. Piezoelectric finite element with 12 mechanical degrees of freedom and 1 electrical degree of freedom [88]

It was shown that the electromechanical FE model can successfully predict the analytical and the experimental results of the bimorph reported in the literature. Sheng (2013) [89] has modelled an impact driven piezoelectric energy harvester from human motion. The design of the harvester is a cantilevered beam sandwiched between two PZT – 5A layers with an attached proof mass at the free end. A schematic drawing of the proposed system is shown in Figure 1.24(a) and 1.24(b) where M is the mass, C is the damping coefficient, K is the stiffness, $i(t)$ and $v(t)$ are the current and voltage outputs and $F_P(t)$ is the time varying force applied. Finite element modelling was used for simulating the optimal resistance. The coupled piezoelectric-circuit finite element method was performed using the software ANSYS.

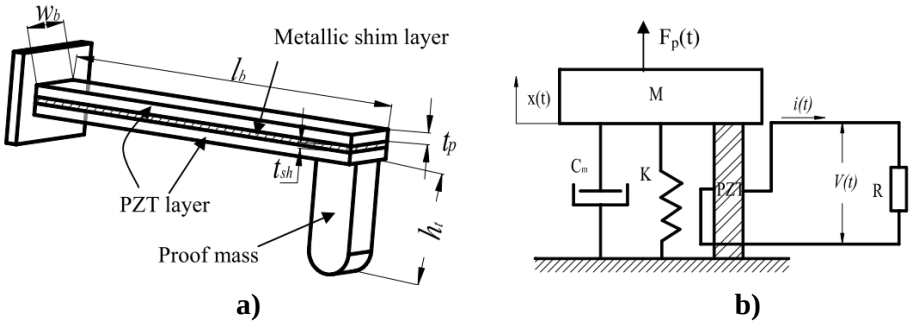

Figure 1.24. (a) A schematic diagram of piezoelectric bimorph. (b) General electromechanical model of piezoelectric vibration energy harvester. [89]

Using the harmonic analysis, the current, voltage, dissipated power over the electrical load and mechanical characteristics were obtained. The meshed FEM model of the piezoelectric cantilever beam with the asymmetric tip is schematically shown in Figure 1.25. The open circuit resonant frequency of this model is about 260 Hz in modal simulation.

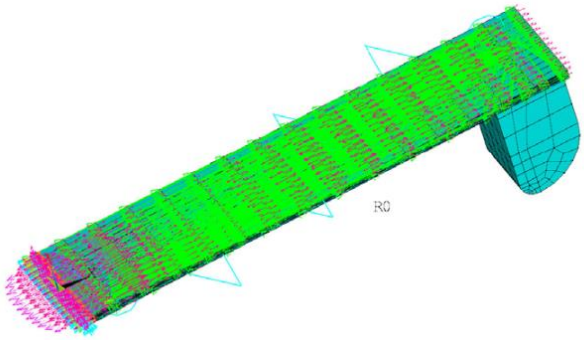

Figure 1.25. Meshed finite element model of piezoelectric cantilever beam with connecting external load resistor [89]

Harmonic analyses were performed with multiple external connecting resistances as well as the frequency response curves of output average voltage with various load resistors.

Two piezoelectric sheets are attached on the neutral plane to have opposite polarization directions in a serial connection while two sheets have the same polarization direction in a parallel connection. For the construction of the FE model, three different types of elements are used in ANSYS (see Figure 1.26). Figure 1.26 shows an example of the FE modelling for a bimorph with a parallel connection. A resistor is connected between the top electrode and the piezo-substrate interface (electrically grounded); and the top and the bottom electrodes are additionally connected using a wire with a very small resistance value.

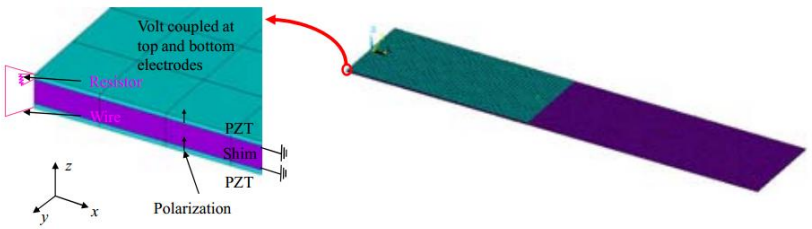

Figure 1.26. FE modelling of piezoelectric bimorph using ANSYS. [90]

Park (2012) [90] proposes a new design for a cantilever-type piezoelectric energy harvester in which a tip is excited by any rotary motion of mechanical devices. A coupled field finite element model for the harvester was constructed using ANSYS. A piezoelectric bimorph is a cantilever-type harvester composed of two piezoelectric layers. According to the polarization directions of the two piezoelectric sheets, the bimorph is categorized into serial connections and parallel connections.

Sunithamani (2013) [91] has developed a FE model to investigate the effect of substrate thickness on performance of energy harvester through simulation. To evaluate the energy harvesting performance of four structures, electrical, frequency and mechanical analysis was carried out. In this study, the thickness of the substrate varied for different structures, namely structure 1, structure 2, structure 3 and structure 4 to evaluate its performance using software COMSOL Multiphysics. Four different geometries are designed and modelled using the software COMSOL Multiphysics. In all structures, steel is used as a substrate; and single-crystal PMN is used as a piezoelectric material. Structure 1 has a rectangular shape cantilever with a rectangular cross section. Piezoelectric material is applied along the full length of the cantilever (RCRCpmnFL). Structure is a cantilever with rectangular shape and a trapezoidal cross section. Here, the piezoelectric material is applied along the full length of the cantilever (RCTRCpmnFL). A cantilever with an optimized piezoelectric layer length produces more output voltage [89]. Therefore, structure 3 and structure 4 are designed as structure 1 and structure 2 but with a reduced piezoelectric layer length.

Kumar (2014) [92] used the Finite Element Modelling to couple the mechanical and electrical domains in unimorph cantilever-type piezoelectric energy harvester. The linear piezoelectric theory and the first order shear deformation theory have been adopted. The model was coupled with a piezoelectric circuit consisting of a single electrical load for a better prediction of electrical damping and power output of the harvester. 24 mechanical and 1 electrical DOF were consider for each node, and

degenerated shell elements were used. Kumar (2014) [92] used the Genetic Algorithm (GA) to increase the energy density of PVEH with different piezoelectric materials. The aim function was to maximize the power density within the selected frequency range. The obtained cantilever shapes were then used in the developed numerical model. The structure under investigation was excited harmonically at low ambient vibration frequencies of 90-110 Hz. The developed model was used to investigate the performance of the PVEH with different piezoelectric materials attached. The results obtained from the finite element model show that the piezoelectric materials of KNN-LS-CT (2 wt.%) yield 35% higher mean power density than PZT material.

Rezaeealam (2011) [93] developed a numerical finite element model for the evaluation of performance of a unimorph vibration energy harvester based on magnetostrictive effect of the Galfenol rod. The Armstrong model is used in the 3-D FE model of the energy harvester. This approach is similar to piezoelectric transducers since it also utilises bending stresses. The COMSOL Multiphysics software was used to model static 3-D. The Armstrong model was chosen due to its ability to predict multiaxial magneto-elastic behaviour in magnetostrictive materials and because it is suitable to incorporate into FEM of the whole structure. The obtained numerical results were compared with the experimental results verifying the modelling results in a good agreement.

The mathematical optimization methods have been developed to solve a variety of different optimization problem formulations. General engineering optimization imposes constraints such as various design specifications and environmental restrictions. Optimization problems with constraints are called constrained optimization. Various numerical methods have been developed to solve the mathematical problem. Some popular methods are introduced in Table 1.4.

Table 1.4. Classification of numerical methods of constrained optimization [72]

Classification		Algorithm	Remarks
Direct method	Primal method	Sequential linear programming (SLP)	A solution of an approximated subproblem is obtained and the optimum solution is found in an iterative process
		Gradient projection method (GRP)	
		Feasible directions method (FDM)	
		Sequential or recursive quadratic method (SQP or RQP)	
	Transformation method	Sequential unconstrained minimization technique (SUMT)	A constrained problem is Transformed to an unconstrained problem and the solution is found in an iterative manner
		Penalty function method	
		Barrier function method	
		Augmented Lagrangian method	
Indirect method	Hybrid method	Optimality criteria method	The KKT conditions of the formulated problem are used to drive an iterative solution strategy

The indirect method tries to solve the Karush–Kuhn–Tucker necessary conditions. It has been verified to be numerically inefficient. The method is rarely used except for topology optimization methods, which have an extremely large number of design variables. The primal method is generally used in engineering optimization; and this chapter explains the basis of the most primal methods.

Optimization techniques have various adaptations, but the biggest interest is received where the trial-and-error method is too expensive or the calculations are too complicated to reach the desired results without mathematical optimization. One of such fields is the structural design. The geometrical or other parameters of the structure can be determined by evaluating the inputs (operating conditions), choosing the right input to output relation (parameterizing the structure), choosing the right state variables, selecting the right criterion function for evaluating performance of the structure during optimization and iterative modification of the system under research, all of the later described by Pister (1972) [73] in his extensive study.

Migliniene (2017) [94] have utilised mathematical optimization techniques to enhance the efficiency of PVEH operating in a vibro-impacting mode. The aim of the optimization problem was to maximize the vibration amplitudes of the cantilever vibrating in higher mode shapes with constraints to modal characteristics, namely the second resonant frequency of the structure. The gradient projection method (GPM) was used. The authors demonstrated significantly improved energy conversion efficiency which was achieved by enhancing the higher-mode responses even at highly variable excitation frequencies and amplitudes.

The same approach, namely vibro-impacting excitation was investigated by Ostasevicius (2015) [95]. In this case, the third vibration mode was used to extend the dynamic efficiency of the PVEH. The higher vibration modes in this case are pursued to increase the amount of deformations, and thus the amount of energy generated. The authors also demonstrated the time fold increase in generated open circuit voltage output when segmenting the piezoelectric material to avoid cancelation effects. The material was segmented at strain node points obtained from the modal analysis. The same as described by Migliniene (2017) [94] – the GPM method – mathematical optimization problem solving method was used to obtain the cantilevers of optimized shape. The aim function was to minimize the mass of the cantilever with restrictions for eigen frequencies, namely the third resonant frequency.

Modelling of the piezoelectric or any other energy harvesting device that exploits electromechanical energy conversion and works in resonant mode can be modelled by using an equivalent circuit or a finite element modelling.

1.9. Experimental verification techniques.

After the mathematical and numerical models are developed and solved, they have to be verified experimentally, recreating the conditions described in the models as precisely as possible. In this section, a review of different techniques, methods and equipments used by different researchers shall be reviewed. The experimental equipment usually consists of the signal generating equipment to mimic the environmental excitation frequencies and other dynamic properties, and signal detection/recording equipment to record the devices electrical and/or dynamic

response to that excitation. The first example provided by Sheng (2013) [89] used real excitation (human body walking) instead of artificial excitation signal generator. Sheng (2013) [89] has modelled an impact driven piezoelectric energy harvester from human motion and the obtained results were tested experimentally. The key components of the impact vibration harvester prototype include PZT bimorph, the cylinder with four ridges and the tip and the shaft as shown in Figure 1.27(a).

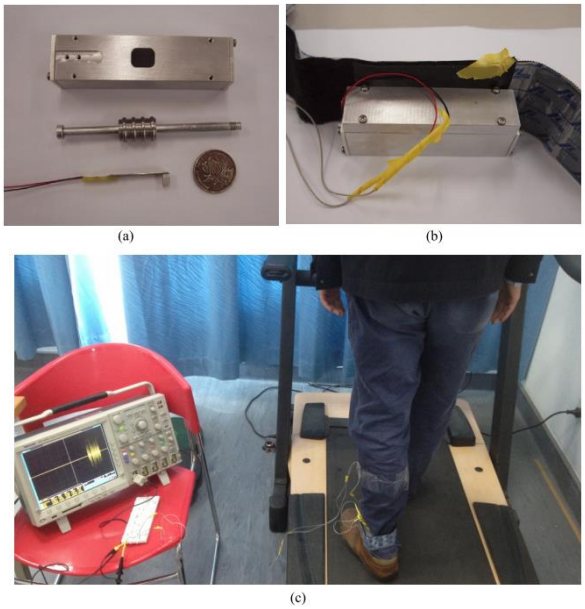

Figure 1.27. (a) Photograph of the actual prototype, showing the PZT bimorph, shaft, cylinder, cover and frame. (b) Assembled prototype

Since the PZT material is fragile and brittle, the large displacements of conventional low-frequency harvesters have commonly been restricted by additional mechanical stops. The experimental arrangement used to test the impact-driven energy harvester is shown in Figure 1.27(c). The dimensions of the prototype device were 90 x 32 x 24mm. The device is made of a cylinder sliding inside a metal shaft, with PZT bimorph beams inside the shaft. The device is mounted on a vibrating structure which in this case is a human body walking on a treadmill. Thus, a low frequency vibration was induced on the bimorph as the metal cylinder moved through the cylinder and hit the PZT bimorphs. The walking speed of the human was 5 km/h. The vibrations induced were frequency up converted, since the low frequency movement of the human body induced high frequency vibrations of the PZT bimorphs via impact coupling. An oscilloscope was used to measure the output voltage with varying electrical load conditions. As described by Sheng (2013) [89], due to the resonant frequency of the PZT bimorph with the tip being 260 Hz, we set up the sample rate of the oscilloscope to 2,5 $\mathrm{ks/s^{-1}}$ (nearly ten times as much as the resonant frequency) and adopted high-resolution sampling for more accurate measurements. The RMS voltage was measured of a 40 s sample. The duration was displayed on the oscilloscope screen with high resolution; and the corresponding output power was

calculated by the equation $P = V^2/R$. Open circuit voltage output and power outputs with different resistive loads were also measured. The peak of the measured power output was 51 μW. Multiple experiments were conducted. It was revealed that a stable power output and operation is also possible at higher walking speeds producing even higher power output, but an optimized electrical load is required for the maximization of power output. The theoretical results were confirmed.

Erturk (2014) [85] conducted experiments to verify the analytical electroelastic modelling of piezoceramic patch-based energy harvesters structurally integrated on thin plates. The experimental setup used is presented in Figure 1.28. The materials of the host plate were aluminium. It was fixed on all sides firmly with additional aluminium clamping bars with two lines of screws ensuring perfect fully fixed boundary conditions. The screws were tightened with a torque wrench to establish zero deflection and zero slope symmetrically along all four edges of the host plate. The whole plate with its setup can be seen in Figure 1.28(a). An off-the-shelf piezoceramic patch (T105-A4E-602 from Piezo Systems, Inc.) is attached on the host plate. The host structure with the aluminium plate attached was excited with a sine-sweep using an electromechanical shaker as shown in Figure 1.28. The surface transverse vibrations were recorded using a laser vibrometer Polytec PDV 100. Different scenarios were investigated, namely with open and short circuit electrical boundary conditions of the piezoelectric patch and some intermediate values of resistive load. The system response measured by force transducer was recorded using signal analyser shown in Figure 1.28. Moreover, the laser vibrometer and oscilloscope reading of voltage across resistive loads were recorded by the same signal analyser. By defining the force transducer's output as the reference channel in the signal analyser, the experimental FRFs including the velocity response-to-force input and voltage output-to-force input were obtained.

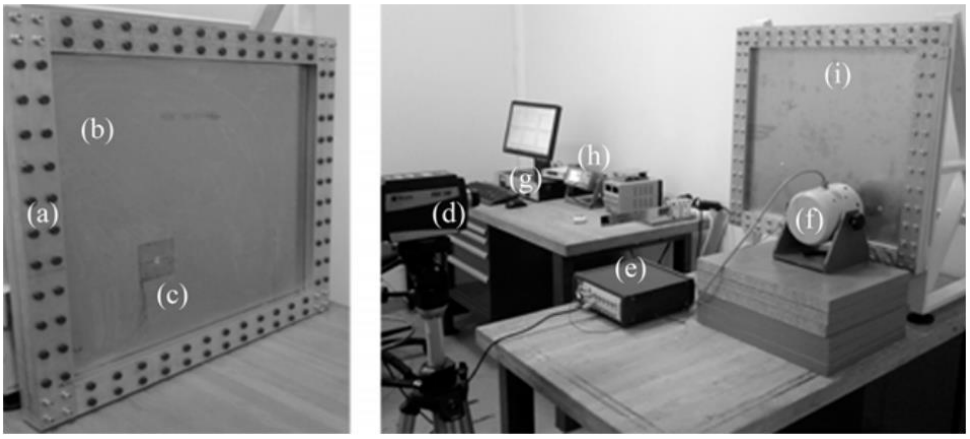

Figure 1.28. Erturk experimental setup. (a) aluminium plate clamping; (b) aluminium plate with piezoelectric material; (c) piezoelectric material; (d) laser vibrometer; (e) signal analyser; (f) electromechanical shaker; (g) amplifier; (h) signal generator; (i) aluminium plate without piezoceramic patch. Erturk (2014) [85]

The analytical FRFs are obtained between the displacement of the plate and the force input, whereas the velocity of the plate is measured using the laser vibrometer. In this work, the analytical velocity FRFs were obtained simply multiplying analytical displacement FRFs with $j\omega$. The mechanical damping ratios used in the analytical model were extracted from the experimental voltage FRF by applying the half-power point method at the resonance frequencies. The gathered data such as peak electrical outputs (voltage, current and power) versus load resistance values were investigated and used with numerical methods and programming tools to create experimental voltage FRFs with different resistive loads as shown in Figure 1.29. Experiments verified the developed models with good agreement.

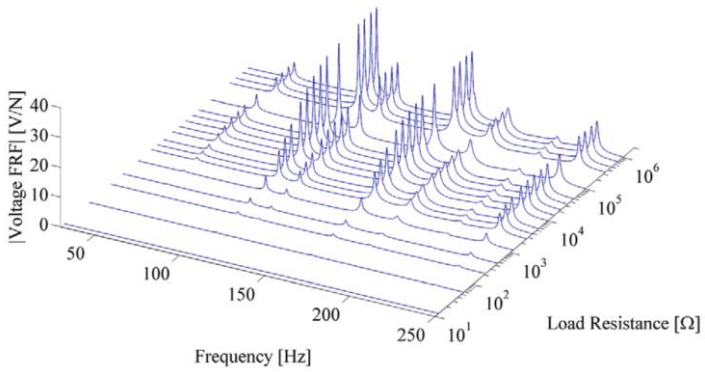

Figure 1.29. Experimental voltage FRFs for a set of resistive loads [85]

Another work was done by Sunithamani (2015) [96] who verified the derived FE model and mathematical optimization models experimentally. The piezoelectric energy harvester prototypes were fabricated. The dynamic waveform of the voltage from the harvester was analysed, and the performance was measured. The performance was compared among the four prototypes in terms of the design shape and the voltage waveform, and the charged voltages and powers. The charging performance was measured using a 10 μF capacitor, and the accumulated voltage was measured for one minute. We roll the mouse at a random velocity to excite each harvester, and the measurements were done 10 times for each harvester. Accumulated voltages and power outputs were measured and compared for different designs.

As for the displacement measurement, the laser vibrometry is recognized as the most suitable method employed by numerous authors, including Rezaeealam (2011) [93] and Migliniene (2017) [94]. The later used the Polytec scanning laser Doppler vibrometer to measure the frequency response of the piezoelectric cantilevered energy harvester (5 x 0,5 x 0,05 mm). Not only a single frequency measurement was taken but also random excitation frequency responses were measured. The harvester was mounted on electromagnetic shaker that in turn was connected to function waveform generator Agilent 33220A and amplified by the linear amplifier EPA-104 (Piezo Systems Inc., Woburn, MA, USA). The interference optical laser signal generated and registered by the Polytec OFV 512 fibre-optic interferometer was transformed into an electrical signal using a Polytec OFV 5000 vibrometer controller via an MSV-Z-40

Scanner controller and transmitted to a Polytec Vibroscan DAQ PC for the analysis as described by Miliniene (2017) [94]. The voltage output of piezoelectric segments was recorded by an oscilloscope PicoScope 3424 (PicoTechnology Ltd., St Neots, UK). The experimental setup can be seen in Figure 1.30. Multiple open circuit output voltage signals were recorded during the experiments since the harvesters under investigation had multiple piezoelectric segments attached.

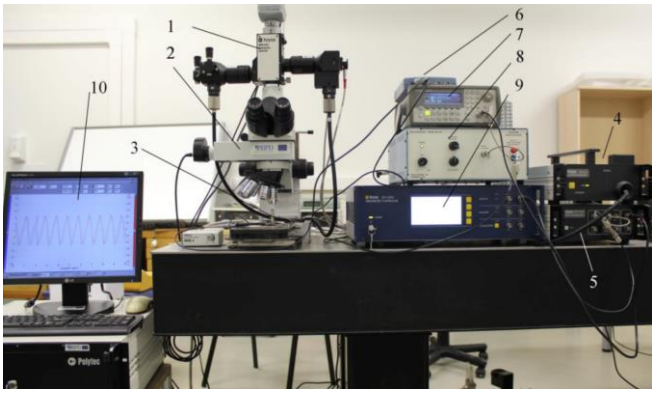

Figure 1.30. Experimental setup by [94]: 1 – laser positioning and scanning equipment, 2 – microscope, 3 – harvester, 4 – fibre-optic interferometer, 5 – scanner controller, 6 – oscilloscope, 7 – function waveform generator, 8 – amplifier, 9 – vibrometer controller, 10 – vibro-scanner

Rezaeealam (2011) [93] used a more modest laser displacement measurement system as shown in Figure 1.31. Here, the harvester is mounted on top of electromagnetic shaker with an accelerometer attached to measure the amplitudes of excitation. To measure the vibration amplitude of the tip of the harvester, a laser sensor was employed.

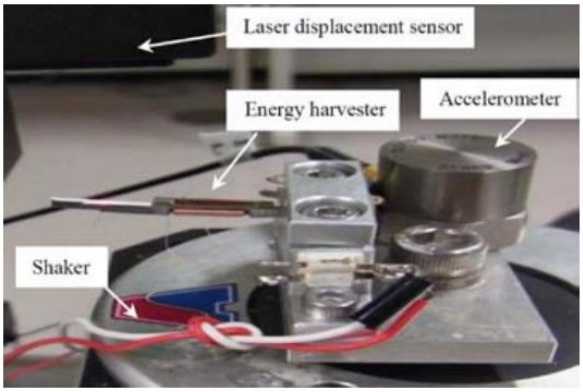

Figure 1.31. Experimental setup by [93]

1.10. Section Conclusions.

This section presented a review of recent publications as well as the main theoretical concepts and principles used in the field of energy harvesting. Firstly, different types of abundant energy that could be used for energy harvesting were

discussed as well as their applicability for MEMS systems. This was followed by a review of most common mechanical or more particularly vibration energy harvesting transduction mechanisms such as electromagnetic, electrostatic and piezoelectric. A focused analysis was done in different methods for increasing the bandwidth of piezoelectric and hybrid energy harvesters including mechanical and electrical resonant frequency tuning. It was decided that the highest potential is seen in the piezoelectric transduction mechanism that is operating in higher transverse vibration modes, since higher modes operate at higher frequencies, and thus carry more energy that can be harvested. The drawback of this is the fact that high operation frequencies are hard to find in an ambient environment. Thus, the decision was made to use the frequency up conversion principle to convert the low frequency vibrations of the ambient environment to high frequency vibrations in the piezoelectric energy harvester. Since higher vibration modes have multiple strain nodes which would normally cancel out the charge collected in a single electrode, an electrode segmentation technique has to be developed for optimal segmentation of such electrodes.

The following conclusions were drawn from the completed analysis:

1. It was decided to designate a piezoelectric vibration energy harvesting device for vibration energy harvesting from low frequency vibration energy sources, since low frequency vibration energy is abundant in industrious and everyday life applications.
2. For electromechanical conversion, piezoelectric transduction mechanism was chosen due to its simplicity and good energy densities. Ease of manufacturing of such devices also plays an important role the selection.
3. After the review of different resonant frequency tuning methods, it was decided to further investigate piezoelectric transducers operating at higher vibration modes and transducers utilizing frequency-up conversion for energy harvesting from low frequency energy sources.
4. Coupled finite element models were developed for the vibration energy harvester operating at higher vibrations modes and a finite element model for vibration energy harvesting tandem consisting of a Low Frequency Resonator (LFR) and a Piezoelectric Vibration Energy Harvester (PVEH) and operating in vibro-impacting mode for a better understanding of the dynamics of such devices. The FE models were coupled with electrical circuit, which enabled the prediction of power output for such devices.
5. FE model was chosen to be implemented in the COMSOL Multiphysics program with a coupled SPICE electrical circuit attached.
6. It was decided to develop mathematical algorithms for solving geometry optimization problems for piezoelectric energy harvesting devices.
7. Vibrometry and holographic measurement systems were chosen as the main stands to perform experimental studies and verify numerical simulation results.

2. MODELING OF AUTONOMOUS PIEZOELECTRIC ENERGY HARVESTING DEVICES.

The chapter presents the mathematical models used for modelling the object under the investigation for this thesis – the piezoelectric vibration energy harvester operating in higher transverse vibrations mode and frequency-up converting mode. Since the aim of this thesis is to analyse and develop different piezoelectric vibration energy harvester power output maximization techniques, taking advantage of higher vibration modes and ensuring their operation at varying mechanical excitation conditions, the reader is first briefly introduced to electromechanical coupling modelling. The piezoelectric consecutive equations are also described and analysed in this section. The Bernoulli beam theory is introduced, since it is the theory behind the bent beam, which is the basis of piezoelectric cantilevered energy harvester operation principle. Modelling of the dynamics of the piezoelectric harvester, including cross-coupling between the elastic variables and the dielectric variables was done. To estimate the power output of a piezoelectric or any other energy harvester, it is necessary to account for the size of the electrical load used. For this purpose, the CPC-FEM model is described. Since one of the methods to maximize the power output of the piezoelectric vibration energy harvester operating at low frequencies is the frequency-up-conversion, and this can be achieved by impact coupling, the Hunt and Crossley nonlinear contact model was described and implemented for mechanical contact modelling. Another technique for harvester power output maximization is mathematical optimization. The shape of the harvester can be optimized to maximize the amount of the normal strain with constraints to the parameters, like the geometric shape or the eigen frequencies. The mathematical optimization problem was formulated for solving the dynamic problem using equivalent static load technique. For the numerical analysis of the obtained results certain numerical analysis methods are necessary. For this purpose, a Discrete Fourier Analysis was investigated deeper. Mathematically, the DFT or discrete Fourier transform is a method to convert a finite sequence of equally spaced samples.

2.1. Electromechanical coupling.

For linear piezoelectric material, the equations describing the electromechanical conversions can be written as shown in (2.1, 2.2) and described by Erturk (2009) [82]. The equations link electrical displacement with piezoelectric strain constant and permittivity or strain vector with compliance and vector of applied electrical field. The equation (2.1) and (2.2) refer to a situation where the piezoelectric element is used as an actuator rather than sensor/generator.

$$\varepsilon_i = S_{ij}^{E}\sigma_j + d_{mi}E_m, \tag{2.1.}$$

$$D_m = d_{mi}\sigma_i + \zeta_{ik}^{\sigma}E_k\,; \tag{2.2.}$$

here, the indexes i, j =1, 2, …, 6 and m, k=1, 2, 3 refer to different directions within the material coordinate system. Since the object of this thesis is the vibration energy

harvester which operates in a generator mode equation, (2.1) and (2.2) are re-written as shown in equation (2.3) and (2.4).

$$\boldsymbol{\varepsilon}_i = \mathbf{S}_{ij}^{D}\boldsymbol{\sigma}_j + \mathbf{g}_{mi}\mathbf{D}_m, \tag{2.3.}$$

$$\mathbf{E}_i = \mathbf{g}_{mi}\boldsymbol{\sigma}_i + \beta_{ik}^{\sigma}\mathbf{D}_k\,; \tag{2.4.}$$

here, $\boldsymbol{\sigma}$ is a stress vector (N/m^2), $\boldsymbol{\varepsilon}$ – a strain vector (m/m), $\mathbf{E}$ – a vector of applied electric field (V/m), ξ – permittivity (F/m), $\mathbf{d}$ – matrix of piezoelectric strain constants (m/V), $\mathbf{S}$ – matrix of compliance coefficients (m^2/N), $\mathbf{D}$ – a vector of electric displacement (C/m^2) and $\mathbf{g}$ – matrix of piezoelectric constants (m^2/C), β – permittivity component (m/F). As described by Erturk (2009) [82], the superscripts *D*, *E* and σ represent the measurements taken at constant electric displacement, constant electric field and constant stress. In the matrix form, the equations (2.1-2.4) can be written as:

$$\begin{bmatrix}\varepsilon_1\\ \varepsilon_2\\ \varepsilon_3\\ \varepsilon_4\\ \varepsilon_5\\ \varepsilon_6\end{bmatrix} = \begin{bmatrix}S_{11} & S_{12} & S_{13} & S_{14} & S_{15} & S_{16}\\ S_{21} & S_{22} & S_{23} & S_{24} & S_{25} & S_{26}\\ S_{31} & S_{32} & S_{33} & S_{34} & S_{35} & S_{36}\\ S_{41} & S_{42} & S_{43} & S_{44} & S_{45} & S_{46}\\ S_{51} & S_{52} & S_{53} & S_{54} & S_{55} & S_{56}\\ S_{61} & S_{62} & S_{63} & S_{64} & S_{65} & S_{66}\end{bmatrix}\begin{bmatrix}\sigma_1\\ \sigma_2\\ \sigma_3\\ \sigma_4\\ \sigma_5\\ \sigma_6\end{bmatrix} + \begin{bmatrix}d_{11} & d_{21} & d_{31}\\ d_{12} & d_{22} & d_{32}\\ d_{13} & d_{23} & d_{33}\\ d_{14} & d_{24} & d_{34}\\ d_{15} & d_{25} & d_{35}\\ d_{16} & d_{26} & d_{36}\end{bmatrix}\begin{bmatrix}E_1\\ E_2\\ E_3\end{bmatrix}, \tag{2.5.}$$

and

$$\begin{bmatrix}D_1\\ D_2\\ D_3\end{bmatrix} = \begin{bmatrix}d_{11} & d_{12} & d_{13} & d_{14} & d_{15} & d_{16}\\ d_{21} & d_{22} & d_{23} & d_{24} & d_{25} & d_{26}\\ d_{31} & d_{32} & d_{33} & d_{34} & d_{35} & d_{36}\end{bmatrix}\begin{bmatrix}\sigma_1\\ \sigma_2\\ \sigma_3\\ \sigma_4\\ \sigma_5\\ \sigma_6\end{bmatrix} + \begin{bmatrix}e_{11}^{\sigma} & e_{12}^{\sigma} & e_{13}^{\sigma}\\ e_{21}^{\sigma} & e_{22}^{\sigma} & e_{23}^{\sigma}\\ e_{31}^{\sigma} & e_{32}^{\sigma} & e_{33}^{\sigma}\end{bmatrix}\begin{bmatrix}E_1\\ E_2\\ E_3\end{bmatrix}; \tag{2.6}$$

If the device is poled along the axis 3, and assuming the piezoelectric material used is a transversely isotropic material such as PZT or similar, many of the above parameters can be cancelled out or derived from other parameters. Non-zero compliance coefficients are found as shown in (2.7-2.11).

$$S_{11} = S_{22}, \tag{2.7.}$$

$$S_{13} = S_{31} = S_{23} = S_{32}, \tag{2.8.}$$

$$S_{12} = S_{21}, \tag{2.9.}$$

$$S_{44} = S_{55}, \tag{2.10}$$

$$S_{66} = 2(S_{22} - S_{12}); \tag{2.11}$$

As described in [29], the non-zero piezoelectric strain constants are $d_{31} = d_{32}$ and $d_{15} = d_{24}$. Finally, the non-zero dielectric coefficients are $e_{11}^{\sigma} = e_{22}^{\sigma}$ and e_{33}^{σ}. Subsequently, the equations (2.5) and (2.6) are simplified to:

$$\begin{bmatrix}\varepsilon_1\\ \varepsilon_2\\ \varepsilon_3\\ \varepsilon_4\\ \varepsilon_5\\ \varepsilon_6\end{bmatrix}=\begin{bmatrix}S_{11} & S_{12} & S_{13} & 0 & 0 & 0\\ S_{12} & S_{11} & S_{23} & 0 & 0 & 0\\ S_{13} & S_{32} & S_{33} & 0 & 0 & 0\\ 0 & 0 & 0 & S_{44} & 0 & 0\\ 0 & 0 & 0 & 0 & S_{44} & 0\\ 0 & 0 & 0 & 0 & 0 & 2(S_{11}-S_{12})\end{bmatrix}\begin{bmatrix}\sigma_1\\ \sigma_2\\ \sigma_3\\ \tau_{23}\\ \tau_{31}\\ \tau_{12}\end{bmatrix}+\begin{bmatrix}0 & 0 & d_{31}\\ 0 & 0 & d_{32}\\ 0 & 0 & d_{33}\\ 0 & d_{15} & 0\\ d_{15} & 0 & 0\\ 0 & 0 & 0\end{bmatrix}\begin{bmatrix}E_1\\ E_2\\ E_3\end{bmatrix}, \quad (2.12)$$

and

$$\begin{bmatrix}D_1\\ D_2\\ D_3\end{bmatrix}=\begin{bmatrix}0 & 0 & 0 & 0 & d_{15} & 0\\ 0 & 0 & 0 & d_{15} & 0 & 0\\ d_{31} & d_{31} & d_{33} & 0 & 0 & 0\end{bmatrix}\begin{bmatrix}\sigma_1\\ \sigma_2\\ \sigma_3\\ \sigma_4\\ \sigma_5\\ \sigma_6\end{bmatrix}+\begin{bmatrix}e_{11}^{\sigma} & 0 & 0\\ 0 & e_{11}^{\sigma} & 0\\ 0 & 0 & e_{33}^{\sigma}\end{bmatrix}\begin{bmatrix}E_1\\ E_2\\ E_3\end{bmatrix}; \quad (2.13)$$

The piezoelectric strain constant *d* can be defined as the ratio of the developed free strain to the applied electric field. The subscript d_{ij} refers to the electric field; the first subscript denotes the direction of polarization created in the material as the electrical field E is zero or, alternatively, is the strength of the applied field. The second subscript j denotes the direction of the applied stress or strain. The actuation matrix differs for the brittle PZT ceramic (2.3) and flexible PVDF piezoelectric foil (2.14). This is mainly because PVDF foil is a non-isotropic material and the applied electrical field in the direction of polarization will result in very different strains in 1 and 2 directions.

$$\begin{bmatrix}0 & 0 & d_{31}\\ 0 & 0 & d_{32}\\ 0 & 0 & d_{33}\\ 0 & d_{25} & 0\\ d_{15} & 0 & 0\\ 0 & 0 & 0\end{bmatrix}; \quad (2.14)$$

When we speak of piezoelectric material, the problem of strain or stress applied involves not only the elastic movement of particles inside the material but also the created electric and magnetic fields. This requires using both elastic equations of motion and Maxwell's partial differential equations to account for piezoelectric effect.

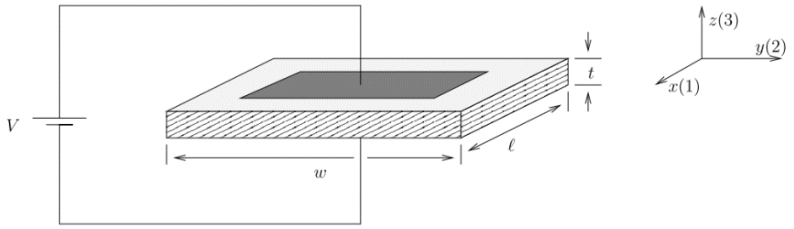

Figure 2.1. A piezoelectric transducer arrangement in d_{31} mode for energy generation;

In Figure 2.1, voltage V is applied to a piezoelectric transducer which is polarized in the direction 3. This voltage generates the electric field [29]

$$E_3 = \frac{\mathrm{V}}{t}, \tag{2.15}$$

which strains the transducer. In particular,

$$\varepsilon_1 = \frac{\Delta l}{l}, \tag{2.16}$$

in which

$$\Delta l = \frac{d_{31} V l}{t}, \tag{2.17}$$

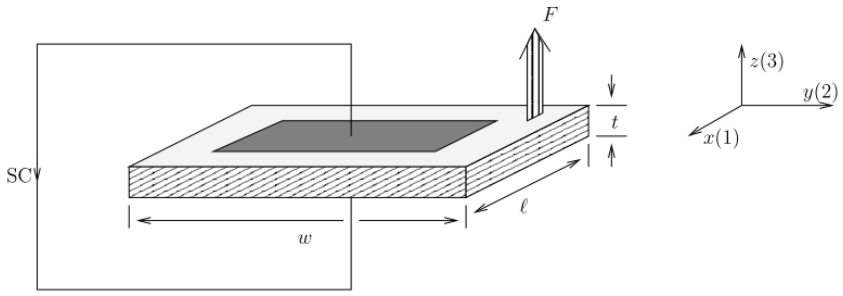

Figure 2.2. Charge deposition on a piezoelectric transducer - An equal, but opposite force, F, is not shown

Since positive electric field will usually generate positive strain in the direction 3, the piezoelectric constant d_{31} is usually a negative number. d_{ij} is also referred to as the ratio between the short circuit charge per unit area floating between the two electrode layers. Figure 2.2 illustrates that a force F applied in the direction 3 generates stress that is transferred through the short circuit. If we assume that the stress is supplied equally to the directions 1-3 and the electrodes in the planes 1-2, the short circuit charge per unit area and divided by applied stress is denoted by d_p. The charge in the direction 3 is found from (2.18)

$$\sigma_3 = \frac{F}{lw}, \tag{2.18}$$

which results in the electric charge

$$q = d_{33} F\,, \tag{2.19}$$

The piezoelectric constant g_{ij} refers to the electric field along the i-axis if it is stressed along j-axis. Therefore, in Figure 2.3, the applied force F results in the voltage (2.20)

$$V = \frac{g_{31} F}{w}, \tag{2.20}$$

Where d_{ij} is also referred to as the ratio between the short circuit charge per unit area floating between the two electrode layers. Figure 2.4 illustrates that the force *F* applied in the direction 3 generates the stress that is transferred through the short circuit. If we assume the that the stress is supplied equally to the directions 1-3 and the

electrodes in the planes 1-2, the short circuit charge per unit area and divided by applied stress is denoted by d_p. The charge in the direction 3 is found from (2.18).

Coefficient g_{ij} is also referred to as the ratio between the strain developed along the j-axis to the charge per unit area induced on the electrodes parallel to the planes 1-2. As shown in Figure 2.5, the electric charge Q induced to the electrodes the piezoelectric elements thickness will decrease by the amount calculable from (2.21).

$$\Delta l = \frac{g_{31} Q}{w}, \tag{2.21}$$

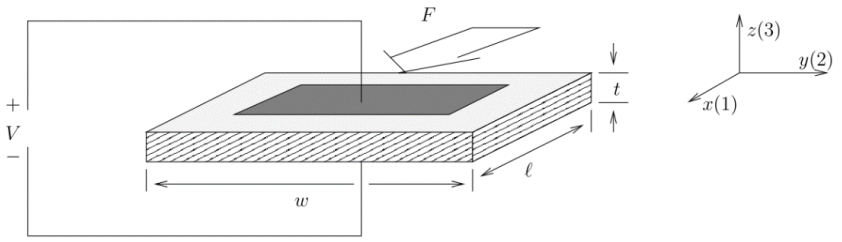

Figure 2.4. An open-circuited piezoelectric transducer under a force in direction 1 - An equal, but opposite force, F is not shown

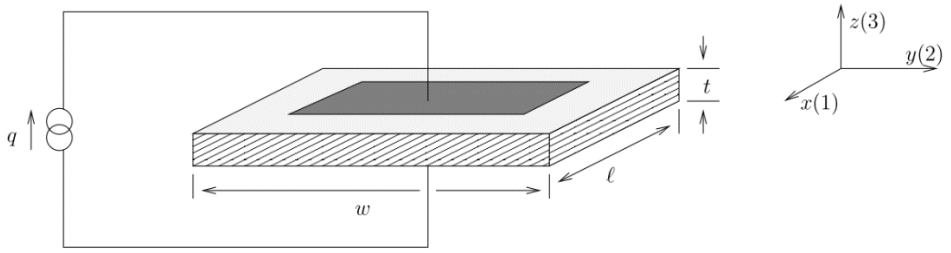

Figure 2.5. A piezoelectric transducer subject to applied charge

The elastic compliance constant S_{ij} is the strain in the i direction to stress in j direction ratio. It represents the tolerance of the materials to elastic deformations. The higher the compliance constant, the easier to stress or strain the material. For shear forces, the subscripts are 4-6 and strains and stresses are denoted as 1-3. If the compliance constant is measured with short-circuit electrode conditions, a superscript "E" is used, and the superscript "D" – for open-circuit conditions. As described in [29], the dielectric coefficient e_{ij} is the charge per unit area in the i-axis due to an electric field applied in the j-axis. The superscript σ in e_{11}^{σ} refers to the permitivity for a field applied in the 1 direction when the material is not restrained.

The piezoelectric coefficient k_{ij} is one of the most important coefficients, since it represents the ability of the piezoelectric material to transform the mechanical energy into electrical and vice versa. It basically represents the electromechanical conversion efficiency. The i index indicates if stress or strain is acting on the direction j and the electrode direction as well as power output is always perpendicular to the i-

direction. Evaluating the k_{ij} coefficient in piezoelectric material can be done in several ways, for example, for the actuator, it can be done by leaving the electrodes open-circuited and applying force onto the element. The element shall deflect, the magnitude of deflection Δz can be measured directly, and using the formula (2.22), the mechanical work done can be calculated.

$$W_M = \frac{F\Delta_z}{2}; \tag{2.22}$$

Subsequently, due to direct piezoelectric effect, the charges will be generated in the piezoelectric material. Thus, the amount of electrical energy can be calculated using formula (2.23)

$$W_E = \frac{Q^2}{2C_p}; \tag{2.23}$$

which is stored in the piezoelectric capacitor.

$$k_{33} = \sqrt{\frac{W_E}{W_M}} = \frac{Q}{\sqrt{F\Delta_z C_p}}; \tag{2.24}$$

The coupling coefficient can be written in terms of other piezoelectric constants. In particular, k_2.

$$k_{ij}^2 = \frac{d_{ij}^2}{S_{ij}^E e_{ij}^\sigma} = g_{ij} d_{ij} E_p; \tag{2.25}$$

Here, E_p is the Young's modulus of the piezoelectric material. The stiffness of the transducer varies depending on whether it is operated in short-circuit or open-circuit conditions, with the latter making the material less stiff. This is the result of the charges accumulated on electrodes not being collected, since during the oscillation, the positive and negative charges are accumulated on the surface, and thus cancelling each other out. Short and open circuit stiffness are denoted by coefficients K_{sc} and K_{oc} respectively (2.26):

$$\frac{K_{oc}}{K_{sc}} = \frac{1}{1-k^2}; \tag{2.26}$$

As shown in the constitutive (2.1), there are only three independent elements within the piezoelectric coupling tensor d. These are d_{33} and d_{31} and d_{15}, since the latter is only related to shear stress, which is not usable in energy harvesting; and d_{33} is rarely used for energy harvesting from transverse direction vibration energy harvesting applications. Only d_{31} is considered and described here. Figure 2.6 shows the d_{31} mode. The i in d_{ij} denotes the axis along which the voltage is generated, i.e., along the z-axis. The second dumber indicates the direction of stress application. In Figure 2.6, the stress T is applied in the direction 1 as the structure to which the active element is attached vibrates in the vertical (3) direction.

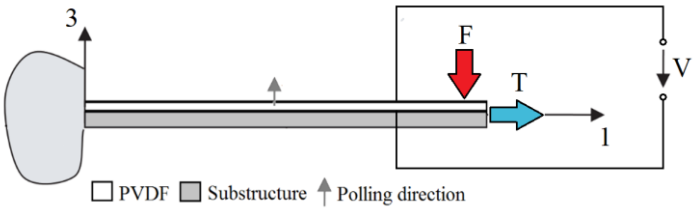

Figure 2.6. Piezoelectric material operated in d_{31} mode

For d_{31} modes, the constitutive (2.3) and (2.4) can be simplified to:

$$\begin{cases} S_1 = S_{11}^E \cdot \sigma_1 + d_{31} \cdot E_3 \\ D_3 = d_{31} \cdot \sigma_1 + \varepsilon_{33}^T \cdot E_3 \end{cases}, \tag{2.27}$$

All the above-mentioned equations define the electromechanical conversion of the piezoelectric vibration energy harvester operating in d_{31} mode.

2.2. Bernoulli beam theory.

Since a simple cantilevered energy harvester is considered in this thesis, its deformations are best described by the Bernoulli beam theory. Consider dynamic equilibrium of a beam element of length *dx* as shown in Figure 2.7.

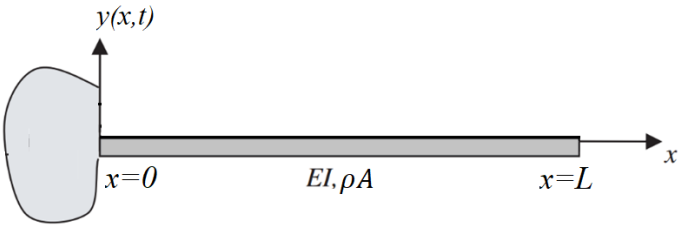

Figure 2.7. Computational scheme of a simple active element

By using Newton's law, some additional assumptions concerning the acceleration of this typical beam element are made.

- The motion is purely translational in the y-direction,
- Beam elements remain rectangular during the motion.

With these assumptions, setting the vertical forces of the element equal to mass times acceleration gives:

$$\frac{\partial \mathrm{V}}{\partial \mathrm{x}} = -\mathrm{w} + \rho \mathrm{A} \frac{\partial^2 \mathrm{y}}{\partial \mathrm{t}^2}; \tag{2.28}$$

while assuming moments produce:

$$\frac{\partial M}{\partial x} = V; \tag{2.29}$$

where ρ is the mass density of the material, A is the cross-section area and $y = y(x,t)$ is the transverse motion measure as shown in figure 2.7. Combining (2.28) and (2.29) yields:

$$\frac{\partial^2 M}{\partial x^2} = -w + \rho A \frac{\partial^2 y}{\partial t^2}; \tag{2.30}$$

From the geometry of the deformation and using Hook's law $\sigma_x = E\varepsilon_x$, assumption e), one can show that:

$$\frac{\partial^2 y}{\partial x^2} = -\frac{M}{EI}; \tag{2.31}$$

where E is the modulus of elasticity and I is the area moments of inertia of the cross-sectional about neutral axis-z. Finally, putting (2.30) and (2.31) together gives the desired result:

$$EI\frac{\partial^4 M}{\partial x^4} = \rho A \frac{\partial^2 y}{\partial t^2}; \tag{2.32}$$

which is the Euler Bernoulli beam theory equation. For the case of no external loading, $w = 0$, and so (2.32) it becomes:

$$b^2 \frac{\partial^4 M}{\partial x^4} + \frac{\partial^2 y}{\partial t^2} = 0; \tag{2.33}$$

where $b^2 = EI/\rho A$. To properly formulate a boundary value problem, we also need boundary conditions for this problem type. These conditions at the ends of the beam follow the undergraduate strength of materials, and a simply supported end, the deflection moment is zero; hence:

$$y = 0, \tag{2.34}$$

$$\frac{\partial^2 y}{\partial x^2} = 0; \tag{2.35}$$

For a built in or a fixed end, the deflection and slope are zero.

$$y = 0, \tag{2.36}$$

$$\frac{\partial y}{\partial x} = 0; \tag{2.37}$$

The case of a free end dictates that the moment of shear force is zero:

$$\frac{\partial^2 y}{\partial x^2} = 0, \tag{2.38}$$

$$\frac{\partial^3 y}{\partial x^3} = 0; \tag{2.39}$$

2.3. Piezoelectric harvester dynamics modelling and simulation.

For energy harvesting, the piezoelectric element must operate in the generator mode, utilizing the direct piezoelectric effect. To achieve the polarization of the poled anisotropic material, a mechanical load must be applied. Subsequently, an electrical

charge is generated in the piezoelectric material. This charge can be collected via the electrodes covering the surface of the piezoelectric material as shown in Figure 2.6. The density of the induced charge is linearly proportional to the strain in the material, and thus proportional to the externally applied stress. This relationship can be described mathematically as follows:

$$\mathbf{P_{pe}} = d \times T; \tag{2.40}$$

where $\mathbf{P_{pe}}$ is the piezoelectric polarization vector with a magnitude equal to the fixed charge density obtained due to the direct piezoelectric effect. Here, d is the piezoelectric strain, and the coefficient T is the stress affecting the piezoelectric material. In the equation (2.40), the subscript "pe" refers to value obtained directly from piezoelectric effect. Considering the elastic properties of the material, the equation (2.40) can be rewritten to (2.41).

$$\mathbf{P_{pe}} = \mathrm{d} \times \mathrm{T} = \mathrm{d} \times \mathrm{p} \times \mathrm{S} = \mathrm{e} \times \mathrm{S}; \tag{2.41}$$

where, p, e and S are the elastic constant, piezoelectric stress constant and mechanical strain. Elastic constant couples the generated stress and the applied strain. As the piezoelectric effect manifests, the stiffness of the material is always increased, which is related to the change in the dielectric constant. Piezoelectricity is the link that couples the elastic variables (stress T and strain S) with the dielectric variables (elastic charge density D and electric field E). The main consecutive equations for piezoelectric effect are written in the equations (2.42) and (2.43).

$$S_p = s_{pq}^{E} T_q + d_{pk} E_k, \tag{2.42}$$

$$\mathrm{D_i} = \mathrm{d_{iq}T_q} + \varepsilon_{\mathrm{ik}}^{\mathrm{T}}\mathrm{E_k}; \tag{2.43}$$

The s_{pq}^{E} , here, is the tensor of elastic compliance at constant value of electrical field upon the piezoelectric material, ε_{ik}^{T} is the dielectric constant tensor under constant stress, d_{pk} is the piezoelectric constant tensor, S_p is the mechanical strain in the p direction, D_i is the electric displacement in the i direction, T_q is the mechanical stress in the q direction, and E_k is the electric field in the k direction. Differential equations (2.44) and (2.45) can be written to express piezoelectric equations for the finite element method.

$$\mathbf{M\ddot{z} + C_{zz}\dot{z} + K_{zz}z + K_{z\Phi}\Phi = F}, \tag{2.44}$$

$$\mathbf{K_{z\Phi}^{t}z + K_{\Phi\Phi}\Phi = Q}; \tag{2.45}$$

Here, $\ddot{\mathbf{z}}$ is a acceleration vector of nodal point, $\dot{\mathbf{z}}$ is a nodal point velocity, and $\mathbf{z}$ is a nodal point displacement vectors respectively; Φ is the electrostatic potential and is a scalar, the subscript z refers to mechanical quantities, whereas the subscript Φ refers to electrical ones, and the combination of the two refers to electromechanical coupling matrices; **M**, **C** and **K** are global matrices and **z**, **F**, **Φ** and Q denote vectors. Equations (2.44) and (2.45) could be expressed in the matrix form:

$$\begin{bmatrix} \mathbf{M_{zz}} & 0 \\ 0 & 0 \end{bmatrix} \begin{pmatrix} \ddot{\mathbf{z}} \\ \ddot{\mathbf{\Phi}} \end{pmatrix} + \begin{bmatrix} \mathbf{C_{zz}} & \mathbf{C_{z\Phi}^t} \\ \mathbf{C_{z\Phi}} & \mathbf{C_{\Phi\Phi}} \end{bmatrix} \begin{pmatrix} \dot{\mathbf{z}} \\ \dot{\mathbf{\Phi}} \end{pmatrix} + \begin{bmatrix} \mathbf{K_{zz}} & \mathbf{K_{z\Phi}^t} \\ \mathbf{K_{z\Phi}} & \mathbf{K_{\Phi\Phi}} \end{bmatrix} \begin{pmatrix} \mathbf{z} \\ \mathbf{\Phi} \end{pmatrix} = \begin{pmatrix} \mathbf{F} \\ \mathbf{Q} \end{pmatrix}; \quad (2.46)$$

The constitutive equation for the load bearing material of the energy harvester under linear elasticity assumption (as shown in Figure 2.6) is written in the equation (2.47):

$$\mathrm{T} = \mathrm{C^H S}; \quad (2.47)$$

here, T is mechanical stress, $\mathrm{C^H}$ is the elasticity matrix and superscript H represents the load bearing material. S is strain Boundary conditions for an active element with one fixed end are as follows: One end of the active element is fixed while the other one remains free. This is mathematically described in equations (2.48) and (2.49) for fixed and free ends of the active element, respectively. Here, Y(x) is displacement in the y direction at the distance x from the fixed end.

$$\mathrm{x} = 0, \ \mathrm{Y(x)} = 0, \ \frac{\mathrm{dY(x)}}{\mathrm{dx}} = 0, \quad (2.48)$$

$$\mathrm{x} = \mathrm{L}, \ \frac{\mathrm{d^2Y(x)}}{\mathrm{dx^2}} = 0, \ \frac{\mathrm{d^3Y(x)}}{\mathrm{dx^3}} = 0; \quad (2.49)$$

The mechanical and electrical domains in piezoelectric material are coupled using the equations (2.50-2.51)

$$T = \mathbf{C^P} \mathrm{S} - \mathbf{e}\mathbf{E}\, \mathrm{S}, \quad (2.50)$$

$$D = \mathbf{e^T} \mathrm{S} + \boldsymbol{\varepsilon^S} \mathbf{E}\, \mathrm{S}; \quad (2.51)$$

where $\mathbf{C^P}$ is the elasticity matrix and the superscript P represents the piezoelectric material, D denotes the electric displacement, **e** and **E** are the piezoelectricity matrix and the applied electric field, respectively, and $\boldsymbol{\varepsilon^S}$ is the permittivity matrix. The electrical potential decreases linearly through the thickness of the piezoelectric material layer if the material is deformed by applying axial stress $\mathrm{T_1}$. As the result, charge is accumulated at the electrodes. Under open circuit boundary conditions (D = 0), the voltage across the piezoelectric material can be calculated as shown in equation (2.52)

$$\mathrm{V} = \mathrm{g_{31} h T_1}; \quad (2.52)$$

For modal analysis of the active element that is considered undamped and undergoing free vibrations, the governing equation is following.

$$\mathbf{M\ddot{u}} + \mathbf{Ku} = 0; \quad (2.53)$$

Internal elastic forces **Ku** are equal in size and opposite to internal forces **Mü**, where **K** and **M** are stiffness and mass matrixes, respectively. Eigen frequencies are obtained from the classical equation (2.54).

$$\mathrm{K}v = \omega_i^2 \mathrm{M}v; \quad (2.54)$$

The transient analysis of the active element can be conducted to verify the position of the strain node in the active element during its base excitation with time varying force f(*t*) acting on it. The equation of motion is then written as shown in (2.55).

$$\mathbf{M\ddot{u}}(t) + \mathbf{C\dot{u}}(t) + \mathbf{Ku}(t) = \mathrm{f}(t); \quad (2.55)$$

here, **C** is the damping matrix. The time-dependent force f(*t*) is described as an active element body load in the vertical direction and is defined as the force/volume using the thickness:

$$\mathrm{f}(t) = am \sin \omega_n t\,; \quad (2.56)$$

here, a is acceleration, m is the mass of the system and ω_n is the ambient excitation frequency.

2.4. Coupled piezoelectric-circuit model and transfer function.

CPC-FEM (coupled piezoelectric circuit FEM) is a model at which the piezoelectric transducer is directly coupled with the external circuit for electrical parameters evaluation, such as generated power, voltage, current, etc. allowing to estimate the size of optimal resistive loads and optimal dynamic parameters. Inertia based mechanical/vibration and, namely, the kinetic energy harvester can all be modelled as second-order spring mass damper systems. Some of the first attempts to model such a system was made by William and Yates (1996) [99]. The main parts of the resonator are represented by simple spring-mass system elements such as mass *m* suspended on a spring with the stiffness k_S, generating a resonant spring-mass system. Ambient excitation, in the perfect case sinusoidal, is represented by sinusoidal excitation that forces the mass to move harmonically as shown in (2.57)

$$\mathrm{y}(t) = \hat{\mathrm{y}} \sin(\omega t); \quad (2.57)$$

where $\hat{\mathrm{y}}$ is the amplitude of the movement of the structure to which the harvester is mounted, and ω denotes the angular vibration frequency. The relative movement between the host structure and the harvester is calculated from (2.58).

$$\mathrm{z}(t) = \hat{\mathrm{z}} \sin(\omega t + \varphi); \quad (2.58)$$

The mass vibration amplitude is denoted by $\hat{\mathrm{z}}$, and since there is a phase-difference between $\mathrm{y}(t)$ and $z(t)$, it is denoted by φ. Mechanical damping is represented by d. For the electromechanical conversion of the kinetic energy, numerous energy conversion mechanisms exist: capacitive, inductive and piezoelectric, which are employed by electrostatic, electromagnetic and piezoelectric transducers, respectively. The electricity generated by these transduction mechanism is, simply put, the work which is done by the mass of the harvester against the spring element – restoring force $\mathrm{F_e}$. This restoring force and electrical damping $\mathrm{d_e}$ is created by coupling between the mechanical and electrical domains of the material if the material is connected into the circuit as described by Hehn (2014) [98].

Since the harvester is never a stand-alone device and is usually used to power up a battery or an energy consuming device directly, it is essential to precisely estimate the power output, vibration amplitude and other dynamic parameters of the harvester for the given dynamic conditions. The key to this is the availability of a proper model that can be used to calculate the power output for designs. Governing equations for a piezoelectric vibration energy harvester can be written as shown in (2.59).

$$M\ddot{z}(t) + C\dot{z}(t) + Kz(t) = M\ddot{y}(t) - \Theta V_p, \tag{2.59}$$

$$\Theta z(t) - C_p V_p(\mathrm{t}) = Q_p(t); \tag{2.60}$$

where M is the mass, C is mechanical damping and K is mechanical stiffness. The electromechanical coupling coefficient of the piezoelectric material or, simply put, the efficiency at which the mechanical work is converted into electricity is denoted by Θ, and the electric capacitance of the piezoelectric material is denoted by C_p. The voltage generated across the electrodes is represented by V_p and Q_p. It represents the electrical charge accumulated on the electrodes. The relative movement between the host structure and the tip of active element is denoted by z(t). The acceleration applied by the host structure to the tip of the active element is represented by ÿ(t).

Electrical circuits can be attached to PVEH model for a more realistic estimation of the performance of a device under different dynamic conditions. However, it was proven that the electrical circuit attached has a significant impact on the vibration response of the harvester, which is directly related to the harvested power. Equations (2.61) and (2.62) allow to estimate the electrical outputs of the harvester with a resistive load attached:

$$V_R(t) = I_R(t)R, \tag{2.61}$$

$$P_R = V_R I_R; \tag{2.62}$$

here, the subscript R represents the resistive load. Thus, the voltage, the current and the power across the resistive load are denoted by V_R, I_R and P_R. In cases when the resistive load is directly connected to the piezoelectric material, the relation between the electrical output of the piezoelectric material and input to resistive load can be written as shown in equations (2.63) and (2.64).

$$V_P(t) = V_R(t), \tag{2.63}$$

$$I_R(t) = \omega Q_P(t); \tag{2.64}$$

A simple electrical circuit can be a useful tool for predicting the electrical outputs of the energy harvester and estimating the circuits impact on vibration response. For this purpose, a piezoelectric-circuit finite element model (CPC-FEM) is the simplest solution.

2.5. Dynamic contact modelling.

For a frequency-up converter with a mechanical coupling, it is essential to select a reliable contact model. The nonlinear viscoelastic contact model presented by Hunt and Crossley for direct, frictionless contact of low surface area is used for the dynamic contact modelling as shown in Figure 2.8 where *i* is the ith contact point of PVEH, and *j* is jth contact point of LFR. The general case of the model is described by Machado (2012) [100] Since the object of investigation is the frequency-up converter, the contact is between a low frequency resonator (LFR) and a high frequency piezoelectric energy harvester (PVEH) as shown in Figure 2.8(a).

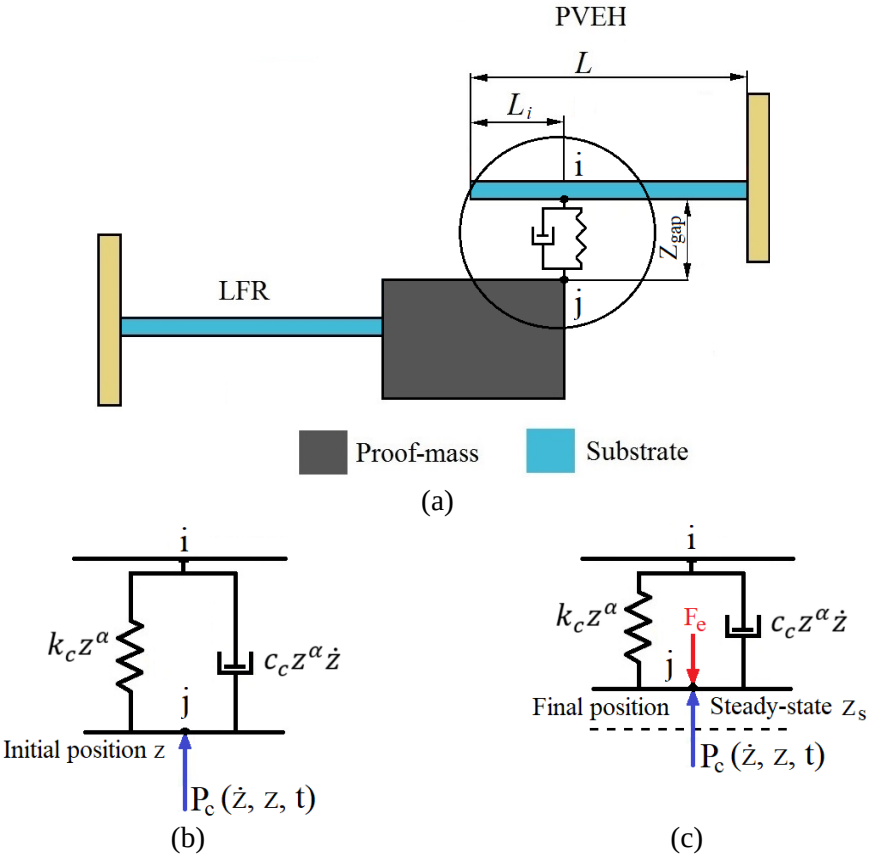

Figure 2.8. LRF and PVEH contact model (a) computational scheme; Nonlinear elastic dynamic Hunt – Crossley contact model: (b) initial position, (c) final position;

The dynamic contact between LFR and PVEH is expressed by the spring constant k_c and damping factor c_c. The gap between two bodies is given by z_{gap}, while the gap ($z_{gap} > 0$) spring and damping constants of the contact have no effect, as shown in Figure 2.8(b). The external mechanical excitation on the bodies is described by the external mechanical load vector **F** and can be expressed as (2.65).

$$(\mathbf{F}) = \begin{cases} (\mathbf{F_k}), \; p_{ls}(\dot{z}_{ls}, z_{ls}, t) \geq 0, \\ (\mathbf{F_k}) + (\mathbf{P}_c(\dot{z}, z, t)), p_{ls}(\dot{z}_{ls}, z_{ls}, t) < 0; \end{cases} \tag{2.65}$$

Here, (F_k) is the kinematic excitation force, $(\mathbf{P_c}(\dot{z}, z, t))$ is a nonlinear interaction vector in the contact pair, and p_{ls} is the contact pair nonlinear interaction force at the contact point of the PVEH. During the contact, LRF and PVEH systems function in parallel to each, and the contact force is expressed as shown in Figure 2.8(c) and as described by equation (2.66):

$$\mathbf{P_C} = k_c z^\alpha + c_c z^\alpha \dot{z}, \; for \; z < 0 \;\; \text{and} \;\; \dot{z} < 0; \tag{2.66}$$

where k_c is a contact stiffness coefficient, c_c is a contact damping coefficient, and α is a force exponent depending on contact surface geometry (α = 2 is assumed). This system of equations could be solved by direct numerical integration methods.

2.6. Shape optimization of the active element of power harvester.

As stated by Park (2007) [72], in optimization, optimum values of the variables are found to minimize or maximize the function that is expressed by the variables. Optimization is a field of study focusing on numerical solution of a mathematical design problem formulated as follows:

Find

$$b \in R^n, \tag{2.67}$$

to optimize

$$f(b), \tag{2.68}$$

subject to

$$h_i(b) = 0,\ i = 1, \dots, l, \tag{2.69}$$

$$g_j(b) \leq 0,\ j = 1, \dots, m, \tag{2.70}$$

$$b_L \leq b \leq b_U; \tag{2.71}$$

here, as described by Park (2007) [72], b is the design variable vector with n elements, f is the objective function, h_i is the ith equality constraint, g_j is the j[th] inequality constraint, $\boldsymbol{b_L}$ and $\boldsymbol{b_U}$ limit conditions for *b*, respectively, *l* is the number of equality constraints and *n* is the number of inequality constraints. The main goal of optimization procedure is to find an optimum value, i.e., to maximize or to minimize a specific design parameter, depending on the problem. The parameter targeted for improvement is called the objective function and is written as shown in (2.68), with limit conditions as written in (2.63-2.71).

Design optimization is generally used in detailed design, since it determines the detailed values of the design variables. The process of the conceptual design is not usually expressed in (2.67-2.71), since the engineering design of the structure is finished. Thus, the optimization of the structure is always done after the engineering design is conclude. Specific programming tools such as MATLAB are used further to employ an algorithm to solve the equations (2.67) to (2.71). Optimization is only applicable when a design problem can be mathematically formulated as in (2.67) to (2.71). It is especially useful in the detailed design.

Structural optimization

As described by Park (2007) [72], in structural optimization, the governing equation is computationally solved, and the solution is used for the evaluation of the objective function and constraints. The governing equation is considered as the equality constraints in (2.69). Structural optimization is formulated as follows:
Find

$$\mathbf{b} \in \mathbf{R^n}, \tag{2.72}$$

to optimize

$$\mathbf{f}(\mathbf{b}, \mathbf{z}), \tag{2.73}$$

subject to

$$\mathbf{K}(\mathbf{b})\mathbf{z} = \mathbf{f}, \tag{2.74}$$

$$\mathbf{g_j}(\mathbf{b}, \mathbf{z}) \leq 0, \qquad j = 1, \dots, m, \tag{2.75}$$

$$\mathbf{b_L} \leq \mathbf{b} \leq \mathbf{b_U}; \tag{2.76}$$

The objective function in (2.71) can be the weight of the structure or a specific response. The inequality constraints in (2.73) are generally defined by limit values on displacements, stresses, natural frequencies, etc. In the optimization process, we need sensitivity information for the function in (2.72-2.76) with respect to design variables. It is known that the sensitivity evaluation is quite expensive. Therefore, an efficient calculation of sensitivity information is significant.

Structural optimization under dynamic loads

In the case of the linear static problem, the governing equation for FEM can be formulated as written in (2.77).

$$\mathbf{K}(b)\mathbf{z} = \mathbf{f}, \tag{2.77}$$

here, **K** is the stiffness matrix, **z** is the nodal displacement vector, **b** is the design variable vector for sizes and shapes, and **f** is the external load vector as described by Park (2007) [72]. As the name implies, dynamic loads imply a time varying force to the structure resulting in a time varying response. As a result, a time varying response should be integrated into the equations of optimization to account for the dynamics. In the "real world", all the loads are dynamic but most of them can be reduced to problems with static loads. The problems that cannot be reduced to static problems are solved using dynamic response optimization. However, static loads are generally preferred because dynamic response optimization is time and calculation consuming. Park (2007) [72] described the dynamic response optimization extensively. If $\mathbf{f}(t)$ is an external load vector and *t* is time, the governing equation in the FEM formulation is as written in (2.78).

$$\mathbf{M}(\mathbf{b})\ddot{\mathbf{z}} + \mathbf{K}(\mathbf{b})\mathbf{z} = \mathbf{f}(t); \tag{2.78}$$

Here, **M** is the mass matrix and $\ddot{\mathbf{z}}$ is the acceleration vector. (2.79) to (2.83) are the general formulations for dynamic response optimization.
Find

$$\mathbf{b} \in \mathbf{R^n}, \tag{2.79}$$

to optimize

$$\mathbf{f}(\mathbf{b}, \mathbf{z}, \mathbf{t}), \tag{2.80}$$

subject to

$$\mathbf{M}(\mathbf{b})\ddot{\mathbf{z}} + \mathbf{K}(\mathbf{b})\mathbf{z} = \mathbf{f}(t), \tag{2.81}$$

$$\mathbf{g_j}(\mathbf{b}, \mathbf{z}, \mathbf{t}) \leq 0, \qquad j = 1, \dots, m, \tag{2.82}$$

$$\mathbf{b_L} \leq \mathbf{b} \leq \mathbf{b_U}; \tag{2.83}$$

(2.79) is imposed as equality constraints as shown in (2.83). Dynamic response optimization is the process of obtaining the design solution of (2.79) to (2.83). It is different from the static response optimization in (2.62) to (2.71) because the time variable is included in the functions. Usually, numerical methods are utilised to solve the problem in (2.79) to (2.83). In a numerical method, the time should be discretized and the constraints in (2.81) and (2.83) are generated for each of the discretized time steps. As a result, the previously mentioned disadvantage manifests, and a large number of time dependent constraints need to be handled. This issue can be tackled in different methods, such as integration in time domain or estimation only of peak values, but as described by Park (2007) [72], these methods do not reduce the level of complexity significantly. Therefore, the dynamic response optimization is not compatible with large scale optimization problems. As a conclusion, it can be outlined that it is more convenient to convert the dynamic equation to a static equation and run the optimization as a static load problem in an iterative manner.

For an optimization problem with the aim to maximize the elastic deformations in one of the layers of the active element with a constrain on the geometric shape, the mathematical problem solution can be expressed as shown in the computational scheme (Figure 2.9) and formulated as described by the equations (2.84 – 2.87).

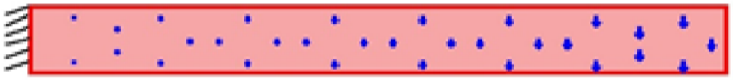

Figure 2.9. Computational scheme of the shape optimization problem of the active element of the energy harvester: initial shape, boundary condition, distributed spatial load;

For the dynamic problem, which is the transient vibration of a cantilevered harvester, to be solved in statics, the aim function can be written as (2.84).

$$\max Z = \int_0^L \left|\frac{du}{dx}\right| dx; \tag{2.84}$$

Together with the system of limiting equations, the equation of state (2.85) and limitation of the thickness of the active element are expressed as (2.86).

$$[\mathbf{K}]\{\mathbf{U}\} = \{\mathbf{F}\}; \tag{2.85}$$

Limitation to the thickness of the active element (2.86) and the project variables are as written in (2.87):

$$H_{min} \leq q_0 + q_1 x^1 + q_2 x^2 + q_3 x^3 \leq H_{max}, \tag{2.86}$$

$$[\mathbf{Q}] = (q_0, q_1, q_2, q_3); \tag{2.87}$$

where Z represents elastic deformations along the edge of the active element, H – thickness of the active element, project parameter, **K** – Stiffness matrix and (2.82) equation of state, **U** – displacement vector, F – force factor of external effect, L – length of the active element, and **Q** – Vector of project variables (2.85).

2.7. Discrete Furrier Transform analysis.

This chapter introduces the Discrete Fourier Transform (DFT) and points out the mathematical elements that will be explicated in this thesis. For a better understanding of DFT, first of all, FT has to be investigated. The Fourier transform of a continuous-time signal $x(t)$ may be defined as.

$$X(\omega) = \int_{-\infty}^{\infty} x(t) e^{-j\omega t}\, d(t), \quad \omega \in (-\infty, \infty); \tag{2.88}$$

The DFT, on the other hand, replaces the infinite integral with a finite sum:

$$X(\omega_k) \triangleq \sum_{n=0}^{n-1} x(t_n)\, e^{-j\omega_k t_n}, \quad k = 0,1,2,\dots,N-1; \tag{2.89}$$

Smith (2007) [101] noted that calculus is not needed to define the DFT (or its inverse). Thus, if finite summation limits are used, the infinities should cause no difficulties either. DFT is simpler mathematically than but as practical as Fourier transform. Therefore, it is more convenient to use. The Discrete Fourier Transform (DFT) of a signal x may be defined by as shown in (2.89) where $\triangleq$ means 'is defined as' or 'equals by definition':

$$\sum_{n=0}^{n-1} f(n) \triangleq f(0) + f(1) + \cdots + f(N-1); \tag{2.90}$$

here, $x(t_n)$ is the input signal amplitude of any form at time t_n in seconds, and t_n or nT is the nth sampling instant in seconds of the sampling interval T, where n is an integer that is bigger than zero. $X(\omega_k)$ is spectrum of x (complex valued), at frequency ω_k. Ω or $\frac{2\pi}{NT}$ is the radian-frequency sample (radians per second) and f_s or $\frac{1}{T}$ is the sampling rate (samples/sec, or Hertz (Hz)). N is the number of time samples.

In common literature concerning the DFT, it is more common to use the set sampling interval $T = 1$.

$$X(k) \triangleq \sum_{n=0}^{n-1} x(n)\, e^{-j2\pi nk/N}, \quad k = 0,1,2,\dots,N-1, \tag{2.91}$$

$$x(n) = \frac{1}{N \sum_{n=0}^{n-1} X(k) e^{-\frac{j2\pi nk}{N}}}, \quad n = 0,1,2,\dots,N-1; \tag{2.92}$$

here, $x(n)$ denotes the input signal at time sample n, and $X(k)$ denotes the k^{th} spectral sample. This form is simplest mathematically, while the previous form is easier to interpret physically. To conclude, the DFT is a tool to investigate a time-based pattern if it is a frequency distribution within harmonics or spectral analysis of the light beam going through an atmosphere of unknown gases.

2.8. Section Conclusions.

In this section, different aspects related to the modelling of a piezoelectric vibration energy harvester were analysed. This included mathematical and numerical modelling and model optimization problem solving techniques. The equations describing the electromechanical coupling were given and explained along with equations for load bearing material and their differential forms for the Finite Element model solution. Since the most common type of piezoelectric energy harvester is a cantilevered type, the Bernoulli beam theory was introduced to get a better understanding of mechanical aspects of the vibration energy harvester as a deformed body. For the solution of differential governing equations, the FE method was investigated and explained as it offers a relative simplicity and reliability of the calculations. The theory and steps of the FE method were investigated and explained in this section.

Since vibrations energy harvesters cannot be easily or cheaply built without prior modelling of their mechanical and electrical aspects, the next section investigated aspects of the coupled piezoelectric circuit model. The modelling of a coupled piezoelectric circuit (CPC-FEM) is explained in one of the chapters.

The dynamic contact modelling using the nonlinear viscoelastic contact model by Hunt and Crossley was investigated because it is particularly important for frequency-up converting devices utilizing impact coupling. Direct contact of solid bodies produces great nonlinearities which cannot be studied properly without a precise and reliable contact model.

And finally, some numerical methods (mathematical optimization, discrete Fourier transform (DFT)) were analysed for solving optimization problems for energy output maximization from piezoelectric vibration energy harvesters with constrains for geometrical parameters of eigen values.

In general, this section presented the mathematical and numerical models used for numerical analysis in further chapters of this thesis.

- The mathematical model was created for the piezoelectric vibration energy harvester operating in higher transverse vibrations modes using equations to describe electromechanical coupling, dynamic processes taking place in the load bearing material and coupling the model with electrical circuit to predict the electrical parameters of the harvester.
- The dynamic contact model was created and used in the mathematical model for energy harvester operating in vibro-impacting mode.
- The mathematical models were created for solving the mathematical optimization problems, total normal strain output maximization with constrains to geometrical shape and harvester volume minimization with constrains to the eigen frequencies, namely the second resonant frequency.

3. SIMULATION OF AUTONOMOUS PIEZOELECTRIC ENERGY HARVESTERS.

The following section describes the elaboration of PEH prototypes. The aim of this section is to present the developed finite element models and their simulation results as well as their numerical analysis.

During the early stages of the device design, it is very convenient to use FE modelling for accurate prediction of how the device will perform with different design parameters. This feature is as much time saving as money saving. As a result, one of the objectives of this research was to develop a general and universal coupled finite element (FE) model of a piezoelectric vibration energy harvester, parameters of which could be easily changed. An electrical circuit was attached to the model to allow a more accurate prediction of the power output levels of the device as well as the impact of electrical loads on the dynamic parameters of the harvester.

The ultimate purpose of FE analysis is to mathematically recreate the behaviour of an actual engineering system. In other words, we have to obtain an accurate mathematical model of a physical prototype. Thus, FE model usually contains nodes, elements, material properties, real constants, boundary conditions and other features that are used to represent a physical system.

Further sections shall provide detailed descriptions of the developed FE models, their geometry parameters, material properties and definitions, mesh parameters, loads, constraints and limits, simulation results and their numerical analysis.

3.1. Investigation of optimal segmentation of PVEH at higher vibration modes.

Two objects, energy harvesting active elements, were investigated. The first one is a common, constant cross section area active element, and the second one is an active element of an optimized shape. The optimization was done using mathematical optimization techniques where the aim function was to minimize the mass of the active element with restrictions to geometrical shape and eigen frequencies. The second eigen frequency ω_2 had to remain unchanged and equal to the corresponding frequency of the constant cross-section active element. The normalized shape of the optimized shape active element can be seen in Figure 3.1. PVDF or polyvinylidene fluoride was used as the piezoelectric material. PVDF was cut into two elements that were attached to the top surface of the active element with directions of polarization opposite to each other. Active elements were modelled as uniform composite beams for linearly elastic deformations and geometrically small oscillations based on the Euler–Bernoulli beam assumption.

As described by Erturk (2015) [102], and as the theory of thin beams dictate, shear deformations and rotary inertia can be neglected as the design of the presented harvesters do not violate the conditions for the thin beam. The principal diagram of an energy harvester of a constant cross-section area is shown in Figure 3.2. The piezoelectric elements are segmented in strain node points; thus, the first piezoelectric element covers the surface of the active element from the fixed end to the strain node, and the second is attached from the strain node to the free end of the active element. Mechanical and geometrical properties of both constant cross-section area and

optimized shape energy harvesters are given in table 3.1. Table 3.2 provides the piezoelectric properties for the PVDF. The eigen frequencies given in table 3.1 were obtained from modal analysis which is described further in this section.

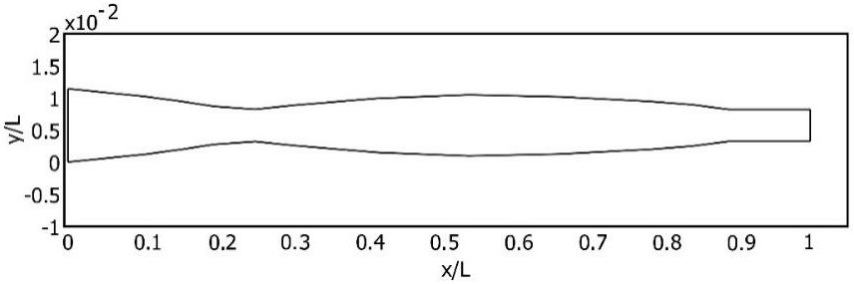

Figure 3.1. Normalized shape of the optimally-shaped active element

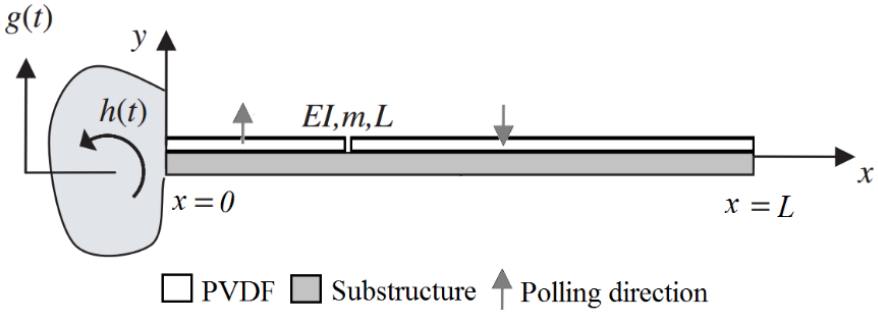

Figure 3.2. Unimorph Piezoelectric active element ever under base motions with a pair of PVDF elements attached

Table 3.1. Mechanical and geometrical properties of the considered active element setups

Parameter	Constant Cross-Section Area Active element	Optimal Shape
ω_1, Hz	86	66
ω_2, Hz	541	534
Density, kg/m^3	7850	
Elastic modulus, N/m^2	2×10^{10}	
Poisson's ratio	0.33	
Length, m	0.1	
Width *a*, m	0.01	
Thickness *b*, m	1×10^{-3}	Varying from 4×10^{-4} to 1×10^{-3}

The constitutive equation for the load bearing material of the energy harvester under linear elasticity assumption is described in section 2 of this thesis by equation (2.47). The coupling of the electrical and mechanical domains is best described by equations (2.50) and (2.51) which describe the electromechanical conversion phenomena. The electrical potential decreases linearly through the thickness of the piezoelectric material layer if the material is deformed by applying axial stress T_1. As

a result, charge is accumulated at the electrodes. Under open circuit boundary conditions (D = 0), the voltage across the piezoelectric material can be calculated as described in equation (2.53).

Table 3.2. Piezoelectric properties of PVDF

Parameter	Name	PVDF	Units
d_{31}	Piezoelectric strain constant	23	(pC/N)
g_{31}	Piezoelectric stress constant	216	(10^{-3} Vm/N)
k_t	Electromechanical coupling factor	12%	
C	Capacitance	1.4–2.8	nF
Y	Young's modulus	4	10^9 N/m^2
ε	Permittivity	110	10^{-12} F/m
ρ	Mass Density	1780	kg/m^3
t	Thickness	64	μm

While the load bearing material is vibrating in its second resonant frequency, the piezoelectric material layers that are attached to the substrate are also deformed. As a result, a voltage potential is generated across the piezoelectric material. Both positive (stretching) and negative (compression) strains can be detected in two different points of the same surface of the active element at any given time instant. A point where the positive and the negative strains meet is called a strain node. This strain node can be detected from the modal analysis or found from the dynamic analysis using numerical methods. Figure 3.3(a) illustrates the second transverse mode shapes obtained from the modal analysis of both types of energy harvesters, i.e., the constant cross-section area and the optimized shape. In Figure 3.3(b), the normal strain distribution of the second transverse vibration modes is presented. The strain node of both active element types is presented in Figure 3.3(b) where the strain mode shape crosses the 0 axis of the normal strain.

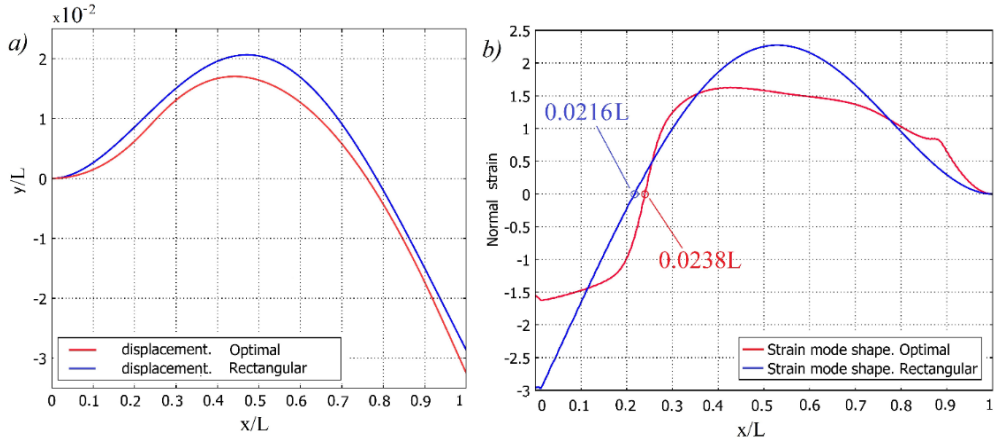

Figure 3.3. Second transverse vibration mode of an active element: (a) displacement; (b) normal strain; along the upper edge of active element

The strain node for the constant cross-section active element is at 0.0216L and for the optimized shape active element at 0.0238L, where L is the length of the active element. It can also be seen that the slope of the normal strain distribution curve in close proximity to strain node has a high gradient, meaning that the area on the surface of the active element where the strain sign is alternating is narrower. This can lead to lower charge cancelation on the electrodes if the electrodes were retracted from the mentioned area.

In Figure 3.4, the second mode shapes of both types of the active element are presented with normal strain fields of their cross-sections. It can be observed that the upper and lower faces of the active element are subjected to the strains of different signs; while the upper face is negatively strained (compressed) at x/L = 0, the lower face is under tension.

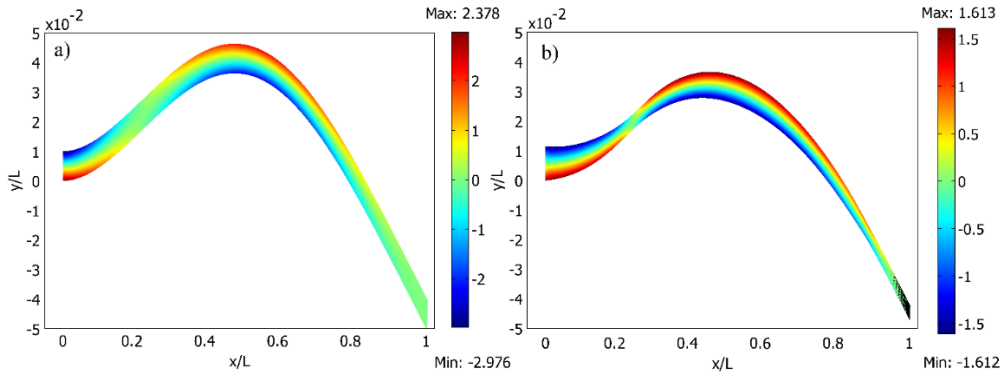

Figure 3.4. The second transverse vibration mode of the active element and the field of normal strain distribution: (a) active element of a constant cross-section; (b) optimally-shaped active element

The transient analysis of the active element was conducted to verify the position of the strain node in the active element during its base excitation with time varying force f(t) acting on it. An equation of motion (2.55) was used as described in section 2 of this thesis. The time-dependent force f(t) is described as active element body load in the vertical direction and is defined as the force/volume using the thickness as described in equation (2.56).

The dynamic response of the active element to the ambient vibrations can be found solving the equation of motion since it controls the linear dynamic behaviour of the body under time varying force. The transverse displacement of the tip of the active element obtained from transient analysis is presented in Figure 3.5(a). The vibration starts from the resting point and runs up from that point until gradually decreasing to the point where the steady state vibrations begin. In Figure 3.5(b), a range of steady state vibrations is shown with points t1 and t3 marking the half-period of tip vibrations selected for further investigation, t2 is the middle-point of that half-period. A magnified view of t1-t3 interval is shown in Figure 3.5(c). The first quarter of ½ T period is marked in blue and the second one in red.

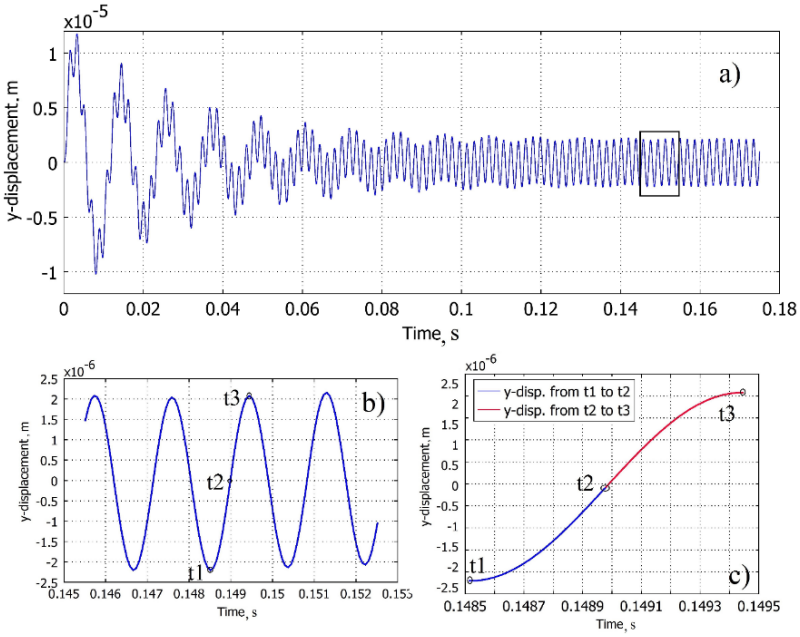

Figure 3.5. Transverse displacement of the active elements tip: (a) dynamic process; (b) region of steady-state vibrations; (c) ½ T period of vibration for further analysis

For the sake of simplicity, the same colouring scheme is used in Figure 3.6 where the normal strain distribution along the upper edge of the active elements are presented. The number of curves in Figure 3.6 represents the number of samples Δt_i between t1 and t3, depicting intermediate normal strain curves.

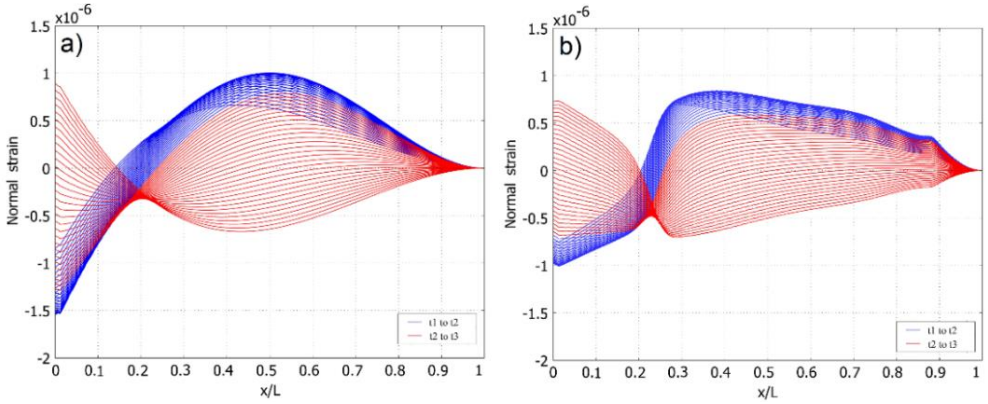

Figure 3.6. Normal strain distribution curves along the active element's length per ½ T obtained from transient analysis: (a) active element of a constant cross-section; (b) optimally-shaped active element

Figure 3.7 illustrates the mode shapes of the constant cross section area active element ever and the optimized shape active element with normal strain distribution fields at t1, t2 and t3. Figures 3.5 and Figure 3.6 clearly reveal that, normal strain

output amplitudes are overall higher in the case of the active element of a constant cross-section.

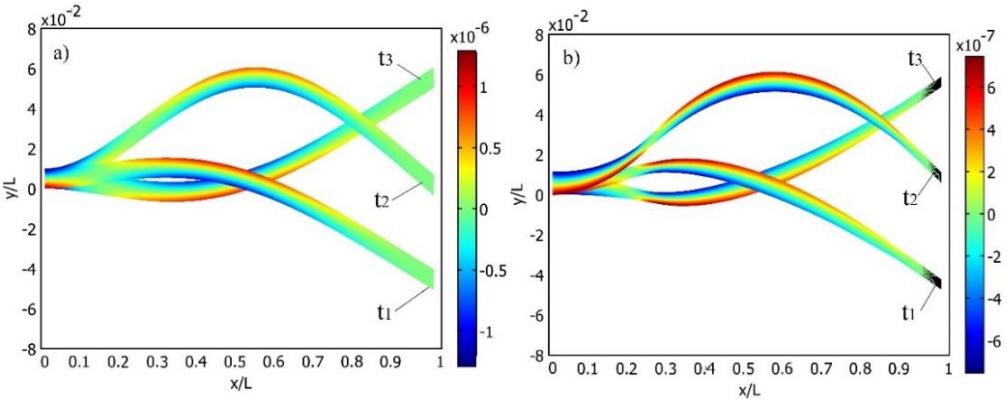

Figure 3.7. Mode shape and normal strain distribution field at t1, t2 and t3 of (a) the constant cross-section area active element (b) optimally-shaped active element

The normal strain field along the upper edge of the active element versus time is presented in Figures 3.8(a) and (b). For constant cross-section area and for the optimized shape active element, the time interval depicted is from t1 to t3, respectively, which is the same as shown in Figures 3.6 and 3.7. The horizontal axis of Figure 8 represents a normal strain distribution along the upper face of the active element of a constant cross-section at time instant t_i, while the vertical axis represents a strain change at any given point per time interval [t1, t3]. It can be directly seen from Figure 3.8(a) that the constant cross-section area active element produces higher amplitudes of strain, especially at the negative side of the spectra, while the optimized shape active element (Figure 3.8(b)) demonstrates higher gradients of the normal strain change.

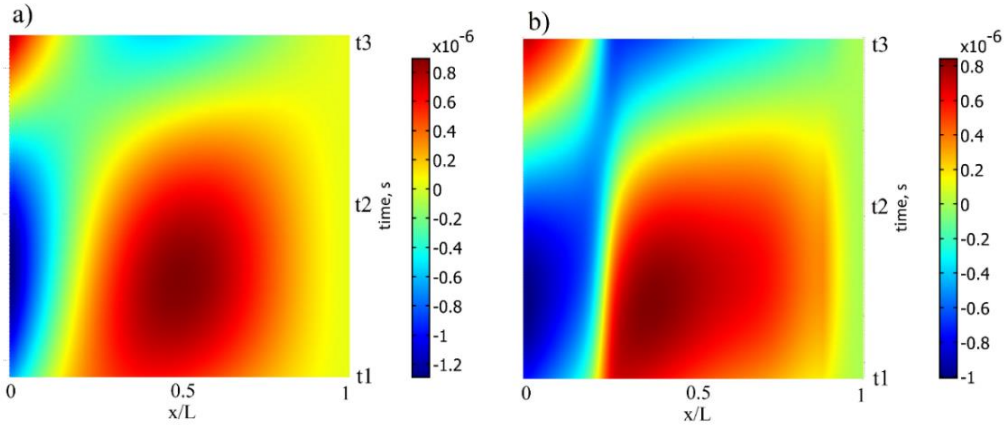

Figure 3.8. Normal strain distribution on the upper face of the active element per time interval t1 to t3: (a) active element of a constant cross-section; (b) optimally-shaped active element

The simulation results obtained from the modelling environment COMSOL were gathered and processed using numerical methods. For this purpose, MATLAB numerical computing environment was used. Figure 3.8(a) and (b) shows that the region where the normal strain is close to 0 (depicted in green) is significantly wider with respect to the length of the active element for the constant cross-section area active element than for the optimized shape active element from t1 to t2. This zone drifts slightly from 0.1L to approximately 0.2L, and from t2 to t3 spreads from 0.1L to the free tip of the active element. The behaviour of the optimized shape active element is depicted in Figure 3.8(b). The normal strain field is much more expressed and the region where the normal strain is close to 0 is much narrower here.

The mathematical methodology has been developed to accurately calculate the location of the strain node along the edge of the active element using the data from the transient analysis data, where the average value of strain per ½ T is 0. A further goal is to compare the normal strain output on both sides of the strain node calculated from the modal analysis and the transient analysis to prove that the transient analysis provides a more accurate location of such a point leading to an increased efficiency of the energy harvester.

The time interval between t1 and t3 was divided into interpolated time steps Δt_i. The time increment Δt between the time steps Δt_i was calculated as shown in equation (3.1).

$$\Delta t = \frac{t_3 - t_1}{N}; \tag{3.1}$$

The aim of this problem is to determine the point along the edge of the active element where the average strain per time interval from t1 to t3 is equal to 0, in other words - to determine the strain node. This is achieved by integrating the area bounded by each interpolated normal strain distribution curve at time steps from Δt_1 to Δt_N over an increment of the length of the active element. Simpson's method is used for integration and the approximation is shown in (3.2):

$$\int_0^L \frac{du}{dx} dx \approx \frac{h}{3}\left[\frac{d(u_0)}{dx} + 2\sum_{j=1}^{\frac{N}{2}-1} \frac{d(u_{2j})}{dx} + 4\sum_{j=1}^{N/2} \frac{d(u_{2j-1})}{dx} + \frac{d(u_N)}{dx}\right]; \tag{3.2}$$

Here, u is the displacement in the axial direction along the length of the active element. The calculation was done in MATLAB. To verify the calculations, the integration was performed from the fixed and to the free end of the active element, and from the free end to the fixed end of the active element. Integration results are plotted in Figure 3.9(a) and (b), constant cross-section area and optimized shape active elements, respectively. The curves represent the accumulation of the strain over an increment of the length of the active elements. It can be seen that following the red curve from the left to right, which represents the integration from the fixed end to the tip of the active element, the curve gradually goes up while the strain is accumulated, and as the curve reaches its peak, the strain node is reached. The added negative strain decreases the total amount of the accumulated strain, hence the curves start declining. If the strain was replaced by charge, it would illustrate the charge cancelation effect. The strain node location (square marker) for integration from left to right and vice

versa coincide and is approximately at 0.238L for the constant cross-section area active element and at 0.259L for the optimized shape active element. From Figure 3.9(a) and (b), it can also be seen that these points do not coincide with the strain node location acquired from the modal analysis (circular marker).

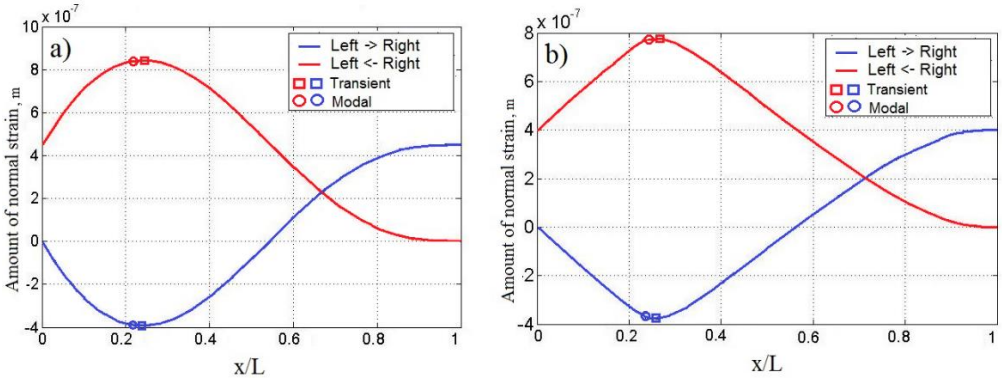

Figure 3.9. Accumulation of normal strain over length x/L per ½ T: (a) active element of a constant cross-section; (b) optimally-shaped active element

The strain node locations are given in table 3.3 along with the integration results for both types of active elements at each side of the strain node, (these represents the charge accumulated and left and right piezoelectric material element) both acquired from the modal and transient analyses. The segment to the left from the strain node produced positive strain output, while the segment to the right produced negative. The total strain sum of the active element is the sum of the strain output of both segments in absolute values. Table 3 indicates that the total strain gain for the constant cross-section area active element segmented in the strain node obtained from transient analysis was 5.5% and for the optimally shaped active element – 5.2%.

Table 3.3. Comparison of normal strain amount

	Strain Node	**Amount of Normal Strain-Left (Dimensionless)**	**Amount of Normal Strain-Right (Dimensionless)**	**Gain, %**
		Active el. of a constant cross-section		
Modal solution	0.216	6.53×10^{-10}	-9.7×10^{-10}	
Transient solution	0.238	6.73×10^{-10}	-9.9×10^{-10}	+5.5%
		Optimally-shaped active el.		
Modal solution	0.239	6.3×10^{-10}	-9.6×10^{-10}	
Transient solution	0.259	6.5×10^{-10}	-9.85×10^{-10}	+5.2%

The numerical calculation results clearly reveal the superiority of the strain node calculation using the developed calculation methodology. The results were calculated for the unimorph configuration of the harvester, and the actual gain would double for bimorph configuration.

3.2. Electric Power Output Maximization by Optimizing Resistive Load.

AC power output of a PVEH operating in the second resonant mode and the effect of varying resistive load on power output of PVEH is investigated. AC power output characteristics of layers connected in parallel, as shown in Fig. 3.10(a) or series Fig. 3.10(b) was investigated. The load bearing layer is made of aluminium and PVDF is chosen as a piezoelectric material due to its flexibility and lightness. Heavier and harder piezo-ceramics were not chosen because of their significant contribution to the overall dynamics of the PVEH, while the effect of PVDF can be neglected. Consecutive equations of the load bearing and piezoelectric materials are more fully explained by Erturk (2009) [103]. The first PVDF layer is mounted from the fixed end of the active element to the strain node, and the second one is fixed from the strain node up to the active element end on the opposite face of the active element. The PVDF layers attached are of same polarization; therefore, the charge produced is of same sign and can be harvested with a relatively simple circuit. The displacement of active elements in the y direction in the second natural mode of PVEH and electric potentials of PVDF layers are shown in Fig. 3.10.

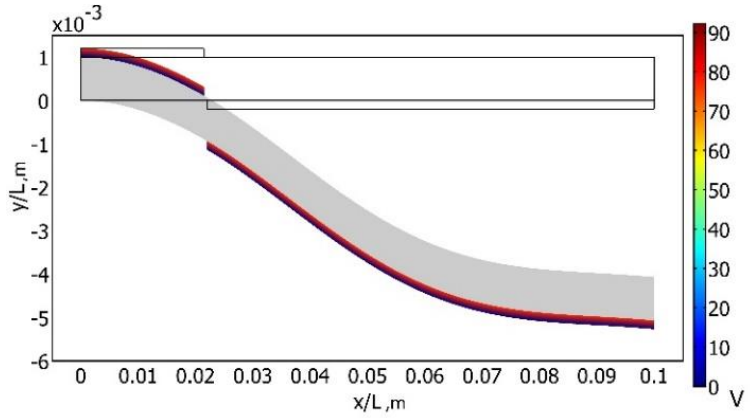

Figure 3.10. Second natural mode of PVEH and electric potentials of piezoelectric layers

The load resistance R_l is connected in series with the piezoelectric elements in the first case and in parallel in the second case producing AC current. The geometric parameters as well as other mechanical characteristics of PVEH can be found in Table 3.4. The modal analysis of the system was done with the aim to obtain the resonant frequency. The harmonic analysis was performed in order to obtain the electric power output of PVEH versus load R_l. FE mesh with 700 elements per length of the active element was implemented. A coupled piezoelectric-circuit finite element model (CPC-FEM) was used for solving this problem. The system was modelled using COMSOL multi-physics with SPICE piezoelectric circuit attached. Harmonic base excitation of the frequency matching the second resonant frequency of the transducers was used with an acceleration of 1.3g. The parameters of the excitation are varied by the frequency ω_n of the time-dependent force f(t). A quadratic Lagrange element type with the second-order polynomial approximation was used. The piezoelectric element

can be modelled as an equivalent circuit of the current source I_{piezo} in parallel with a capacitor C_i as shown in Fig. 3.11(c) and Fig. 3.11(d). The piezoelectric PVEH has high impedance in order of MΩ; thus, it may be considered as purely capacitive element with capacitance of pF order. The capacitance of the piezoelectric element C_p can be found from Equation (3.3), and the impedance of piezoelectric element Z_p can be found as shown in Equation (3.4).

Table 3.4. Mech. and geometrical properties of substrate layer and PVDF properties

Parameter	Substrate layer	Parameter	PVDF
Density, kg/m^3	2700	Piezoel. strain constant, d_{31}, (pC/N)	23
Elastic modulus, N/m^2	$0{,}69 \times 10^{11}$	Piezoel. stress constant, d_{31}, (Vm/N)	216×10^{-3}
Poisson's ratio	0,33	Electromechanical coupling factor, k_t,	12%
Length, *L*, m	0,1	Capacitance, C, nF	1,4-2,8
Width *a*, m	0,01	Young's modulus, Y, N/m^2	4×10^9
Thickness *b*, m	0,001	Permittivity, ε, F/m	110×10^{-12}
PVDF Segm. line, m	0,0238	Mass Density, ρ, kg/m3	1780
		Thickness, t, μm	45

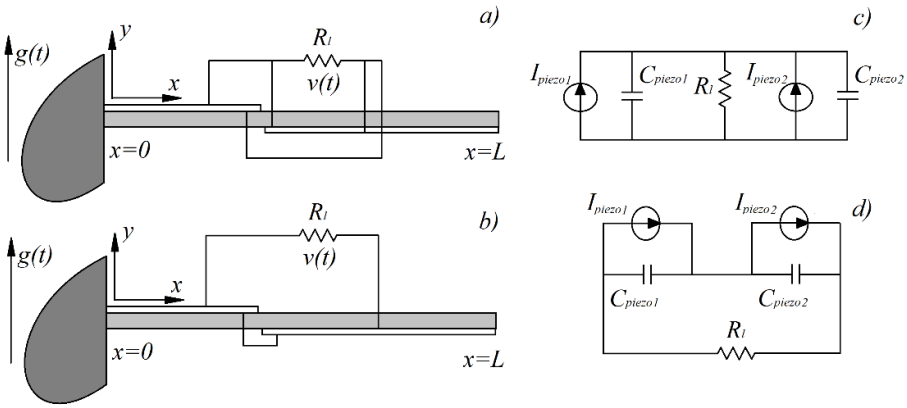

Figure 3.11. Piezoelectric active element under translational base excitation with PVDF segments connected a) in parallel, b) in series. Electrical circuit of PVEH with piezoelectric outputs connected in c) parallel and d) series connection

$$C_p = \frac{K\varepsilon_0 A}{t}, \tag{3.3}$$

$$Z_p = \frac{1}{2\pi f C_p}; \tag{3.4}$$

Here, *A* is the surface area of the piezoelectric layer, and *t* represents the thickness. *K* is the dielectric constant, which is the ratio between the permittivity of the piezoelectric material *ε* and the permittivity of the free space ε_0. In Equation (3.4), *f* is the excitation frequency. For the maximization of the power transfer, the load resistance has to be matched with the internal impedance of the piezoelectric elements of the transducer which will be different for series and parallel connections of

piezoelectric elements. The optimal load resistance is equal to the equivalent impedance of combined internal impedances of PVDF layers. The calculated combined impedance of both PVDF layers for series connection is $Z_{pS} = 127168\,\Omega$ and the parallel connection is $Z_{pP} = 29355\,\Omega$. For the series connection, the combined impedance is simply the sum of impedances of both piezoelectric layers $Z_{pS} = Z_{p1} + Z_{p2}$ and $\frac{1}{Z_{pP}} = \frac{1}{Z_{p1}} + \frac{1}{Z_{p2}}$ for the parallel connection.

The second resonant frequency found from the modal analysis was 644 Hz. The frequency-amplitude response obtained from the harmonic analysis is shown in Figure 3.12, and it confirms the modal analysis results. The obtained eigen-frequency was then inserted into the harmonic analysis models to obtain the voltage and current outputs with varying load resistances for series and parallel connections. The obtained characteristics, such as the voltage output, the current output and the PVEH electric power output are shown in Fig. 3.13 – 3.15, respectively.

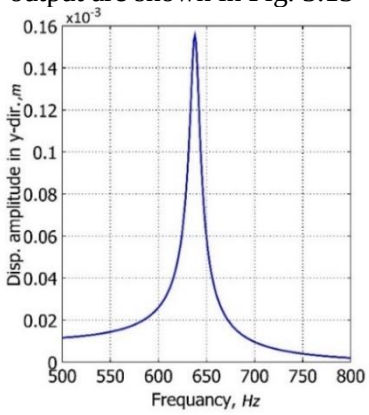

Figure 3.12. Amplitude-Frequency response characteristics of the tip of the active element

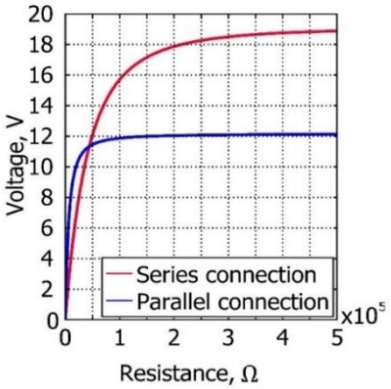

Figure 3.13. Voltage output of parallel and series connection

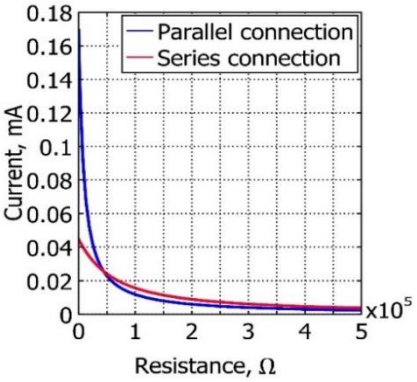

Figure 3.14. Current output of parallel and series connection

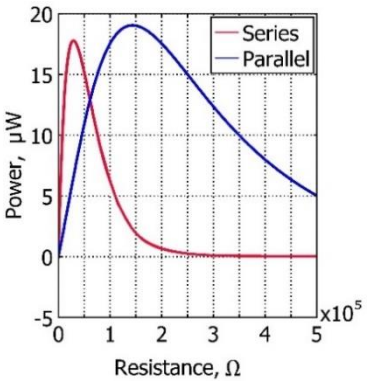

Figure 3.15. Power output of parallel and series connection

As shown in Figure 3.13, the voltage output of series connection is nearly double of that obtained from parallel connection. A drop in the output current can be observed as the voltage output increases with the increasing load resistance (see Figure 3.14). Figure 3.15 shows that a similar power output (8% difference) is obtained from both series and parallel connections. Peak power output values are reached at optimal resistances. It can be observed that the optimal resistances for both setups are different. Optimal resistance for the parallel connection is found to be at 127 kΩ, and for the series connection at 29 kΩ. The results comply well with calculated values of the impedance of the piezoelectric elements Z_{pP} and Z_{pS}. The simulation results comply well with the theoretical calculations of the optimal resistive load. It is obvious that the resistive load varies significantly for parallel (127 kΩ) and series (29 kΩ) connected piezoelectric material layers. An appropriate connection can be chosen if larger output voltage or current is desired. The difference between the output power of PVEH connected in series (17.5 μW) and in parallel (19.2 μW) connections is small (8%) but the outputs were expected to be equal with same initial conditions. For this, the impact of varying resistive load on dynamics of PVEH is suspected. Significantly larger power outputs are expected from PVEH using piezo-ceramics instead of PVDF due to a larger piezoelectric constant but the effect on dynamics of the active element has still to be investigated.

3.3. Investigation of dynamics and transient process of Multibeam PVEH with frequency-up conversion.

A frequency up-converting tandem is investigated. The tandem consists of a low frequency resonator (LFR) and a high frequency piezoelectric vibration energy harvester (PVEH). A schematic representation of the energy harvesting "tandem" can be seen in Figure 3.16.

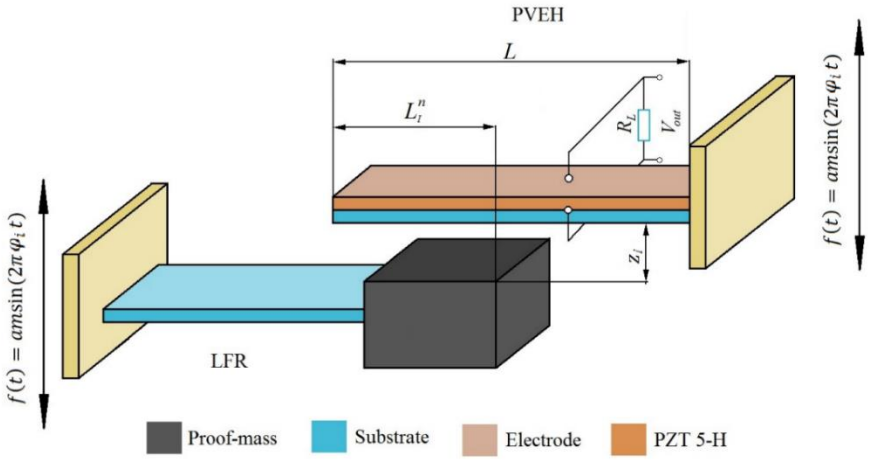

Figure 3.16. Schematic representation of the device – LFR and PVEH suspended on the same substructure

The LFR consists of a steel active element and a proof mass attached to its tip. Different transverse vibration eigen frequency ratios were achieved by varying the

geometry and the proof-mass of LFR while the geometry of PVEH was kept constant for the entire analysis. The piezoelectric active element was modelled as a uniform composite beam subjected to linearly elastic deformations and geometrically small oscillations with the reference to the Euler–Bernoulli beam assumption. Table 3.5 presents the mechanical and geometrical of properties of the PVEH. A thin layer of PZT-5H piezoelectric material was attached on the upper surface of the high frequency piezoelectric energy harvester; upper and lower surfaces of the piezoelectric material were modelled as ideally conductive electrodes of negligible thickness. The dimensions of PVEH were 10 x 0.3 x 0.001 mm (i.e., the length, width and thickness, correspondingly).

Different configurations of the energy harvesting tandem were investigated. The piezoelectric vibration energy harvester (PVEH) design and the geometrical properties were kept constant, while the first natural frequency of the low frequency resonator (LFR) was altered. In total, five configurations of LFR were investigated with natural frequencies ω_i^{LFR}= (311, 207, 155, 103, 77) Hz, where i = 1, 5 and represented the configuration number.

Table 3.5. Mechanical and geometrical properties of the proposed Piezoelectric Vibration Energy Harvester (PVEH) load bearing material (PET)

Parameter	Value
ω_1^{PVEH}, Hz	622
Density ρ, kg/m^3	1430
Young's modulus, Pa	4.6×10^9
Poisson's ratio	0.33
Length l, m	0.01
Width *a*, m	0.003
Thickness *b*, m	0.0001

The geometric and piezoelectric properties of the piezoelectric material (PZT-5H) layer are listed in Table 3.6.

Table 3.6. PZT-5H properties

Parameter	Value
Piezoelectric strain constant d_{31}, (pC/N)	-320
Piezoelectric stress constant g_{31}, (10^{-3} Vm/N)	550
Electromechanical coupling factor k_t	41%
Young's modulus Y, 10^9 N/m^2	6,3
Permittivity ε, 10^{-12} F/m	3130
Mass Density ρ, kg/m^3	7800
Thickness t, m	0.00008

The five-different configurations of the energy harvesting tandem were also excited by different harmonic ambient vibration frequencies φ_i, which was always equal to corresponding ω_i^{LFR}. The distance between the LFR and PVEH at rest is denoted by z_{gap}. For different configurations of the LFR and PVEH tandem, different gap distances z_{gap} were used. As each configuration of the tandem was different with respect to LFR excitation and natural frequency, their amplitude of vibrations was also different, i.e., the lower the frequency, the higher vibration amplitude. Thus, z_{gap}

was chosen so that the indentation of LFR at its peak transverse vibrations was equal to the thickness of the PVEH. As a result, at its peak, the vibration LFR would hit the PVEH creating a dynamic contact point and forcing the PVEH to operate in a vibro-impact mode.

In addition to the five configurations of LFR, different dynamic contact locations between PVEH and LFR were investigated. The dynamic contact point is denoted by L_l^n (where n = 0 = $\underline{0L}$ and n = 7 = $\overline{0{,}6\mathrm{L}}$). The contact point was shifted from the tip of PVEH (0L) towards the fixed end by increments of 0.1L up to 0.6L. A coupled 2D CPC-FEM circuit consisting of a simple resistive electrical load R_l was attached to the piezoelectric element of the energy harvester. The purpose of the electrical load is to mimic an impact of the real electrical load, since from the literature review it is known that an electrical circuit attached significantly influences the vibration response of the energy harvester. An electrical load also enables to predict the generated power output. Obviously, the resistive load alone is a simplified version of a real-life circuit and it cannot account for all possible influences. However, this was not the scope of this thesis.

The circuit was created using SPICE, general-purpose circuit simulator, which attached to a COMSOL created LFR-PVEH model. PVEH and LFR were modelled using the Lagrange-quadratic FE for plane-strain approximation. The LFR and PVEH tandem was excited cinematically by the harmonic law in the transversal direction; a kinematic effect in the model is described as a body load with magnitude controlled by imposed acceleration (a = 0.85 g) and excitation frequency φ_{i} (where φ_i=$\omega_{1\mathrm{i}}^{LFR}$). The transverse vibration eigenfrequency ratios investigated were $\omega_1^{PVEH}/\omega_1^{LFR}$= (2; 3; 4; 6; 8), where ω_1^{PVEH} and ω_1^{LFR} are the first transverse vibration eigenfrequencies of the high frequency PVEH and LFR, respectively.

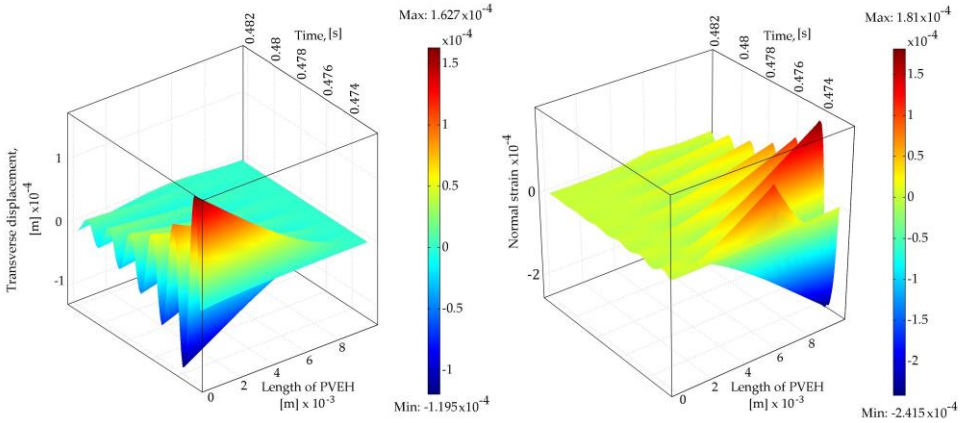

(a) **(b)**

Figure 3.17. Dynamic process of the PVEH from the instant of impact to fully decayed vibration (LFR—103 Hz, contact point position at 0.6 L) (a) transverse displacement and (b) normal strain distribution through the length of the PVEH

The PVEH is driven by the energy from the dynamic impact occurring between the LFR and PVEH during base excitation of the harvesting tandem. The nonlinear dynamic behaviour is controlled by the equation of motion, which is solved to find the dynamic response. The dynamic analysis of different LFR geometries was performed to model the PVEH dynamics process. Then the LFR was kinematically actuated by its first transverse vibration mode eigen frequency. A transient analysis was conducted to obtain the dynamic response of the LFR-PVEH tandem under harmonic base excitation and dynamic contact between the two active elements under open circuit conditions ($R_L \rightarrow \infty$), as shown in Figure 3.17. From Figure 3.17(a, b), the amount of normal strain is highest at the fixed end of the active element (Figure 3.17(b)) when the displacement is at its maximum as seen in Figure 3.17(a). As the vibration decays, the normal strain in the length of PVEH also decays. From Figure 3.17(b), it can also be seen that the amount of the positive normal strain is higher than that of the negative one, which can be related to the impact coupling. Figure 3.18 denotes the vibration response of PVEH and LFR for different tandem configurations: (LFR ω_i^{LFR} = (311, 207, 155, 103, 77 Hz) resulting in $\omega_1^{PVEH}/\omega_i^{LFR}$ = (2, 3, 4, 6, 8), respectively). The dynamic contact location for the denoted figures is at L_I^6 = 0.5L.

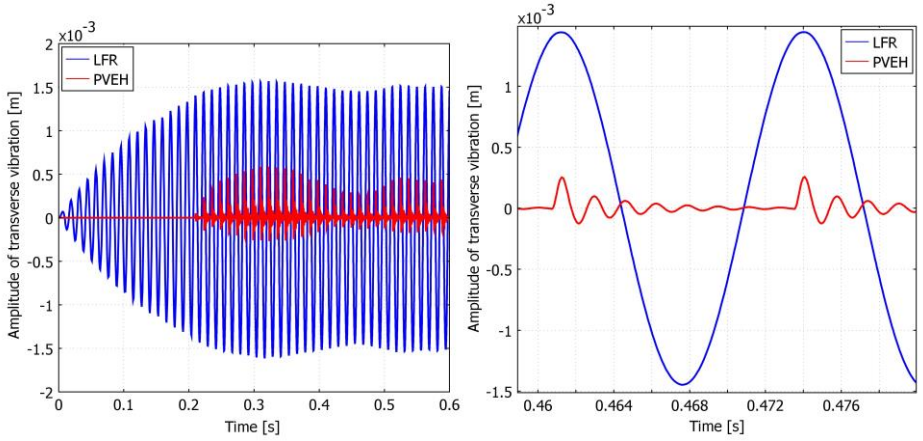

(a)

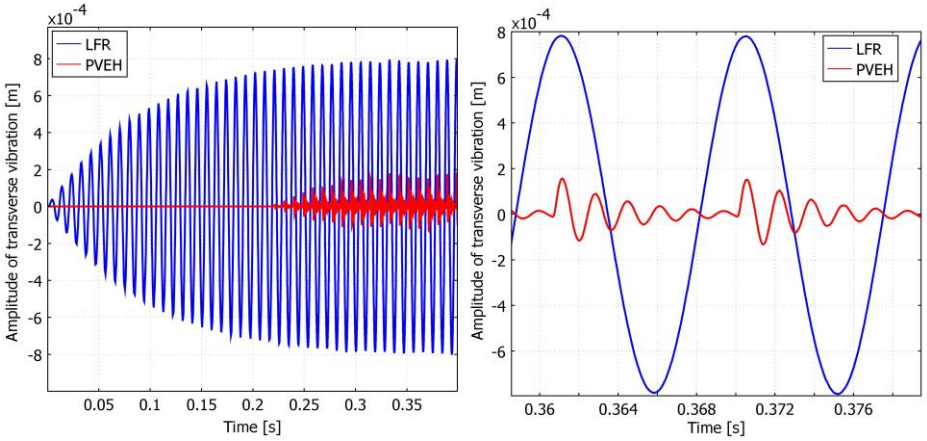

(b)

Figure 3.18. *Cont.*

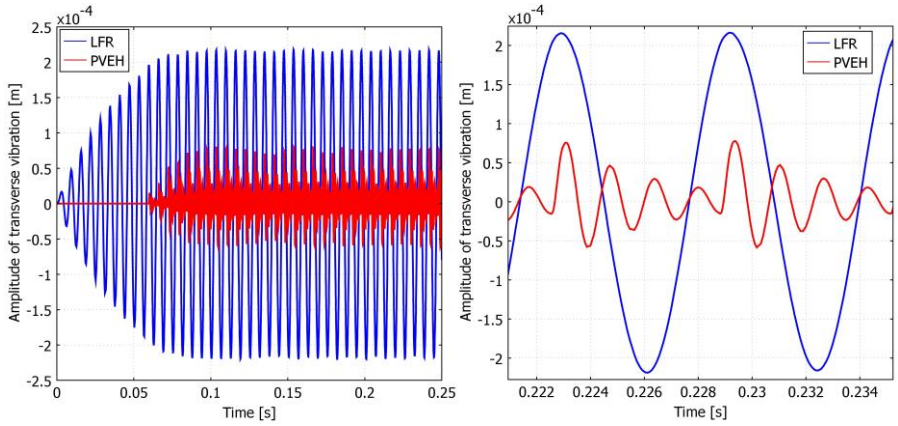

(**c**)

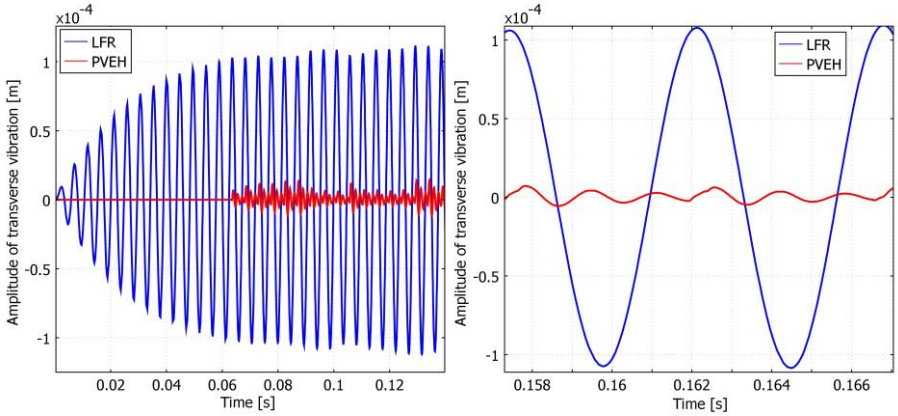

(**d**)

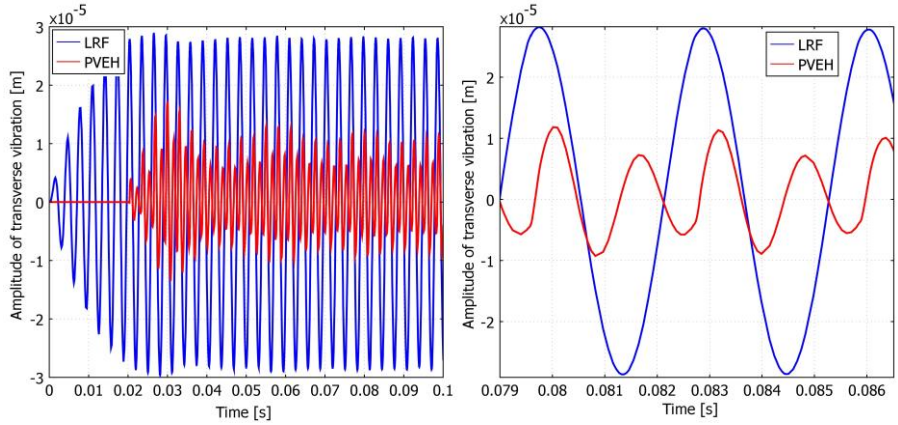

(**e**)

Figure 3.18. Transverse vibrations of LFR (blue) and high frequency PVEH (red) tip point. Contact position L_I^n = 0.5 L of PVEH and natural frequency ratio $\omega_1^{PVEH}/\omega_1^{LFR}$ = (a) 8; (b) 6; (c) 4; (d) 3; (e) 2

Figures 3.8(a-e) depict the vibration of both PVEH and LFR displacement peaks. This can be related to the kinetic energy exchange between the active elements and overlapping of the frequencies, i.e., the higher the frequency ratio, the longer the duration between the pulsation peaks. It is predicted that for higher $\omega_1^{PVEH}/\omega_1^{LFR}$, one could also predict repetitive contacts between the PVEH and the LFR after the impact due to large differences in the natural frequencies. This can be observed very well in Figure 3.18(a) where in the transverse response of the PVEH, after the impact of LFR, the peak of the amplitude is split into two, i.e., a clear result of another impact right after the first one. This bouncing of the PVEH could also lead to an increased energy output, since PVEH would encounter a short burst of impact and relaxation events before being released to fully unbend.

For a better understanding of the processes taking place in PVEH during this type of harmonic and impact induced vibrations, the Discrete Fourier Transform of PVEH tip vibration response signal was performed. The data was processed using MATLAB software.

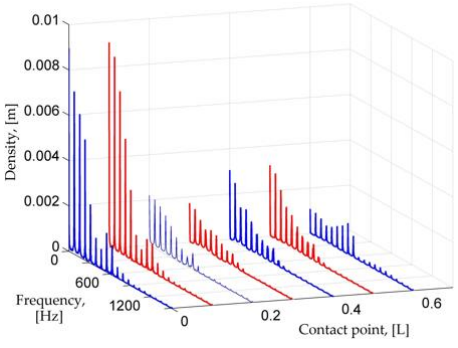

(**a**)

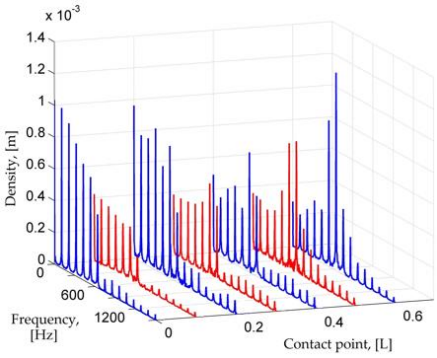

(**b**)

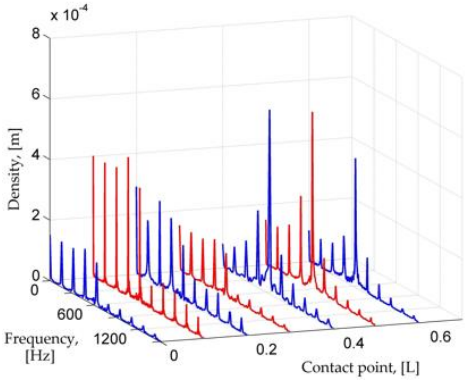

(**c**)

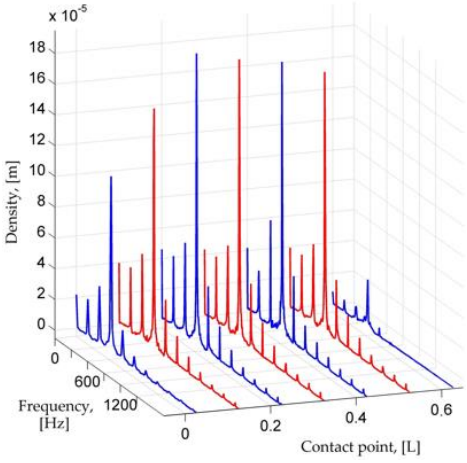

(**d**)

Figure 3.19. Cont.

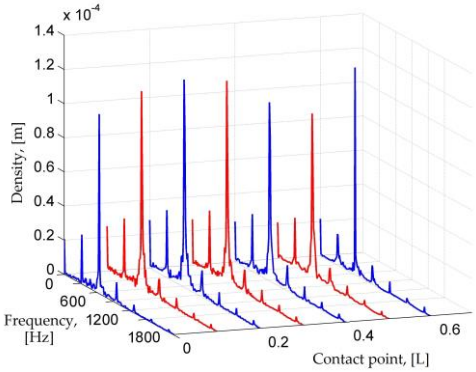

(**e**)

Figure 3.19. DFT of LFR-PVEH tandem at different dynamic contact points and natural frequency ratio $\omega_1^{PVEH}/\omega_1^{LFR}$ = (a) 8; (b) 6; (c) 4; (d) 3; (e) 2

The frequency spectral density obtained from DFT can be seen in Figures 3.19(a-e). The figures were constructed by assembling separately obtained DFT frequency spectra of PVEH tip vibration response data set at different dynamic contact point locations, namely from 0L to 0,6L. Five figures were constructed, each for a different $\omega_1^{PVEH}/\omega_1^{LFR}$ frequency ratio. Each curve has multiple frequency peaks which are equally spaced. This can be explained by the "bounce-off" of PVEH immediately after the initial contact with LFR, and the peaks represent the frequencies of these events. Figure 3.19 shows that fewer frequency peaks are seen in tandem configurations with lower $\omega_1^{PVEH}/\omega_1^{LFR}$ ratio. This confirms the idea that more repetitive contacts observed for tandem configurations with lower $\omega_1^{PVEH}/\omega_1^{LFR}$ ratio will encounter more of these events. From Figure 3.19(a), it can be seen that the frequency spectra peaks are most expressed at low frequency range, roughly where the LFR excitation frequency φ_i is, when the contact location is at the tip of the active element and decreases with contact location shifting towards the fixed end. This can be the result of the distracted LFR. As the PVEH is hit by LFR, the tip of PVEH can vibrate freely without being repeatedly hit by LFR. Hence, the frequency spectra are located around two main peaks, namely the LFR excitation frequency φ_i and PVEH natural frequency ω_1^{PVEH} – 622 Hz. With decreasing $\omega_1^{PVEH}/\omega_1^{LFR}$ ratio, fewer and fewer peaks can be observed, and the frequency gets more and more expressed around the PVEH natural frequency ω_1^{PVEH}. In Figure 3.19(e), the peak at 622 Hz dominates the spectra at all dynamic impact locations. This is mainly due to the fact that after the initial contact PVEH fewer events of repetitive strikes occur.

Electrical properties of PVEH were investigated using the Root-Mean-Square (RMS) values instead of peak values due to the fact that the vibration energy harvester produces alternating power outputs, and it is difficult to estimate the absolute quantities of energy generated as the signal is non-linear. The formula used for this purpose is shown in Equation (3.5):

$$RMS = \sqrt{\frac{\sum_{i=0}^{n} a_i^2}{n}}; \tag{3.5}$$

where a is an array of elements or points in the obtained electrical response curves and n is the number of these elements. PVEH power output curves with different resistive loads R_L connected for each LFR-PVEH tandem configuration and impact point were obtained. The optimal resistive load for all setups was obtained from the steady state analysis and it was found to vary between 28 kΩ and 31 kΩ. The results were obtained by a trial and error method, i.e., by investigating the dynamic responses of the LFR-PVEH tandem with different loads R_L connected. The figures illustrating the RMS power output at different contact point positions and varying resistive load R_L can be seen in Figure 3.20(a–e). The results clearly depict that one can get maximum power output if the contact is located at 0.2 L to 0.3 L from the tip of PVEH. The size of optimal resistance varies with varying contact point position, i.e., a larger resistive load is necessary if the contact point is located closer to the free end of the active element.

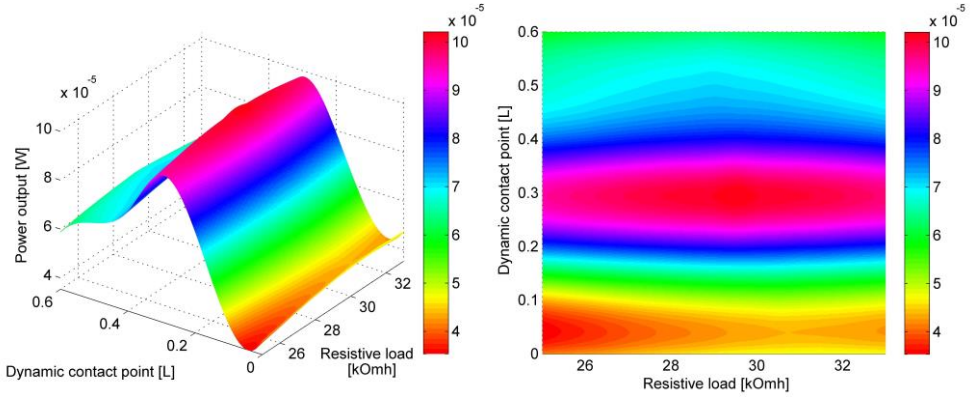

(**a**)

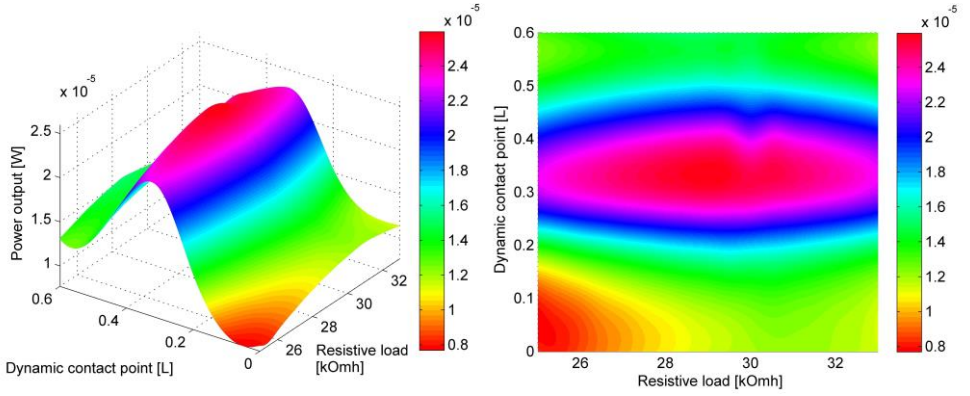

(**b**)

Figure 3.20. *Cont*

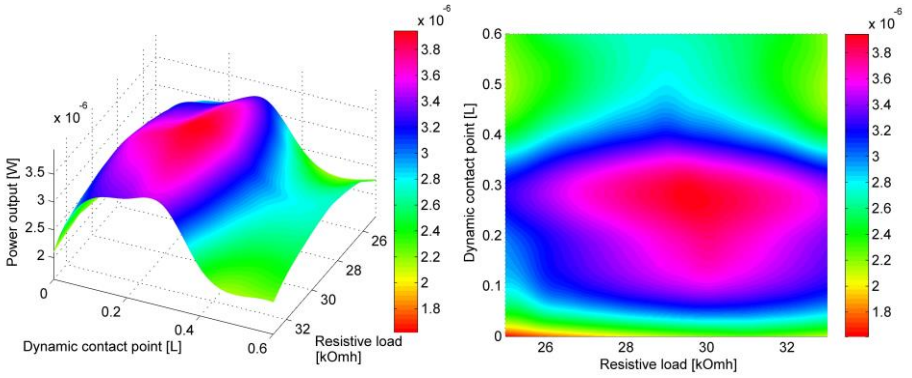

(**c**)

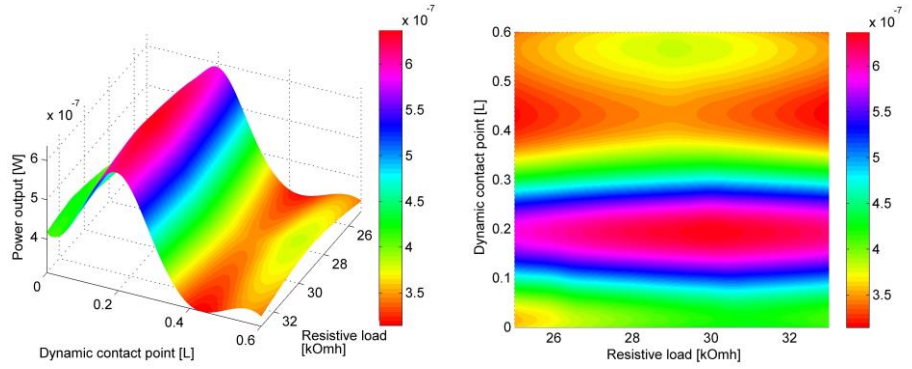

(**d**)

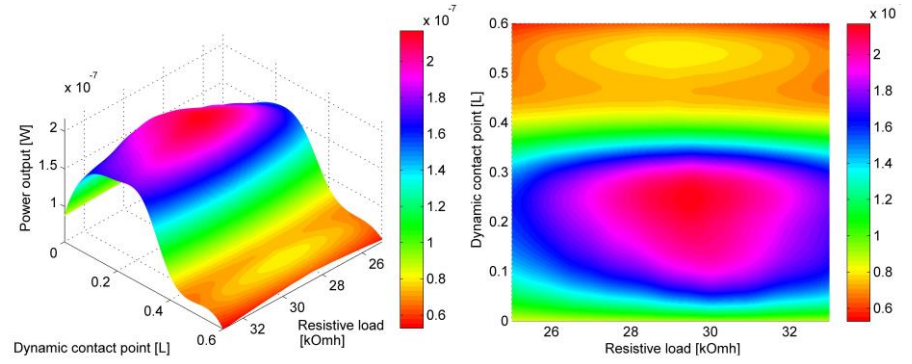

(**e**)

Figure 3.20. RMS Power output of PVEH with different resistive loads and dynamic contact point position. Isometric and top view with natural frequency ratio $\omega_1^{PVEH}/\omega_1^{LFR} =$ (a) 8; (b) 6; (c) 4; (d) 3; (e) 2

The values of resistive loads at which maximum RMS power output was achieved are listed in Table 3.7, and the actual maximum RMS power output values for each configuration are given in Table 3.8. The trend is clear, showing that higher resistive load R_L is needed closer to the free end. From Table 3.7 and Figure 3.20(a–e), it can be seen that the optimal resistive load R_L has highest values when the contact point is at the free end of PVEH (0 L). As the contact point shifts by 0.6 L towards the fixed end, the size of optimal resistive load gradually decreases by ~7%. This is true for all investigated natural frequency ratios. Since for each investigated tandem configuration with the same $\omega_1^{PVEH}/\omega_1^{LFR}$ ratio values such as z_{gap}, excitation frequency and acceleration of LFR were kept constant, a single variable is left to account for change of the size of optimal resistive load size and maximal RMS power output - varying dynamic contact point location.

Table 3.7. Optimal resistive [kΩ] loads for different LRF/PVEH tandem configuration

	$\frac{\omega_1^{PVEH}}{\omega_1^{LFR}}$	**Dynamic Contact Point Position from the Tip of the PVEH active element**						
		0 L	**0.1 L**	**0.2 L**	**0.3 L**	**0.4 L**	**0.5 L**	**0.6 L**
Optimal resistive load R_L, [kΩ]	**8**	31	30.5	29.5	29.5	29	29	29
	6	31	30.5	29.5	29	29	29	28.5
	4	31	30	30	29.5	29	29	28.5
	3	31	30.5	30	30	29	29	28.5
	2	30.5	30	29.5	29.5	29	29	28.5

The difference of the resistive load size for different configurations is comparatively small. It does not exceed 1.5% for the corresponding dynamic impact point of different $\omega_1^{PVEH}/\omega_1^{LFR}$ ratios and 6.5% for different dynamic contact points of the same $\omega_1^{PVEH}/\omega_1^{LFR}$ ratio. The tendency is clear: higher resistive loads are required for tandem configurations with dynamic impact location at the tip of active element. This can be related to increased electrical stiffening of the active element.

PVEH RMS power outputs at different dynamic impact locations and $\omega_1^{PVEH}/\omega_1^{LFR}$ with optimally sized resistive loads from table 3.7 are presented in table 3.8.

Table 3.8. RMS power output [W] of different tandem configurations at optimal resistive loads

	$\frac{\omega_1^{PVEH}}{\omega_1^{LFR}}$	**Dynamic Contact Point Distance from the Tip of the active element**						
		0 L	**0.1 L**	**0.2 L**	**0.3 L**	**0.4 L**	**0.5 L**	**0.6 L**
PVEH RMS Power output, (W)	**8**	4.8×10^{-5}	5.1×10^{-5}	9.2×10^{-5}	1.12×10^{-4}	8.1×10^{-5}	7.1×10^{-5}	6.2×10^{-5}
	6	1.2×10^{-5}	1.3×10^{-5}	2.3×10^{-5}	2.73×10^{-5}	2.2×10^{-5}	1.7×10^{-5}	1.5×10^{-5}
	4	2.2×10^{-6}	3.5×10^{-6}	4.2×10^{-6}	4.51×10^{-6}	3.2×10^{-6}	2.8×10^{-6}	2.7×10^{-6}
	3	4.3×10^{-7}	5.5×10^{-7}	7.9×10^{-7}	8.71×10^{-7}	4.9×10^{-7}	3.6×10^{-7}	3.7×10^{-7}
	2	7.1×10^{-8}	1.1×10^{-7}	1.5×10^{-7}	1.35×10^{-7}	9.3×10^{-8}	7.4×10^{-8}	4.8×10^{-8}

The data shows that the maximum RMS power output is achieved if the contact point is in the interval from 0.2 L to 0.3 L from the tip of PVEH. The data also shows

that the power output is higher for lower LFR ω_1^{LFR} frequencies than for the corresponding impact point locations at higher ω_1^{LFR} frequencies. From Table 3.8, it was calculated that for two-fold natural frequency ratio decrease, the power output increases four to seven times.

From Table 3.8, it can be seen that the contact point at which the maximum RMS power output is obtained is slightly shifting towards the free end of PVEH. For natural frequency ratio $\frac{\omega_1^{PVEH}}{\omega_1^{LFR}} = 2$, maximum power output is obtained at 0.2 L, while for higher natural frequency ratios $\frac{\omega_1^{PVEH}}{\omega_1^{LFR}}$, maximal power output was obtained at 0.3 L. Thus, a conclusion can be drawn that for lower natural frequency ratios, the contact point shall also be located closer to the free end of PVEH. Figure 3.21 illustrates the data given in Table 3.8.

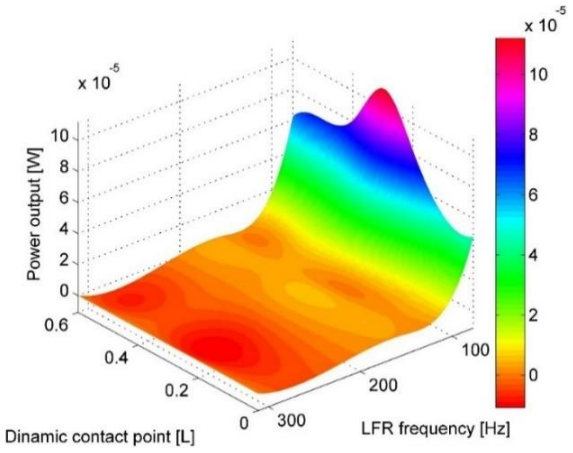

Figure 3.21. RMS power output of different tandem configurations and contact points with optimal resistive load R_L

To compare power outputs obtained at different base excitation frequencies of LFR, an efficiency criterion was invented:

$$P_{eff} = \omega_1^i \times P_n^i \tag{3.6}$$

where P_n^i is RMS power output at the ith ratio of frequencies and the n^{th} position of the impact point at PVEH. The obtained P_{eff} values are given in Table 3.9. A higher power output is obtained from the tandem configuration with a higher $\omega_1^{PVEH}/\omega_1^{LFR}$ ratio even after adapting the efficiency criterion. The difference in frequency only partially accounts for the significant difference between the maximal RMS power output of harvester tandems with different normal frequency ratios $\omega_1^{PVEH}/\omega_1^{LFR}$. After the normalization, the difference between maximal RMS power outputs of tandem configurations with frequency output ratios $\omega_1^{PVEH}/\omega_1^{LFR}$ = 8 and 6 at 0.3 L is 306% (the difference of 410% before normalization), while for $\omega_1^{PVEH}/\omega_1^{LFR}$ = 6 and 4 at 0.3 L the difference is 402% (605% before normalization). This is true for all investigated natural frequency ratios.

Table 3.9. Frequency normalized RMS power output [W] for different tandem configurations at optimal resistive loads

	$\frac{\omega_1^{PVEH}}{\omega_1^{LFR}}$	Dynamic Contact Point Distance from the Tip of the active element						
		0 L	**0.1 L**	**0.2 L**	**0.3 L**	**0.4 L**	**0.5 L**	**0.6 L**
Normalized PVEH RMS Power output	**8**	$3.7\text{x}10^{-3}$	$3.9\text{x}10^{-3}$	$7.1\text{x}10^{-3}$	$8.6\text{x}10^{-3}$	$6.2\text{x}10^{-3}$	$5.5\text{x}10^{-3}$	$4.8\text{x}10^{-3}$
	6	$1.2\text{x}10^{-3}$	$1.3\text{x}10^{-3}$	$2.4\text{x}10^{-3}$	$2.8\text{x}10^{-3}$	$2.2\text{x}10^{-3}$	$1.7\text{x}10^{-3}$	$1.6\text{x}10^{-3}$
	4	$3.5\text{x}10^{-4}$	$5.4\text{x}10^{-4}$	$6.5\text{x}10^{-4}$	$6.9\text{x}10^{-4}$	$4.9\text{x}10^{-4}$	$4.3\text{x}10^{-4}$	$4.2\text{x}10^{-4}$
	3	$8.9\text{x}10^{-5}$	$1.2\text{x}10^{-4}$	$1.6\text{x}10^{-4}$	$1.8\text{x}10^{-4}$	$1.2\text{x}10^{-4}$	$7.5\text{x}10^{-5}$	$7.7\text{x}10^{-5}$
	2	$2.2\text{x}10^{-5}$	$3.5\text{x}10^{-5}$	$4.7\text{x}10^{-5}$	$4.2\text{x}10^{-5}$	$2.9\text{x}10^{-5}$	$2.2\text{x}10^{-5}$	$1.5\text{x}10^{-5}$

To compare the effect of the shifting a dynamic contact point along the length of the active element, a comparison of RMS power output at different positions of dynamic contact points to RMS power output at 0 L position was performed. The results are presented in Table 3.10 and Figure 3.21, with values expressed as percentage difference of RMS power output at a certain contact point in comparison to power output at 0 L point.

Table 3.10. Comparison between tandem power output at different positions of contact point and a contact position at the tip

	$\frac{\omega_1^{PVEH}}{\omega_1^{LFR}}$	Dynamic Contact Point Distance from the Tip of the active element						
		0 L	**0.1 L**	**0.2 L**	**0.3 L**	**0.4 L**	**0.5 L**	**0.6 L**
RMS Power output, (%)	**8**	0	6.2%	91.3%	132.8%	68.6%	47.4%	29.9%
	6	0	7.3%	90.2%	123.8%	79.5%	40.2%	25.4%
	4	0	56%	87.1%	100.4%	41.8%	24.9%	21.3%
	3	0	28.2%	84.7%	102.1%	14.4%	−15.3%	−13%
	2	0	58.3%	146.1%	90.8%	31.4%	−0.6%	−32.5%

The results are also presented graphically in Figure 3.22. The results dictate that for a lower natural frequency ratio (or higher base excitation and LFR natural frequency), the point of maximum power output drifts slightly towards the free end of the active element (0 L).

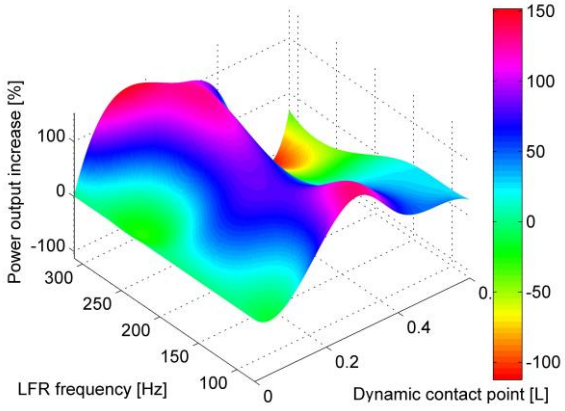

Figure 3.22. Comparison of RMS power output at different contact points with respect to PVEH power output when dynamic contact point is at 0 L

It can also be observed that for natural frequency ratio $\omega_1^{PVEH}/\omega_1^{LFR}$ 6 and 4, higher power outputs are obtained when the contact point is located from 0.2 L and towards the fixed end of PVEH if compared to the power output when the contact point is located at the tip of PVEH. In fact, for the mentioned tandem configurations, the power output from impact at 0 L is the lowest (the power output obtained from impacting at 0.6 L still produces from 20 to 30% higher power output if compared to 0 L). For the frequency ratio $\omega_1^{PVEH}/\omega_1^{LFR}$ 3 and 2, the power output closer to the fixed end (0.5 L and 0.6 L) already produces lower power output if compared to power output at 0 L. This tendency can be related to the amount of kinetic energy supplied by the LFR necessary to deflect the PVEH.

The tendency is clear here, and it suggests that the optimal contact point for different natural frequency ratios is always around 0.2 L to 0.3 L, and the increase in power output achieved there is significant. This can be related to the second transverse vibration mode shape which can be induced if the impact is located at 0.216 L from the tip because at this position the nodal point of the second transversal vibration mode form exists.

3.4. Optimal harvester shape active element analysis.

The goal of the piezoelectric energy harvester active element shape optimization was to maximize the amount of elastic deformation on the upper surface of active element when the active element is subjected to a linear spatial load and with limitations to geometric parameters of the active element (in this case, the thickness of the active element). Maximization of elastic deformations in the upper layer of the active element shall result in increase of voltage, and thus power output as the piezoelectric material layer is attached to that surface. The constraints were introduced on the geometric parameters in order to avoid excessive thinning or thickening of the active element during the optimization procedure. The dynamic equation is converted to a static equation, and optimization is carried out with the static equation in an iterative manner. The method exploits the well-developed static response optimization. A dynamic load is discretized and transformed to multiple static loads and a structure is optimized with multiple loading conditions.

The mathematical formulation of the problem is described in chapter 2.7 of this thesis as shown in equation (2.90 - 2.93). The initial shape of active element is shown in Figure 2.9. The mathematical model was realized in FEM analysis system COMSOL. In the solution, modules of the deformed shape and optimization analysis, were used. A mesh of rectangular elements was used.

An optimal geometry of the active element maximizing elastic deformations in the upper surface while under distributed spatial load is shown in Figure 3.24. The initial boundaries of the active element are shown as a black contour in the Figure 3.24. The optimization procedure finished after 14 iterations.

The developed numerical models were investigated using the modal analysis as described in chapter 2.4 of this thesis. Equation (2.53) describes the equation of the motion, while the eigen frequencies were calculated from equation (2.54). The boundary conditions of an active element fixed in one end are described by equations (2.48) and (2.49).

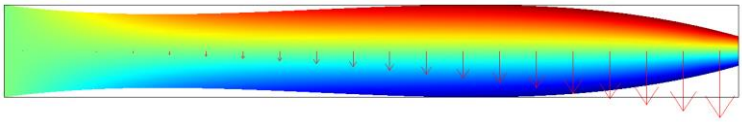

Figure 3.24. Initial and optimal shape of the active element. Normal strain field

The first transient vibration mode shape of the optimized active element is shown in Figure 3.25. The first natural frequency obtained from the modal analysis for the optimally shaped active element was found to be ω_1= 50Hz, while the first natural frequency of the primary constant cross-section active element was ω_1= 66Hz.

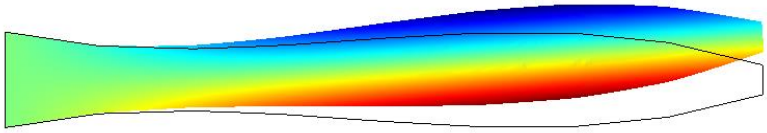

Figure 3.25. First mode shape of optimally shaped active element at ω_1= 50Hz. Normal strain field

The second transient vibration mode shape of the optimized active element is shown in Figure 3.26. The second natural frequency obtained from the modal analysis for the optimally shaped active element was found to be ω_2= 369Hz, while the second natural frequency of the primary constant cross-section active element was ω_2= 389Hz.

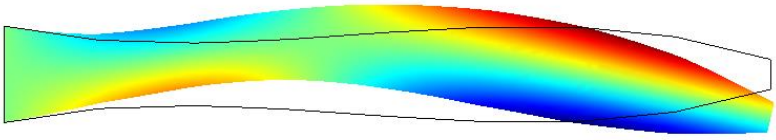

Figure 3.26. Second mode shape of optimally shaped active element at ω_2= 369 Hz. Normal strain field

The transient analysis of the active element was conducted after obtaining the natural frequencies of the investigated active element, with a time varying force f(t) acting on it. The time-dependent force f(t) is described as active element body load in the vertical direction and is defined as the force/volume using the thickness as described in equation (2.56), while the equation of motion is given in equation (2.55) from chapter 2.4. The equation of motion controls the linear dynamic behaviour, and the dynamic response can be found by solving this equation of motion.

The integrated amount of normal strain in the upper surface of the constant cross-section (or sub-optimal) active element for a given interval of time can be seen in Figure 3.27. The integrated amount of normal strain in the upper surface of the optimally shaped active element for a given interval of time can be seen in Figure 3.28.

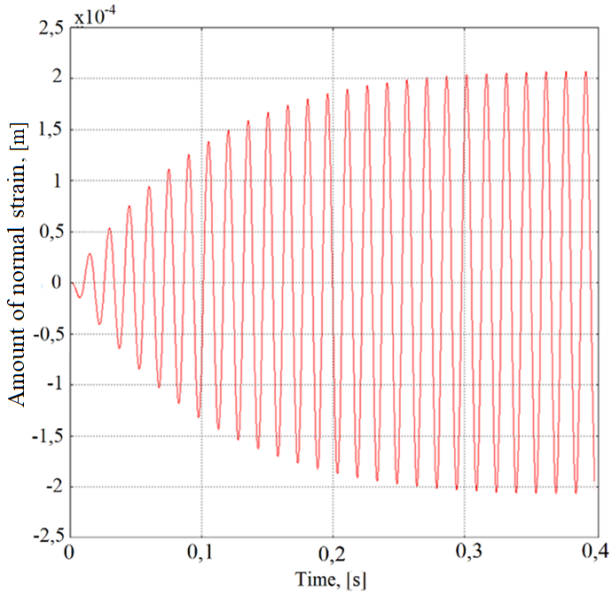

Figure 3.27. Amount of normal strain in the upper surface of the active element versus time. Constant cross-section active element

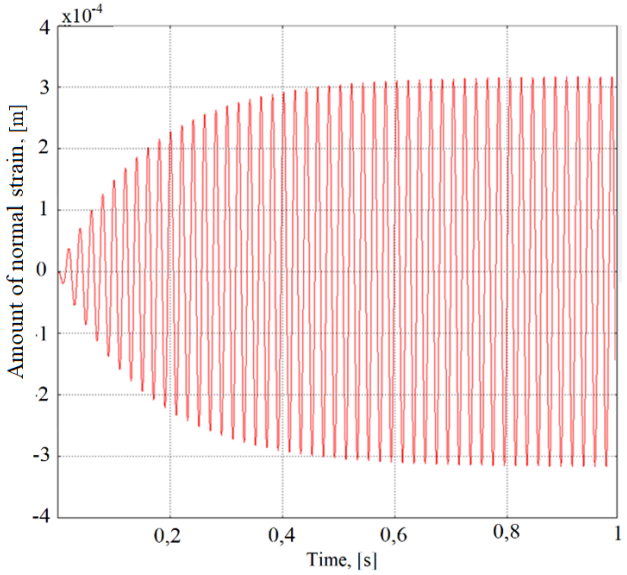

Figure 3.28. Amount of normal strain in the upper surface of the active element versus time. Optimal shape active element.

From Figure 3.27 and Figure 3.28, the peak amount of the normal strain generated by an optimally shaped active element is significantly higher (3.15×10^{-4} *m* in the optimal shape active element versus 2.11×10^{-4} *m* in the constant cross section active element). Each active element was excited by vibrations of frequency matching their first natural frequency and the same acceleration and its parameters. The criteria

of effectiveness (3.7) are derived to properly compare the results obtained at different frequencies.

$$E_{eff} = \omega_1 * \text{Max}\frac{du}{dx}; \quad (3.7)$$

The constant cross-section active element resulted in $E_{eff}^{const} = 135{,}3 \text{ x } 10^{-4}\ m/s$, the optimal shape active element resulted in $E_{eff}^{opt} = 157{,}5 \text{ x } 10^{-4}\ m/s$, and the relative effectiveness calculated using both values is $\frac{E_{eff}^{opt}}{E_{eff}^{opt}} = 1{,}16$.

3.5. Section Conclusions.

Modelling can be considered as one of most important if not most important part of the design of new devices, especially of such a complicated device as an energy harvester. This preliminary design stage gives one the advantages for predicting how elaborated configuration of PEH will perform.

The following FE models have been realized in this section using COMSOL Multiphysics software: i) PVEH dynamic and electric (open circuit) response operating in higher transverse vibration modes (constant cross section active element and optimal shape); ii) PVEH dynamic and electric response operating in higher transverse vibration modes with electrical circuit attached and power output dependency on piezoelectric material layer connection (series or parallel); iii) Low Frequency Resonator (LFR) and PVEH tandem operating in the frequency-up converting mode with dynamic contact, dynamic and electrical response and its dependency on the geometry of LFR, its excitation frequency and electric load size of PVEH; iv) harvester shape optimization.

The numerical simulations and analyses performed throughout the research may be grouped into a few case studies: i) evaluation of PVEH response to the harmonic excitation of the frequency matching its second resonant frequency; ii) evaluation of PEH electrode segmentation on its electric outputs; iii) evaluation of the effects of the electric load connection type (series, parallel) to PVEH generated open circuit voltage; iv) evaluation of the effects of different LFR configurations on PVEH power output when operating in the frequency up converting mode under dynamic impact conditions; vi) evaluation of effect of varying resistive load on PVEH power output when operating in frequency up converting mode under dynamic impact conditions; vii) evaluation the effects of geometric parameters of active elements to the amount of the normal strain produced by it.

The numerical simulation results obtained were further processed using MATLAB software. The main conclusions drawn from numerical simulation results are the following:

- The optimal segmentation point which coincides directly with the normal strain node obtained from the transient analysis was determined for active elements vibrating in their second transverse vibration mode. The two setups of a harvester were investigated: constant cross-section area and optimal shape active elements. 7.2% increase in the generated normal strain was achieved for

optimal shape active element and 6% for constant cross-section area active element.

- The coupled piezoelectric-circuit finite element model (CPC-FEM) with an attached electrical load was used to verify the theoretical calculations of the optimal resistive load, and it is obvious that the resistive load varies significantly for parallel (127 kΩ) and series (29 kΩ) connected piezoelectric material layers. The size of theoretically calculated optimal resistive load found from FEM simulation complies well with numerical simulation results.
- The CPC-FEM and mathematical models were created of a non-linear, frequency-up converting, piezoelectric energy harvesting tandem that consists of a low frequency resonator (LFR) and a high frequency piezoelectric energy harvester (PVEH). The CPC-FEM model was realized using COMSOL software. Different configurations with varying $\omega_1^{PVEH}/\omega_1^{LFR}$ ratio of the tandem and different dynamic impact points that were moved from the free end of PVEH towards the fixed end by 0.6L. It was determined that the maximal power output is obtained when the $\omega_1^{PVEH}/\omega_1^{LFR}$ ratio is 8 and the dynamic impact point is roughly at 0.2L distance from the tip of PVEH. This configuration produces up to 146% higher power output than the configuration with impact point location at the tip of PVEH (0L).
- The shape of a simple active element energy harvester was optimized with the goal to maximize the amount of elastic deformation on the upper surface of the active element when the active element is subjected to a spatial load and with limitations to the geometric parameters of the active element (in this case, the thickness of the active element). The transient analysis of the obtained optimal shape active element and the sub-optimal shape active element revealed that, after the optimization, the peak output of the normal strain was increased by 49% and, after adopting the criterion of effectiveness, the increase of the normal output was 16%.

4. EXPERIMENTAL VERIFICATION.

The following section describes the steps of PVEH prototype development, manufacturing and testing as well as the customized equipment and stands used for the experimental measurements and the experimental studies with different configuration PVEH prototypes performed throughout the research period. The aim of the experimental studies was to evaluate the dynamic and electric characteristics of the harvester prototypes and verify the adequacy of the developed FE model.

The PVDF specimens were created using laser cutting technology and were manufactured in the Centre for Physical Sciences and Technology (Vilnius). The specimens were then used for manufacturing of PVEH operating at higher transverse vibration modes, and two geometries of active elements were tested. Optimally shaped (shape obtained from solving volume minimization problem with constrains for eigen frequencies) and rectangular (water jet cutting was used for manufacturing the active elements) cantilevers were used for the experiment. The aim of the experiment was to test the newly developed numerical methodology to calculate the accurate strain node location for such devices, and thus optimal segmentation points for the piezoelectric material. The holography technique was used to test the mode shapes and eigen frequencies of the active elements obtained from modal analysis.

The second experiment was conducted in order to test the developed model of the LFR and PVEH energy harvesting tandem utilizing frequency up conversion and the developed dynamic contact model. The specimens of the active elements used for this experiment were manufactured using water jet cutting technique. PZT was used as a piezoelectric material. A simple electrical circuit consisting of a resistive load was attached to the PVEH in order to obtain the power output of the developed harvester.

4.1. Piezoelectric material cutting for segmentation: methodology, parameters and characteristics of used equipment and materials.

This section briefly describes the manufacturing process of the PVDF specimens used for the first experiment. A picosecond laser PL10100 (Ekspla) was used for the manufacturing (laser cutting) of the piezoelectric material specimens (fundamental and second harmonics). The laser plates were guided using galvanometric scanners (ScanLab). The parameters of the laser system are given in Table 4.1.

Table 4.1 Parameters of the laser system

Laser	**PL10100, Ekspla**	
Wave length	1064 nm	532 nm
Duration of impulse	10 ps	
Repeating frequency	50 - 100 kHz	
Maximum power	5,2 W @ 100 kHz	2,1 W @ 50 kHz
Galvanometric scanner	**SCANgine 14**	**HurrySCAN 14**
F-theta lens focus distance	80 mm	80 mm
Telescope	4x	-
Laser beam width before the scanner ($1/e^2$ level)	6,38 mm	2,16 mm
Width of the focused laser beam ($2w_0$)	20,7 μm	20,6 μm

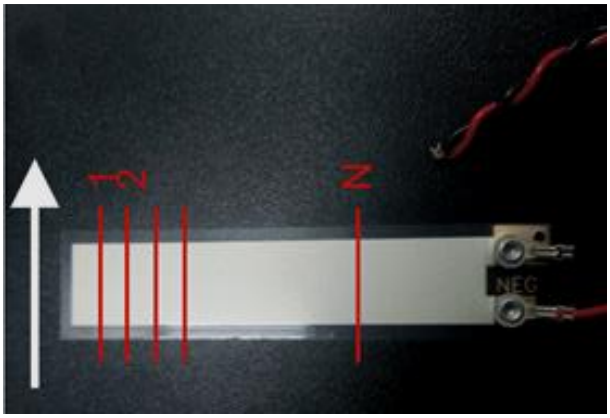

Figure 4.1. PVDF specimen used for laser cutting

PVDF was used for manufacturing of the experimental specimens, namely DT1-028K by the Measurement Specialties Inc., Hampton. Rectangular, piezo film, silver electrode covered elements were used. The lead attachment was accomplished by using a riveted lug going to 12" (300 mm) of 28 AWG wire, as shown in Figure 4.1.

The PVDF was cut by scanning the lines and changing the laser power output, the impulse energy, the scanning speed and the number of scans. After each cut, the resistance between the positive and negative electrodes of the PVDF specimen was measured using a multimeter (Mastech MS8268). In this way, it was measured if a short circuit between the electrodes was created during the cutting procedure. The PVDF was cut from in the direction shown in Figure 4.2 since the laminate was thinner on that side as shown in Figure 4.3.

Figure 4.2. 532 nm, "1" cut of the PVDF specimen

Figure 4.3. 532 nm, "N" cut of the PVDF specimen

When cut with the 1064 nm wavelength beam, the PVDF was positioned on a glass surface. After the cut, the ends of the PVDF specimens were separated mechanically if the number of scans was insufficient. When cut with the 532 nm wavelength beam, the PVDF specimen was positioned in the air in every case and no mechanical separation was necessary.

4.2. Segmentation investigation: preparation of harvester model, scheme, stands, parameters of used equipment and materials.

Open circuit voltage output experiment

The aim of the first experiment was to verify the FEM model of the piezoelectric vibration energy harvester operating in higher transverse vibration modes with two PVDF segments attached. Four different setups of active elements were investigated, i.e., two optimal shape active elements, one of which was segmented at the segmentation line obtained from modal analysis (0,239L) and one segmented at the segmentation line obtained from transient analysis (0,259L) and two constant resection active elements, one of which was segmented at the segmentation line obtained from modal analysis (0,216L) and one segmented at the segmentation line obtained from transient analysis (0,238L).

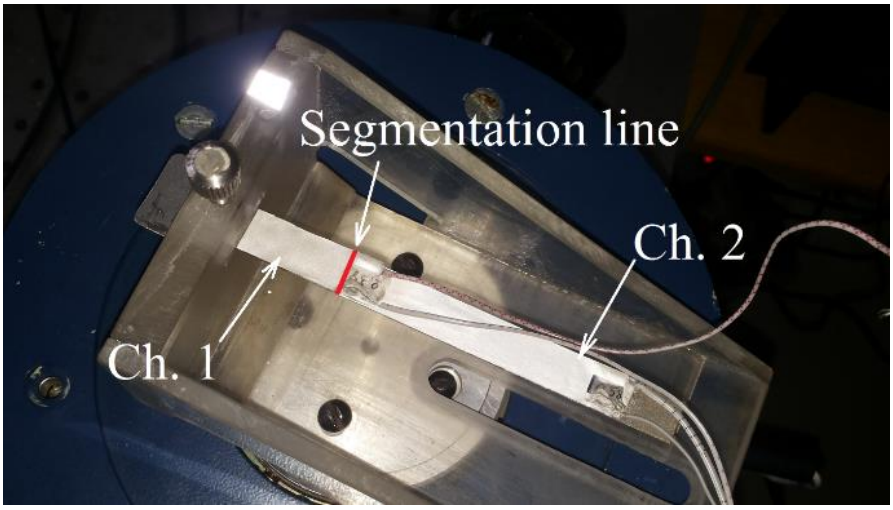

Figure 4.4. Experimental setup of the tested piezoelectric vibration energy harvester

The objectives set to reach this aim were as follows: to manufacture active elements that would be the same as modelled in the FEM model, to produce a reasonable test stand and to test their response to the harmonic excitation of the same frequency that is used in the FEM model. The obtained open circuit voltage output results then had to be compared to the ones obtained theoretically.

To verify the modelling results, the open-circuit voltage output from constant cross-section area and optimal shape active elements were compared with experimental results obtained from an experiment conducted using experimental stand shown in Figure 4.4. The scheme of the experiment is depicted in Figure 4.5.

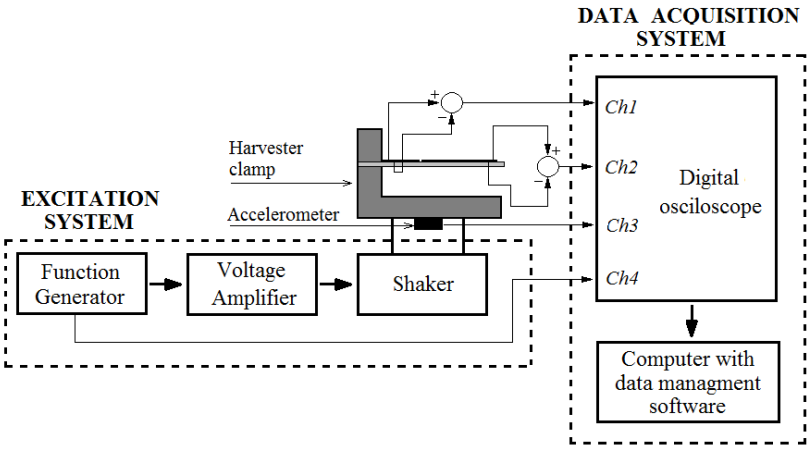

Figure 4.5. Scheme of the experimental setup

This experimental setup is composed of two main systems. The first one is the data acquisition system with the purpose to record the vibration response of the active element and record the open-circuit voltage outputs of both piezoelectric segments. The second system is an excitation system that consists of a signal generation system and an electromechanical shaker witch directly excites the energy harvester in a desired frequency since the harvester clamp is directly mounted on the top of the shaker. The substrate layer of the PVEH (with final harvester dimensions of 100 × 10 × 1 mm) is made of water-jet cut structural steel; and two PVDF layers (transducers DT1-028K by Measurement Specialties Inc., Hampton, VA, United States) are mounted on top. The function generator AGILENT 33220A is used to control the harmonic excitation signal transmitted to the electromagnetic shaker. The single-axis miniature piezoelectric charge-mode accelerometer METRA KS-93 (with a sensitivity of k = 5 mV/(m/s^2)) is attached at the bottom of the electromagnetic shaker for acceleration measurements. A constant 1.3 g acceleration was maintained.

The experimental results for the constant cross-section area active element are given in Figure 4.6. Open circuit voltage outputs for both left (Channel 1 from Figure 4.5) and right (Channel 2 from Figure 4.5) elements are shown in Figures 4.6(a) and 4.6(b), respectively. The blue line represents the “optimal” configuration which corresponds to the segmentation results corresponding to the segmentation in the segmentation line (strain node) obtained from transient analysis as described in chapter 3.1 of this thesis. The red line indicates the “sub-optimal” segmentation results corresponding to the segmentation in the segmentation line (strain node) obtained from modal analysis. The excitation frequency for the constant cross-section area active element was 551 Hz.

Open circuit voltage output peak at Channel 1 is 0.287 V for optimal segmentation and 0.264 V for the suboptimal segmentation (8.7% difference). Channel 2 produced 0.389 V for the optimal segmentation and 0.351 V for the suboptimal segmentation (10.2% difference).

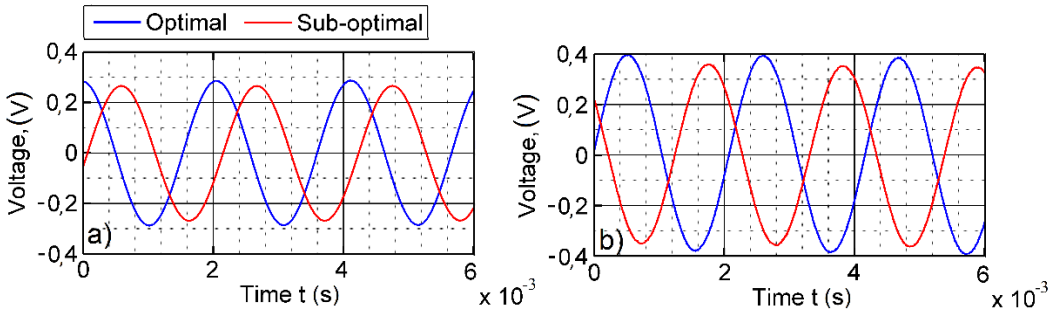

Figure 4.6. Open circuit voltage output for the active element of a constant cross-section (ω_2 = 551 Hz): (a) first segment; (b) second segment

Figure 4.7 provides the corresponding results for the optimally-shaped active element excited at its second natural frequency of 545 Hz. Open circuit voltage output peak at Channel 1 is 0.275 V for the optimal segmentation and 0.261 V for the suboptimal segmentation (5.1% difference). Open circuit voltage output peak Channel 2 was 0.369 V for the optimal segmentation and 0.353 V for the suboptimal segmentation (4.6% difference).

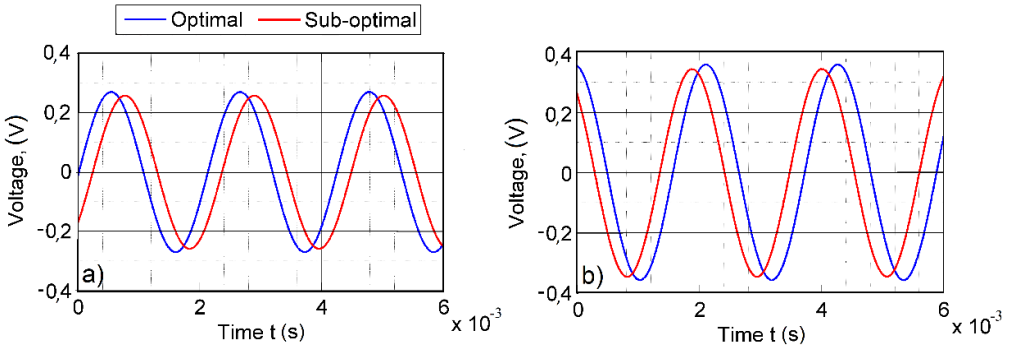

Figure 4.7. Open-circuit voltage output of the optimally-shaped active element at ω_2 = 545 Hz:
(a) first segment; (b) second segment

The results dictate that the peak open circuit voltage output for the optimally shaped active element were approximately 3.5% lower if compared to the constant-cross section area active element open circuit voltage output amplitude. These results comply well with the results shown in table 3.3.

In Figure 4.8, the comparison of open circuit voltage outputs obtained experimentally and retrieved from simulations is presented. The dotted lines here represent the theoretical results while the continuous ones represent the experimental results. The results dictate that in every case, the theoretical predictions for the voltage output have a good agreement with the experimentally-obtained voltage values.

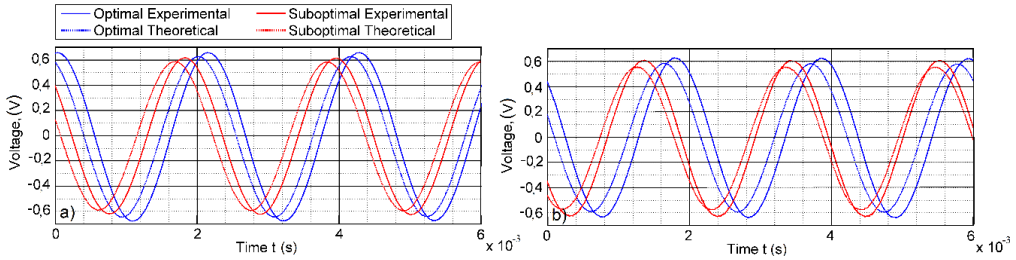

Figure 4.8. Experimental and theoretical outputs of total open-circuit voltage (first segment + second segment): (a) active element of a constant cross-section; (b) optimally-shaped active element

The results show that the largest voltage amplitude was generated by the optimal constant cross-section area active element (segmentation line at 0.0238 m): 0.676 V, while the sub-optimal counterpart (segmentation line at 0.022 m) generated 0.615 V, which is 9.9% less. The optimally-shaped active element with optimal segmentation (segmentation line at 0.026 m) generated 0.536 V, while sub-optimal counterpart (segmentation line at 0.024 m) generated 0.511 V, which is 4.8% less. The theoretical and modelling results show a good agreement, and the error does not exceed 5% for all investigated cases.

PRISM Holography experiment

The aim of this experiment was to verify the FEM model of the active element vibrating in higher transverse modes. To achieve this aim, several objectives had to be fulfilled: the transient vibrations eigen frequencies obtained from the modal analysis had to be confirmed experimentally, and higher transverse vibration mode shapes obtained from modelling had to be verified experimentally. To achieve this aim and objectives, the holographic interferometry was chosen.

To verify the developed model, experiments were conducted. The model was verified by experimentally measuring the vibration amplitudes in the y-direction of the rectangular and optimal shape active element when excited by their first and second natural frequencies of transverse vibrations. The active elements used were described in the previous section. The technique of holography was used for this purpose. The experimental setup can be seen in Figure 4.9(a).

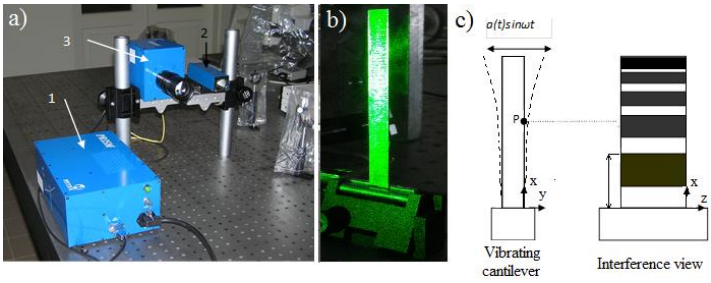

Figure 4.9. a) The PRISM holography system: 1 – control block; 2 – object beam source; 3 – camera; b) The rectangular active element specimen c) Interferometric view of vibrating active element

The displacement in the y-direction between each pair of adjacent parallel dark lines can be found from the Bessel function. Holography is lensless photography in which an image is captured as an interference pattern as shown in Figure 4.9(c). The active element specimen can be seen in Figure 4.9(b).

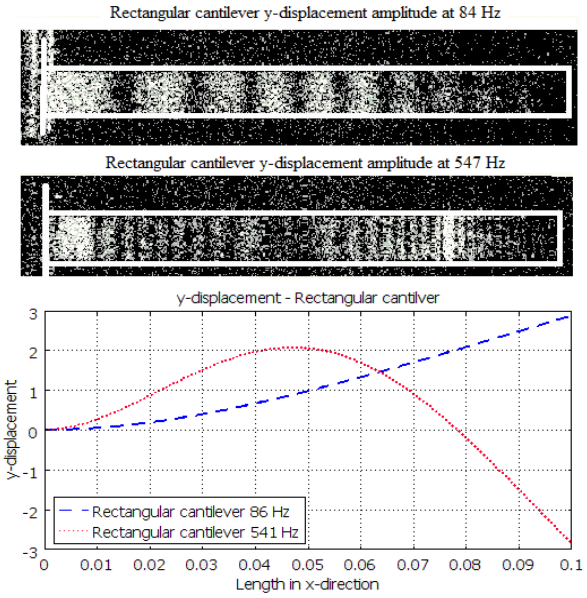

Figure 4.10. Holographic image of active element's face vibration amplitudes and first/second mode shapes from modal analysis of Rectangular active element

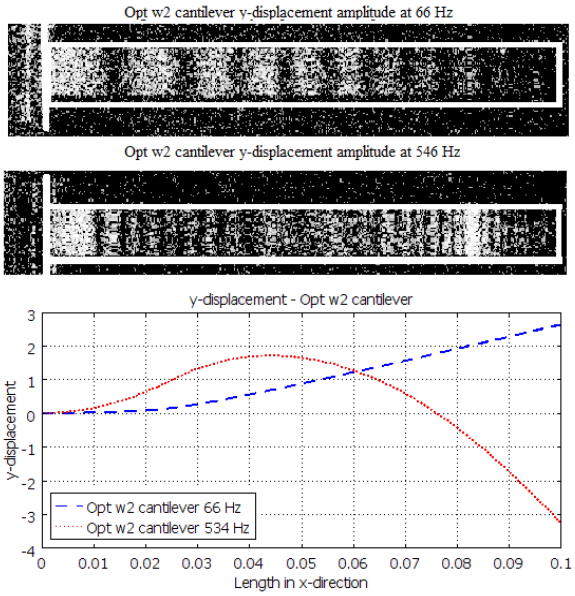

Figure 4.11. Holographic image of active element's face vibration amplitudes and first/second mode shapes from modal analysis of optimal shape active element

The vibration amplitudes obtained from the holographic images are compared with those obtained from COMSOL multiphysics as shown in Figure 4.10 for rectangular active element and Figure 4.11 for optimal shape active element. The bright white lines in the holographic images of active elements excited in their second resonant frequencies represent the amplitude minimum or nodal points where the vibration amplitude is 0 m, while the dark region represents the maximums of amplitude. These nodal points coincide with vibration minimums of the mode shapes obtained from the numerical modal analysis. Resonant frequencies of rectangular and optimal shape active elements obtained experimentally and from modal analysis are compared. The results indicate that the deviation is very small and within the tolerance of 3%.

4.3. Vibro-shock system. Equipment, scheme, methodology and results.

For experimental verification of the derived FEM model of the frequency-up converting tandem, a prototype system was fabricated. Its schematic representation can be seen in Figure 4.12.

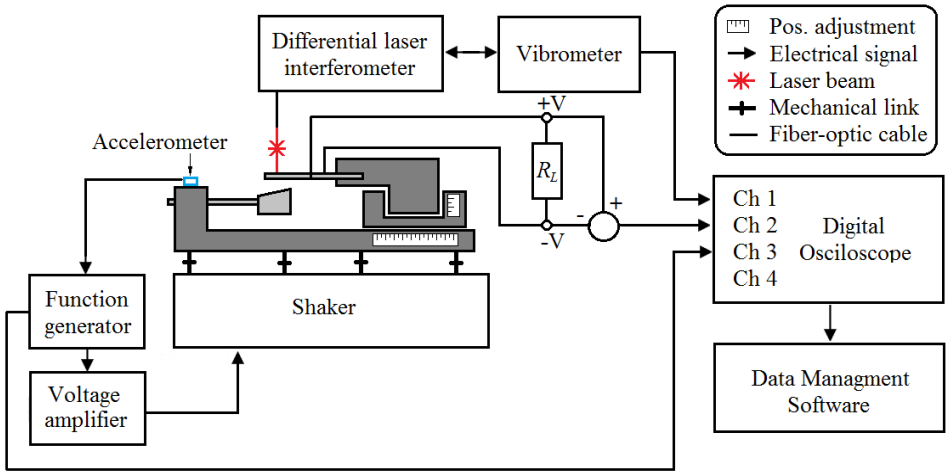

Figure 4.12. Schematic representation of experimental setup

LFR was manufactured from a structural steel. An additional weight, that is proof mass, was added to the tip of the active element. PVEH was manufactured from a stainless steel with a bulk PZT-5H layer attached on the top by using dry adhesives. LFR was suspended below the PVEH so that the mechanical contact occurred only between the LFR proof mass and PVEH load bearing structure. PVEH tip displacement was measured with a Doppler Vibrometer (OFV-512 differential laser interferometer, Polytec, Waldbronn, Germany) with a Polytec OFV-5000 controller (Polytec, Waldbronn, Germany) connected to it. An acrylic glass support and clamp structure with both active elements (LFR and PVEH) fixed was mounted on to an electromagnetic shaker, which was controlled by a 33220A function generator (Keysight, Santa Clara, USA), and the VPA2100MN voltage amplifier (HQ Power, Gavere, Belgium) was used to amplify the signal. LFR position on the stand was fixed,

while the PVEH was mounted onto a movable clamp structure, which allowed to adjust the gap distance and the dynamic contact point location. Excitation amplitudes were measured using a single axis accelerometer (KS-93, sensitivity 0.35 mV(m/s^2)). Readings from both accelerometer and resistive load attached were recorded using 3425 USB oscilloscope. The experimental setup can be seen in Figure 4.13.

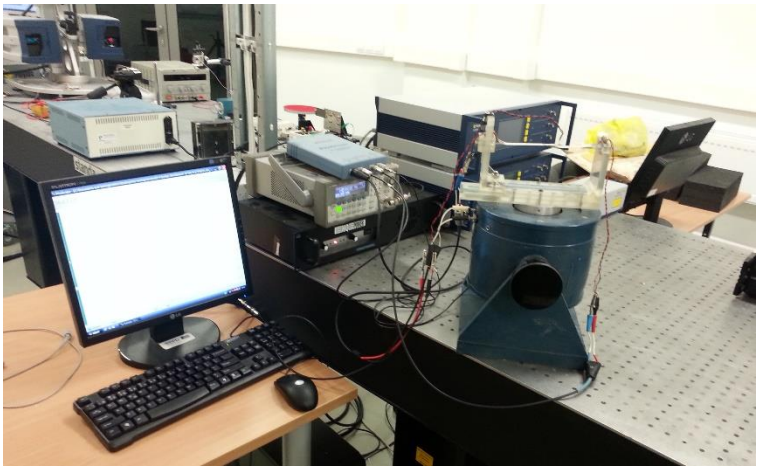

Figure 4.13. Experimental setup

During the first experiment, PVEH dynamic response under open circuit conditions (RL = 10 MΩ was measured under 77 Hz base excitation frequency and $\omega_1^{PVEH}/\omega_1^{LFR}$ = 8 tandem configurations inducing 622 Hz PVEH resonant vibrations). As explained in section 3.3, this is the manifestation of frequency-up conversion phenomena. An experimental voltage-time dependence was obtained (depicted in Figure 4.14).

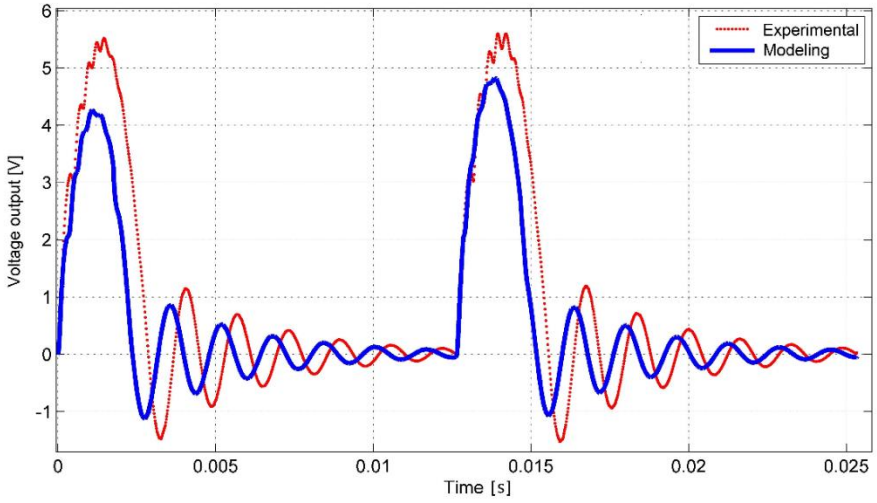

Figure 4.14. Experimental vs. modelling obtained open circuit voltage output of PVEH under dynamic excitation by 77 Hz LFR at 0.2 L dynamic impact contact point

The time interval of 0.025 seconds is shown in Figure 4.14. It depicts two full periods of LFR, which results in two mechanical impact coupling events of PVEH. The transient process shown was "cut" from a steady state vibration region. Between the impacts, a decaying PVEH signal can be observed with multiple signal "ripples" during the contact. This can be explained by the repetitive bouncing of PVEH. The experimental and modelling results comply well with the modelling results, and the difference of both signals does not exceed 8%. From the experimental curve, it can also be seen that higher transverse vibration modes are induced in PVEH during the impact. The duration of the impact was a little longer in the experimental mode, which is due to a possible difference of LFR excitation frequency and/or the damping parameters. Overall, the model shows a good agreement with the experimental data.

Figure 4.15(a) presents a comparison of modelling and experimentally obtained peak of the harvested power as a function of load resistance under highly nonlinear vibro-shock inputs to the transducer. The experiment was done using these parameter values: contact position—0.2 L, natural frequency ratio $\omega_1^{PVEH}/\omega_1^{LFR} = 8$.

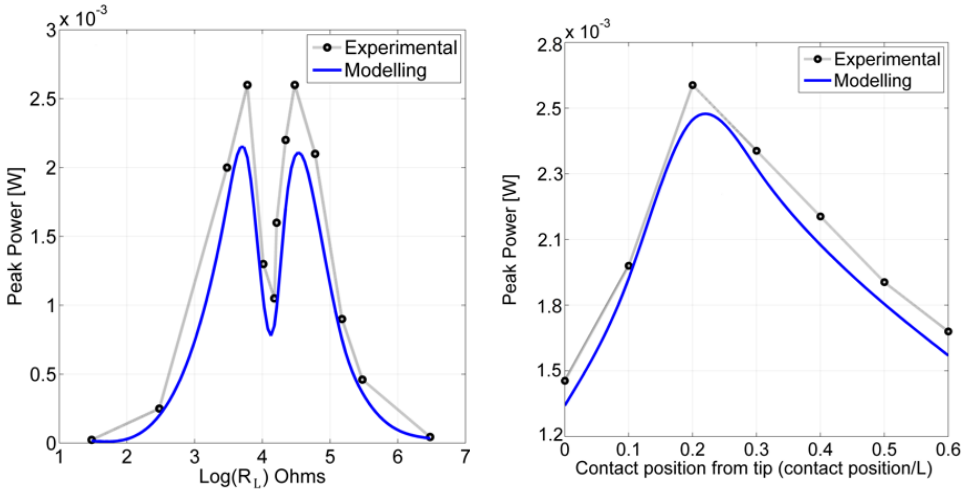

(**a**) (**b**)

Figure 4.15. Experimental and modeling maximum of harvested power output as a function of: (a) load resistance under sinusoidal and impact excitation, contact position—0.2 L, natural frequency ratio $\omega_1^{PVEH}/\omega_1^{LFR} = 8$; (b) contact position at natural frequency ratio $\omega_1^{PVEH}/\omega_1^{LFR} = 8$, resistive load attached R_L = 29.5 kΩ

The resistive load values in Figure 4.15(a) are presented in a logarithmic scale, two peaks represents optimal resistive load values - ~6.5 kΩ and ~31 kΩ which is due to electrical resonance and anti-resonance effect as expected for piezoelectric material with high electromechanical coupling coefficient. The modelling results show a good agreement with the experimental results. This clear gap in peak power output as a function of resistive load could be explained by sinusoidal and impact driven vibrations. The results show that experimentally obtained values were approximately 5% higher than the results obtained from modelling.

Figure 4.15(b) depicts the relationship between the experimental and modelled power output as a function of dynamic contact location along the length of PVEH with a resistive load R_L = 29.5 kΩ. The experimental and modelling results show a good agreement, and the error does not exceed 6%. In both cases, the peak power output is generated when the dynamic contact location is at 0.2L. The experiment was done using these parameter values: natural frequency ratio $\omega_1^{PVEH}/\omega_1^{LFR} = 8$, resistive load attached R_L = 29.5 kΩ.

Peak power outputs with an optimal resistive load attached are in a good agreement with the RMS power outputs presented in Table 3.9 and Figure 3.21, matching both the dynamic contact point location at which the highest power and the highest amount of power output were generated (0.2-0.3L).

4.4. Section conclusions.

Theoretically obtained results can only be deemed correct if verified experimentally. This was done by conducting several experiments for verification of previously developed mathematical and FE models and numerical simulations done in accordance to them. The main conclusions drawn from the experiment with a PVEH operating at higher vibration modes are following:

- The coupled model of PVEH operating at higher transverse vibration modes with two segments of piezoelectric material attached was experimentally verified with a quite good agreement of 7%. The open circuit voltage obtained theoretically from the model was compared to the experimentally obtained values from the experiment with a vibro stand. The theoretically obtained eigen frequencies and mode shapes were compared to the results obtained from the experiment using the holography technique, and the error does not exceed 3%.
- The methodology developed to calculate the exact location of the strain node using transient analysis and its superiority over the strain node obtained from modal analysis to be used as a segmentation point of piezoelectric elements for PVEH operating in the second transverse vibration mode was confirmed experimentally. PVEH segmented in the strain node obtained from transient analysis generated 7.2% higher open circuit voltage output for the constant-cross section area active element and 6% for the optimally shaped active element. The error between the modelling and experimental results does not exceed 5% in any investigated case.
- The model shows a good agreement with the experimental results and, therefore, is deemed valid.

The main conclusions drawn from the experiment with an energy harvesting tandem consisting of PVEH and LFR are following:

- The experimental investigation of PVEH dynamic response under open circuit conditions (RL = 10 MΩ) at 77 Hz base excitation frequency and $\omega_1^{PVEH}/\omega_1^{LFR}$ = 8 tandem configurations were conducted. The experimental and modelling results comply well with the numerical modelling results, and the difference of both signals does not exceed 8%.

- A comparison of modelling and experimentally obtained peak of the harvested power as a function of load resistance under highly nonlinear vibro-shock inputs to the transducer with tandem configuration of contact position 0.2 L, natural frequency ratio $\omega_1^{PVEH}/\omega_1^{LFR} = 8$ was conducted. The obtained optimal resistive values were ~6.5 kΩ and ~31 kΩ, which is due to electrical resonance and anti-resonance which manifests in materials with a high electromechanical coupling coefficient. The results show that the experimentally obtained values were approximately 5% higher than the results obtained from modelling.
- The relationship between the experimental and modelled power output as a function of dynamic contact location along the length of PVEH with a resistive load RL = 29.5 kΩ was determined. The experimental and modelling results show a good agreement, and the error does not exceed 6%. In both cases, the peak power output is generated when the dynamic contact location is at 0.2L. The experiment was done using these parameter values: natural frequency ratio $\omega_1^{PVEH}/\omega_1^{LFR} = 8$, resistive load attached RL = 29.5 kΩ.
- The model shows a good agreement with the experimental results and, therefore, is deemed valid.

5. GENEREAL CONCLUSIONS.

1. A novel methodology was developed for optimal harvesting of the energy generated from a piezoelectric material operating at higher vibration modes. The distribution of the normal strain in the piezoelectric material layer was investigated using transient analysis. Using the developed methodology and numerical results of the normal strain distribution, the normal strain nodal point was calculated for the harvester operating at the second transverse vibration mode, ensuring a 5.2% and 5.5% increase in the harvested energy for constant cross-section and optimal shape active elements, respectively, if compared to the results obtained when segmenting the active element at the normal strain nodal point obtained from modal results.
2. The mathematical and numerical models of nonlinear dynamic contact of piezoelectric vibration energy harvester elements were created. The developed models were used for the investigation of harvester's physical behaviour under kinematic and vibro-impact excitation.
3. The coupled model of the piezoelectric device with an electrical load attached was developed. The eligibility of the models for practical calculations of the dynamical and electrical properties of the piezoelectric elements connected in parallel and series was checked, and the modelling results were investigated by using the numerical methods. The size of the optimal resistive load needed for the series connection is 77% lower than those needed for the parallel connection, even though the power output is similar.
4. The mechanical and electrical parameters of the nonlinear dynamic contact between different piezoelectric elements maximizing the energy output of such devices were determined. Using the developed FE model of the low frequency resonator (LFR) and piezoelectric vibration energy harvester (PVEH), it was found that the transducer is the most efficient when the location of the dynamic impact point is at $0{,}2 - 0{,}3$ L distance from the tip of the active element. This allows up to 150% greater RMS power output if compared to LFR impacting to the tip of PVEH (0L). This might be explained by stating that the location of the dynamic contact roughly coincides with the location of the displacement node point for the second mode shape of the active element generating higher mode shapes which generate significantly higher amount of strain, and thus more energy.
5. The mathematical and numerical models of the shape optimization problem, maximizing the amount of the generated normal strain, were developed. By solving the shape optimization, the peak output of the normal strain was increased by 49% of the active harvester's element and after adopting the criterion of effectiveness normalizing the amount of the normal strain with respect to excitation frequency, the increase of normal output was 16% if compared to the energy output from a constant cross-section active element.
6. The methodologies and experimental stands were developed for the experimental verification of the described mathematical and numerical

models. After conducting the experiments, the following conclusions can be drawn:

i. The methodology for calculation of the normal strain nodal point was checked experimentally. It was experimentally determined that a harvester segmented at the strain nodal point obtained from the transient analysis generated 5.5% higher voltage output in comparison to the voltage output obtained from the harvester segmented at the nodal point obtained from the modal analysis.

ii. The effect of the size and location of the electrical load of the dynamic contact on the amount of power generated by the tandem was experimentally investigated and proven to be in a good agreement with the modelling results as the error does not exceed 8%. The best results were obtained when the location of the dynamic contact coincided with the displacement nodal point of the second transverse vibration mode.

iii. The relation between the frequency ratio of LFR and PVEH natural frequency ω_1^P/ω_1^{LF} and the power generated by the tandem was experimentally determined. The best results were obtained when the frequency ratio $\omega_1^P/\omega_1^{LFR}$ was equal to 8. It can be explained by the fact that the higher the amount of energy the LFR is carrying, the more of that energy can be usefully transferred into the piezoelectric generator.

REFERENCES

1. *World Energy Resources 2013 Survey,* [Last viewed 2017-05-22]. Access via internet: www.worldenergy.org, World Energy Council.
2. ZADEH, Mohsen S. *Measurement of ion mobility in dielectric liquids*, Diploma work in the Master Program Electric Power Engineering, Diploma work No. 66/2011.
3. KETILSSON, J., M. GUDMUNDSDOTTIR. 2016 *Iceland Country Report,* Wairakei Research Centre, Reykjavik, Iceland. 2017.
4. DONOVAN, J. (2016), *New applications for Energy Harvesting*, [Last viewed 2017-05-22]. Access via internet: https://eu.mouser.com/applications/energy-harvesting-new-applications/
5. BEEPY, S., N. WHITE. Energy harvesting for autonomous systems, *IEEE Industrial Electronics Magazine*, March 2012, Volume: 6, Issue: 1.
6. OSTASEVICIUS, V., G. JANUSAS, A. PALEVICIUS, R. GAIDYS, V. JURENAS. *Biomechanical Microsystems: Design, Processing and Applications*. Springer, 2017. ISBN 978-3-319-54849-4.
7. KNIGHT, C., S. BEHRENS, J. DAVIDSON. Review Energy Options for Wireless Sensor Nodes. *Sensors.* 2008, 8(12), pp. 8037-8066. doi:10.3390/s8128037.
8. ZHU, D. Vibration Energy Harvesting: Machinery Vibration, Human Movement and Flow Induced Vibration. *Sustainable Energy Harvesting Technologies - Past, Present and Future*. INTECH, 2011. pp. 25-54. DOI: 10.5772/25731
9. DESPESSE, G., T. JAGER, J. CHAILLOUT, J. LEGER, A. VASSILEV, S. BASROUR and B. CHALOT. Fabrication and characterisation of high damping electrostatic micro devices for vibration energy scavenging. *Symposium on Design, Test, Integration and Packaging of MEMS/MOEMS (DTIP 2005), June 1-3, 2005, Montreux, Switzerland.* TIMA, 2005. pp. 386-390. ISBN:2-84813-0357-1.
10. WANG, F., O. HANSEN. Electrostatic energy harvesting device with out-of-the-plane gap closing scheme. *Sensors and Actuators A: Physical.* 2014, 211, 131–137. ISSN 0924-4247.
11. CROVETTO, A., F. WANG, O. HANSEN. An electret-based energy harvesting device with a wafer-level fabrication process. *Journal of Micromechanics and Microengineering.* 2013, 23(11): 4010. doi: 10.1088/0960-1317/23/11/114010.
12. ZHANG, Y., et.al. Electrostatic energy harvesting device with dual resonant structure for wideband random vibration sources at low frequency. *Review of Scientific Instruments 87*, 125001. 2016. doi: dx.doi.org/10.1063/1.4968811
13. SUZUKI, Y., D. MIKI, M. EDAMOTO, M. HONZUMI. A MEMS electret generator with electrostatic levitation for vibration-driven energy-harvesting applications. *Journal of Micromechanics and Microengineering*. 2010, 20, 104002. https://doi.org/10.1088/0960-1317/20/10/104002.
14. SUHAIMI, K., R. RAMLAN, A. PUTRA. A Combined Softening and Hardening Mechanism for Low Frequency Human Motion Energy Harvesting Application. *Advances in Acoustics and Vibration*. 2014, Article ID 17032, pp. 1-13. doi: http://dx.doi.org/10.1155/2014/217032
15. WARNEKE, B., et al. Smart Dust: Communicating with a Cubic-Millimeter Computer. *Computer*. 2001, vol. 34, No. 1, pp. 44–51. ISSN 0018-9162.
16. YANG, B., C. LEE C. Non-resonant electromagnetic wideband energy harvesting mechanism for low frequency vibrations. *Microsystem Technologies.* 2010, vol. 16, 961–966. doi: 10.1007/s00542-010-1059-z

17. SARDINI, E., M. SERPELLONI. An efficient electromagnetic power harvesting device for low-frequency applications. *Sensors and Actuators A: Physical*. 2011, 172(2), 475-482. ISSN 0924-4247.
18. MAHMOUDI, S., et al. Enhancement of the performance of a hybrid nonlinear vibration energy harvester based on piezoelectric and electromagnetic transductions. *Smart Material Structures.* 2014, vol. 23, 075024. doi: https://doi.org/10.1088/0964-1726/23/7/075024
19. JUILLARD, J., et al. From MEMS to NEMS: Closed-loop actuation of resonant beams beyond the critical Duffing amplitude. *In Proceedings of the 2008 IEEE Sensors, Lecce, Italy, 26–29 October 2008*. pp. 510–513.
20. KACEM, N., S. BAGUET, S. HENTZ, R. DUFOUR. Nonlinear phenomena in nanomechanical resonators: Mechanical behaviors and physical limitations. *Mechanics & Industry* . 2010, 11, 521–529. ISSN 2257-7777.
21. ABED, I., et al. Multi-modal vibration energy harvesting approach based on nonlinear oscillator arrays under magnetic levitation. *Smart Materials and Structures.* 2016, 25, 025018. doi: https://doi.org/10.1088/0964-1726/25/2/025018
22. ZHU, D., et al., Closed Loop Frequency Tuning of a Vibration-Based Micro-Generator. *Proceedings of PowerMEMS 2008+ microEMS2008, November 9–12, 2008, Sendai, Japan*, 2008. pp. 229–232.
23. EL-HAMI, M., et al., Design and Fabrication of a New Vibration-Based Electromechanical Power Generator, *Sensors and Actuators A: Physical.* 2001, 92, 2001, 335–342. ISSN 0924-4247.
24. BEEPY, S. P., et al., A Micro Electromagnetic Generator for Vibration Energy Harvesting. *Journal of Micromechanics and Microengineering.* 2007, 17(7), 1257–1265. doi: https://doi.org/10.1088/0960-1317/17/7/007
25. GLYNNE-JONES, P., et al., An Electromagnetic, Vibration-Powered Generator for Intelligent Sensor Systems. *Sensors and Actuators A: Physical.*2004, 110, 344–349. ISSN 0924-4247.
26. von BÜREN, T., and G. TRÖSTER, Design and Optimisation of a Linear Vibration-Driven Electromagnetic Micro-Power Generator. *Sensors and Actuators A: Physical.* 2007, 135(2), 765–775. ISSN 0924-4247.
27. ROME, Lawrence C., et al., Generating Electricity While Walking with Loads. *Science*, September 2005, 309, pp. 1725–1728. doi: 10.1126/science.1111063
28. GRANSTROM, J., et al., Energy Harvesting from a Backpack Instrumented with Piezoelectric Shoulder Straps. *Smart Materials and Structures*. October 2007, vol. 16(5), pp. 1810–1820. doi: https://doi.org/10.1088/0964-1726/16/5/036
29. Fundamentals of Piezoelectricity. In*: Piezoelectric Transducers for Vibration Control and Damping. Advances in Industrial Control*. Springer, London, 2006, pp 9-35
30. BEEPY S., N. WHITE. Energy harvesting for autonomous systems (Smart materials, structures and systems) Fundamental Understanding of Piezoelectric Strain Sensors. *Journal of Intelligent Material Systems and Structures*. 2000, 11. doi: 10.1106/8BFB-GC8P-XQ47-YCQ0
31. IEEE Standard on Piezoelectricity, 1987, ANSI/IEEE Standard 176.
32. BEEPY, S.P., M. J. TUDOR, N. M. WHITE. Energy harvesting vibration sources for microsystems applications. *Measurement Science and Technology*. 2006, 17(12), pp. 175–195. doi: https://doi.org/10.1088/0957-0233/17/12/R01
33. SIROHI, J., I. CHOPRA. Fundamental Understanding of Piezoelectric Strain Sensors. *Journal of Intelligent Material Systems and Structures*. 2000, 11(4), pp. 246–257. ISSN 1530-8138.

34. SODANO, H. A., G. PARK, D. J. INMAN. Estimation of Electric Charge Output for Piezoelectric Energy Harvesting. *Strain: An International Journal for Experimental Mechanics.* 2004, 40(2), 49–58. ISSN 1475-1305.
35. ERTURK, A.; D. J. INMAN. Electromechanical Modeling of Cantilevered Piezoelectric Energy Harvesters. *In Energy Harvesting Technologies.* Springer: Berlin, Germany, 2009. pp. 41–77.
36. MELLO, L.A.M., C.Y. KIYONO, P. H. NAKASONE, E. C. N. SILVA. Design of quasi-static piezoelectric plate-based transducer by using topology optimization. *Smart Materials and Structures*. 2014, 23(2). DOI: https://doi.org/10.1088/0964-1726/23/2/025035
37. NAKASONE, P.H., N. SILVA. Dynamic design of piezoelectric laminated sensors and actuators using topology optimization. *Journal of Intelligent Material Systems and Structures*. 2010, 21(16), 1627–1652. ISSN 1530-8138.
38. ASHRAF, K., M. H. M. KHIR, J. O. DENNIS, Z. BAHARUDIN. A wideband, frequency up-converting bounded vibration energy harvester for a low-frequency environment. *Journal Smart Material and Structures.* 2013, 22 (2). DOI: https://doi.org/10.1088/0964-1726/22/2/025018
39. LI, W.G., S. HE, S. YU. Improving Power Density of a Cantilever Piezoelectric Power Harvester Through a Curved L-Shaped Proof Mass. *IEEE Transactions on Industrial Electronics*. 2010, 57(3), 868–876. ISSN 0278-0046.
40. EL-HEBEARY, M.M.R., M. H. ARAFA, S. M. MEGAHED. Modeling and experimental verification of multi-modal vibration energy harvesting from plate structures. *Sensors and Actuators A: Physical*. 2013, 193, 35–47. ISSN 0924-4247.
41. BAI, X., Y. WEN, P. LI, J. YANG, X. PENG, X. YUE. Multi-modal vibration energy harvesting utilizing spiral cantilever with magnetic coupling. *Sensors and Actuators A: Physical*. 2014, 209, 78–86. ISSN 0924-4247.
42. ERTURK, A., P. A. TARAZAGA, J. R. FARMER, D. J. INMAN. Effect of Strain Nodes and Electrode Configuration on Piezoelectric Energy Harvesting from Cantilevered Beams. *Journal of Vibration and Acoustics*. 2009, 131(1), 011010-1–011010-11. DOI: doi:10.1115/1.2981094
43. REZAEISARAY, M., M. El GOWINI, D. SAMEOTO, D. RABOUD, W. MOUSSA. Low frequency piezoelectric energy harvesting at multi vibration mode shapes. *Sensors and Actuators A: Physics*. 2015, 228, 104–111. ISSN 0924-4247.
44. BUCCIARELLI L.L. *In Engineering Mechanics for Structures*. Chapter 8 Dover Publications: Mineola, NY, USA, 2009.
45. ERTURK, A., D. J. INMAN. On Mechanical Modeling of Cantilevered Piezoelectric Vibration Energy Harvesters. *Journal of Intelligent Material Systems and Structures*. 2008, 19(11), 1311–1325. ISSN 1530-8138.
46. KANG, Z., L. TONG. Integrated optimization of material layout and control voltage for piezoelectric laminated plates. *Journal of Intelligent Material Systems and Structures*. 2008, 19(8), 889-904. ISSN 1530-8138.
47. CADY, W.G. *Piezoelectricity: An Introduction to the Theory and Applications of Electromechanical Phenomena in Crystals*; McGraw-Hill: New York, NY, USA, 1946.
48. DJUGUMA, R., P. TRIVAILO, K. GRAVES. A study of energy harvesting from piezoelectrics using impact forces. *The European Physical Journal Applied Physics*. 2009, 48(1), ISSN 1286-0042.
49. HAN, J-E., D. KIM, Y. KWANG-SEOK. All-polymer hair structure with embedded three-dimensional piezoresistive force sensors. *Sensors and Actuators A: Physical*. 2012, 188, 89-94. ISSN 0924-4247.

50. ZHU, D., S. BEEBY, J. TUDOR, N. WHITE & N. HARRIS. A novel miniature wind generator for wireless sensing applications. *Proceedings IEEE Sensors 2010, November 1-4, 2010, Waikoloa, Hawaii, USA*. pp. 1415 – 1418. DOI: 10.1109/ICSENS.2010.5690505
51. ROUNDY, S., P. K. WRIGHT and K. S. J. PISTER. Micro-Electrostatic Vibration-to-Electricity Converters. *Proc. American Society of Mechanical Engineers International Mechanical Engineering Congress and Exposition, 2002-34309, New Orleans, LA, November 17–22, 2002*. pp. 487-496.
52. ZHU, D., M. J. TUDOR and S. P. BEEBY. Strategies for Increasing the Operating Frequency Range of Vibration Energy Harvesters: A Review. *IOP Journal of Measurement Science and Technology*. 2010, 21(2). DOI: https://doi.org/10.1088/0957-0233/21/2/022001
53. WU, X., J. LIN, S. KATO, K. ZHANG, T. REN and L. LIU. A frequency adjustable vibration energy harvester. *Proceedings of PowerMEMS 2008+ microEMS2008, November 9–12, 2008, Sendai, Japan*. pp. 245–8.
54. BENDAME, M., E. ABDEL-RAHMAN and M. SOLIMAN. Electromagnetic Impact Vibration Energy Harvesters. *In: Belhaq M. (eds) Structural Nonlinear Dynamics and Diagnosis.* Springer Proceedings in Physics, 2015, 168, pp. 29-58. DOI 10.1007/978-3-319-19851-4_2
55. SCHEIBNER, D., et al., Characterization and Self-Test of Electrostatically Tunable Resonators for Frequency Selective Vibration Measurements, *Sensors and Actuators A: Physical*. 2004, 111(1), 93–99. ISSN 0924-4247. DOI: https://doi.org/10.1016/j.sna.2003.10.010
56. ADAMS, S. G., et al., Capacitance Based Tunable Micromechanical Resonators. *8th International Conference on Solid-State Sensors and Actuators, and Eurosensors IX*. Stockholm, Sweden, 1995. pp. 438–441.
57. CHARNEGIE, D., *Frequency Tuning Concepts for Piezoelectric Cantilever Beams and Plates for Energy Harvesting*. M.Sc. Dissertation, School of Engineering, University of Pittsburgh, 2007.
58. ROUNDY, S., P. K. WRIGHT and J. M. RABAEY. *Energy Scavenging for Wireless Sensor Networks with Special Focus on Vibrations*. Boston, MA: Kluwer Academic Publishers, 2004.
59. BLEVINS, R. D., *Formulas for Natural Frequency and Mode Shape*. Malabar, FL: Krieger Publishing Company, 2001.
60. WU, W.-J., et al., Tunable Resonant Frequency Power Harvesting Devices. *Proceedings of SPIE*, Vol. 6169, 2006, pp. 55–62. DOI: https://doi.org/10.1117/12.658546
61. CHALLA, V. R., et al., A Vibration Energy Harvesting Device with Bidirectional Resonance Frequency Tunability, *Smart Materials and Structures*. 2008, 17(1), 2008, p. 015035. doi.org/10.1088/0964-1726/17/01/015035.
62. ABED, I.; et al. Nonlinear dynamics of magnetically coupled beams for multi-modal vibration energy harvesting. In *Proceedings of the SPIE 9799, Active and Passive Smart Structures and Integrated Systems, Las Vegas, NV, USA, 20 March 2016;* 9799. doi: 10.1117/12.2218410
63. SHARVARI, D, J. ZU, and Y. ZHU. A nonlinear multi-mode wideband piezoelectric vibration-based energy harvester using compliant orthoplanar spring, *Applied Physics Letters*. 2015, 106(16). 163903. doi: 10.1063/1.4919000
64. BAI, X, Y. WEN, P. LI, J. YANG, X. PENG, X. YUE, Multi-modal vibration energy harvesting utilizing spiral cantilever with magnetic coupling, *Sensors and Actuators A: Physical*. 2014, 209. pp.78–86. doi: 10.1016/j.sna.2013.12.022.

65. Dauksevicius, R, D Briand, Andrés Felipe Vasquez Quintero, et al. Multiphysics Finite Element Model of a Frequency-amplifying Piezoelectric Energy Harvester with Impact Coupling for Low-frequency Vibrations. *Journal of Physics Conference Series. Vol. 476*. BRISTOL: IOP PUBLISHING LTD, 2013. Print. doi:10.1088/1742-6596/476/1/012090.
66. ASHRAF, K., M. H. M. KHIR, J.O. DENNIS, Z. A. BAHARUDIN, A wideband, frequency up-converting bounded vibration energy harvester for a low-frequency Environment. *Smart Materials and Structures*. 2013, 22, 049601. doi: 10.1088/0964-1726/22/2/025018
67. TANG, Q. C., Y.L. YANG, X. X. LI, Bi-stable frequency up-conversion piezoelectric energy harvester driven by non-contact magnetic repulsion. *Smart Materials and Structures.* 2011, 20(12). 125011. doi: 10.1088/0964-1726/20/12/125011.
68. NAJAFI, K., H. Kulah, Energy scavenging from low-frequency vibrations by using frequency up-conversion for wireless sensor applications. *IEEE Sens. J*. 2008, 8(3), pp. 261–268. Doi: 10.1109/JSEN.2008.917125.
69. LI, H., F. DAI, S. DU, Broadband energy harvesting by exploiting nonlinear oscillations around the second vibration mode of a rectangular piezoelectric bistable laminate. Smart Materials and Structures. 2015, 24(4). doi: 10.1088/0964-1726/24/4/045024.
70. LI, S., A. CROVETTO, Z. PENG, A. ZHANG, O. HANSEN, M. WANG, X. LI, F. WANG, Bi-resonant structure with piezoelectric PVDF films for energy harvesting from random vibration sources at low frequency. *Sensors and Actuators A: Physical*. 2016, 247, pp. 547–554. doi: 10.1016/j.sna.2016.06.033.
71. LI, S.; Z. PENG, A. ZHANG, F. WANG, Dual resonant structure for energy harvesting from random vibration sources at low frequency. *AIP Advances*. 2016, 6(1). 015019. doi: 10.1063/1.4941353.
72. PARK J., *Analytic Methods for Design Practice*, Springer Science & Business Media. 2007. Technology & Engineering
73. K. S. Pister., *Mathematical modeling for structural analysis and design*, Elsevier, 1972, 18(3), pp. 353-375. doi.org/10.1016/0266-8920(88)90025-2
74. FUJIWARA H, T. ABE, K. TANAKA, *Residual Stresses III: Science and technology two volume set*, CRC Press, 1992.
75. ERHART, J., P. PŮLPÁN, M. PUSTKA, *Piezoelectric ceramic resonators*, Springer, 2016.
76. SHERRIT S, H.D. WIEDERICK, B.K. MUKHERJEE, and M. SAYER, An Accurate Equivalent Circuit for the Unloaded Piezoelectric Vibrator in the Thickness Mode, *Journal of Physics D*: *Applied Physics*, 1999, 30(16), pp. 2354-2363. Doi: 10.1088/0022-3727/30/16/014.
77. SEDRA A.S. and K.C. SMITH, *Microelectronic Circuits*, 5th edition, Oxford University Press, 2003.
78. ANSI/IEEE Std 176-1987, IEEE Standard on Piezoelectricity, 1987.
79. GUAN M. and W.H. Liao, Studies on the Circuit Models of Piezoelectric Ceramics, In *International Conference on Information Acquisition, 21-25 June 2004*. pp. 26-31, doi**:** 10.1109/ICIA.2004.1373314.
80. KIM. J., B. L. GRISSO, J. K. KIM, D. S. HA, and D. J. INMAN. Electrical Modeling of Piezoelectric Ceramics for Analysis and Evaluation of Sensory Systems, In *SAS 2008 – IEEE sensors applications symposium*, GA, February 12-14, pp. 122-127.
81. ERTURK A. and D. J. INMAN, Mechanical Modeling of Cantilevered Piezoelectric Vibration Energy Harvesters, *Journal of Intelligent Material Systems and Structures*. 2008, 19(11). 1311. doi: 10.1177/1045389X07085639.

82. ERTURK A., J. RENNO, A. INMAN, Modeling of Piezoelectric Energy Harvesting from an L-shaped Beam-mass Structure with an Application to UAVs. *Journal of Intelligent Material Systems and Structures. 2009,* 20(5), pp. 633-642. doi: 10.1177/1045389X08098096.
83. ERTURK, A., S.R. ANTON, INMAN, D.J. *Piezoelectric energy harvesting from multifunctional wing spars for UAVs: Part 1. Coupled modeling and preliminary analysis*. In *Proceedings of SPIE, the International Society for Optical Engineering*. *Mar 12 2009. San Diego, CA, United States*. 7288. Doi: 10.1117/12.815799.
84. ERTURK, A., P. A. TARAZAGA, J. R. FARMER, and D. J. INMAN. *Effect of Strain Nodes and Electrode Configuration on Piezoelectric Energy Harvesting from Cantilevered Beams*, *Journal of Vibration and Acoustics*. 2009, 131(1). pp. 011010-11. doi: 10.1115/1.2981094.
85. ERTURK A, U. ARIDOGAN, I. BASDOGAN. Analytical modeling and experimental validation of a structurally integrated piezoelectric energy harvester on a thin plate, Smart Materials and Structures. 2014. 23(4). 045039. doi: 10.1088/0964-1726/23/4/045039.
86. ERTURK, A. and D. J. INMAN. An experimentally validated bimorph cantilever model for piezoelectric energy harvesting from base excitations, *Smart Materials and Structures*. 2009, 18(2). pp. 25009-18. Doi: 10.1088/0964-1726/18/2/025009.
87. KAGAWA et al. *Ansys. Multyphysics manual; Abaqus manual*, USA. Hibbitt, Karlsson & Sorensen, Inc. 2000.
88. ERTURK A., D. J. INMAN, C. D. MARQUI JR., An electromechanical finite element model for piezoelectric energy harvester plates. *Journal of Sound and Vibration*. 2009, 327(1-2). pp. 9–25. doi: 10.1016/j.jsv.2009.05.015.
89. SHENG W., H. HONG, H. SIYUAN. Modeling and experimental investigation of an impact-driven piezoelectric energy harvester from human motion. *Smart Materials and Structures*. 2013, 22(10). 105020. Doi: 10.1088/0964-1726/22/10/105020.
90. PARK, J., S. LEE. and B. M. KWAK. Design optimization of piezoelectric energy harvester subject to tip excitation. *Journal of Mechanical Science and Technology*. 2012. 26(1), pp. 137–143. Doi: 10.1007/s12206-011-0910-1.
91. SUNITHAMANI, S., P. LAKSHMI, F. E. EBA., PZT length optimization of MEMS piezoelectric energy harvester with a non-traditional cross section: simulation study. *Microsystem Technologies*. 2013, 20(12). pp. 2165-2171. doi:10.1007/s00542-013-1920-y.
92. KUMAR, A., A. SHARMA. R, KUMAR. R, VAISH. V, S, CHAUHAN. Finite element analysis of vibration energy harvesting using lead-free piezoelectric materials: A comparative study. *Journal of Asian Ceramic Societies*, 2014, 2(2), pp. 138-143. Doi: 10.1016/j.jascer.2014.02.001.
93. REZAEEALAM, B., T. UENO, and S. YAMADA; Finite Element Analysis of Galfenol Unimorph Vibration Energy Harvester, *IEEE Transaction on Magnetics*, 2011, 48(11). pp. 3977-3980. Doi: 10.1109/TMAG.2012.2202273.
94. MIGLINIENE, I., V. OSTASEVICIUS, R. GAIDYS, R. DAUKSEVICIUS, G. JANUSAS, V. JURENAS and P. KRASAUSKAS; Rational Design Approach for Enhancing Higher-Mode Response of a Microcantilever in Vibro-Impacting Mode, 2017, *Sensors.* 17(12):2884. doi: 10.3390/s17122884.
95. OSTASEVICIUS, V. G. JANUSAS, I. MILASAUSKAITE, M. ZILYS and L. KIZAUSKIENE, Peculiarities of the Third Natural Frequency Vibrations of a

Cantilever for the Improvement of Energy Harvesting, *Sensors*. 2015, 15, 12594-12612; doi:10.3390/s150612594.
96. SUNITHAMANI, P. LAKSHMI, Simulation study on performance of MEMS piezoelectric energy harvester with optimized substrate to piezoelectric thickness ratio, *Microsystem Technologies*. 2014, 21(4), pp. 733–738. doi: 10.1007/s00542-014-2226-4.
97. NAGURKA, M.; HUANG, S. A mass-spring-damper model of a bouncing ball. *International Journal of Engineering Education*. 2006, 22(2), pp. 393–401. doi: 0949-149X/91
98. HEHN, T., YIANNOS MANOLI, Interface Modeling and Loss Analysis, In *CMOS Circuits for Piezoelectric Energy Harvesters: Efficient Power Extraction*, Springer, 2014 - Technology & Engineering. pp. 42-43.
99. WILLIAMS, C.B., R.B. YATES, Analysis of a micro-electric generator for microsystems. *Sensors and Actuators A: Physical*. 1996, 52(1–3), 8–11. Doi: 10.1016/0924-4247(96)80118-X.
100. MACHADO, M.; MOREIRA, P.; FLORES, P.; LANKARANI, H.M. Compliant contact force models in multibody dynamics: Evolution of the Hertz contact theory. *Mechanism and Machine Theory*. 2012, 53, 99–121. doi: 10.1016/j.mechmachtheory.2012.02.010.
101. SMITH, J. *Mathematics of the Discrete Fourier Transform (DFT): With Audio Applications*, W3K Publishing, 2007. pp. 133-135.
102. LEADENHAM, S. and ERTURK A. Unified nonlinear electroelastic dynamics of a bimorph piezoelectric cantilever for energy harvesting, sensing, and actuation. *Nonlinear Dynamics*. 2015, 79(3), 1727-1743. doi: 10.1007/s11071-014-1770-x.
103. ERTURK, A.; INMANN, D.J. Electromechanical Modeling of Cantilevered Piezoelectric Energy Harvesters. In *Energy Harvesting Technologies*; Springer: Berlin, Germany, 2009. pp. 41–77.
104. ZHANG, X. and Z. KANG. Dynamic topology optimization of piezoelectric structures with active control for reducing transient response. *Computer Methods in Applied Mechanics and Engineering*. 2014, 281, 200–219. doi: org/10.1016/j.cma.2014.08.011.

SL344. 2018-04-06, 14,5 leidyb. apsk. l. Tiražas 12 egz. Užsakymas 133.
Išleido Kauno technologijos universitetas, K. Donelaičio g. 73, 44249 Kaunas
Spausdino leidyklos „Technologija“ spaustuvė, Studentų g. 54, 51424 Kaunas